Quantification of Flare Combustion Efficiency through Mid-Wavelength Infrared Spectroscopy

by

Rodrigo Brenner Miguel

A thesis

presented to the University of Waterloo

in fulfillment of the

thesis requirement for the degree of

Doctor of Philosophy

in

Mechanical and Mechatronics Engineering

Waterloo, Ontario, Canada, 2022

Examining Committee Membership

The following served on the Examining Committee for this thesis. The decision of the Examining Committee is by majority vote.

External Examiner	Philip J. Smith Professor Emeritus
Supervisor(s)	Kyle J. Daun Professor
Internal Member	Elizabeth J. Weckman Professor
Internal Member	Sean D. Peterson Professor
Internal-external Member	K. Andrea Scott Associate Professor

Author's Declaration

I hereby declare that I am the sole author of this thesis. This is a true copy of the thesis, including any required final revisions, as accepted by my examiners.

I understand that my thesis may be made electronically available to the public.

Abstract

Flares convert unwanted hydrocarbon emissions into carbon dioxide to be disposed into the atmosphere. Although this conversion reduces the oil and gas industry's greenhouse gas inventory, it is still responsible for significant anthropogenic CO_2 emissions. In the case of incomplete combustion, the flare emits unburned fuel, increasing the greenhouse footprint, environmental damage, and possibly presenting a local hazard. The efficiency with which the hydrocarbons are transformed into CO_2, called the combustion efficiency, is assumed to be higher than 98%. However, in some circumstances, combustion efficiency may be reduced significantly.

Mid-wavelength infrared spectroscopy is well suited for fenceline measurements of flare combustion efficiency. As the emission from flares may not be well mixed due to the mechanisms that create the inefficiencies, mid-wavelength infrared cameras make it possible to observe the two-dimensional effects of the three-dimensional concentration field of the species. This study investigates the use of multispectral and hyperspectral mid-wavelength infrared cameras to quantify flare combustion efficiency.

This dissertation begins with a review of the flaring process. Most flaring occurs in the production phase and is used to burn unwanted associated gas from oil extraction. Production flares are susceptible to ambient conditions, and wind can decrease flare efficiency. The dissertation continues with a derivation of the measurement model that relates the measured spectral camera irradiance to the flare plume, and how the model is inverted to infer the column density of gas corresponding to each camera pixel. These column densities are combined with a velocity field obtained from an optical flow algorithm to calculate the species mass flow, and, thereafter, the flare combustion efficiency.

At least one independent signal is necessary to infer each parameter needed to compute flare combustion efficiency. In the case of multispectral cameras, the number of signals is limited, and the spectral bands need to be carefully selected to generate independent signals. A technique for selecting optimal filters for a multispectral camera to measure flare combustion efficiency is presented. Filter sets are ranked in terms of the change in the combustion efficiency to the change in measurement noise. Synthetic data are generated using the resulting species concentration and temperature from a simulated flare-in-crosswind. The CH_4 and CO_2 concentrations, as well as temperatures, are estimated using commercially-available filter sets. The estimated parameters are transformed to combustion efficiency and compared using error propagation. The optimal filters are aligned with the CH_4 and CO_2 absorption bands, emphasizing the CH_4 lines.

The potential of using imaging Fourier transform spectrometers (IFTS) is next assessed to measure the combustion efficiency. The species mass flows are estimated by combining species column densities estimated from a spectroscopic model with intensity-weighted velocities found using optical flow. Simulated measurements using a computational fluid dynamics (CFD) large eddy simulation of a flare in a crosswind are used to establish the technique's viability, followed by experimental measurements on a heated gas vent. Finally, preliminary measurements are carried out on laboratory-scale steam- and air-assisted flares. While the simulated measurements and heated vent experiments support the feasibility of this approach, experimental spectra from the lab-scale flare were contaminated with anomalies, which complicates the quantitative interpretation of the measurement data.

Obtaining the concentration distribution of combustion products from spectroscopic data is challenging due to the many variables involved and the indirect relationship between the measured spectra and the unknown quantities. These effects often make the inference problem mathematically ill-posed and computationally demanding to solve. The dissertation examines how incorporating a

thermochemical manifold reduction (TCMR) mechanism into the inference procedure reduces the number of unknown parameters, decreasing the ill-posedness of the problem and the computational cost of solving it. The approach is demonstrated on synthetic images from the CFD data. The information introduced by the TCMR improved the CO_2 column density accuracy and precision for all tested wavenumber resolutions in relation to a full regression, with a more pronounced improvement for pixels having a larger column density. On the other hand, there is no significant change in estimating the concentrations of unburned fuel.

Optical gas imaging has the potential to estimate flare combustion efficiency. The IFTS demonstrated good accuracy in the numerical and part of experimental tests. Additionally, in the tests on the lab-scale flares, the IFTS-inferred combustion efficiency agreed with the expected trends, excluding plumes rich in soot. Although numerical experiments showed that the multispectral camera was inferior to the IFTS, it is significantly less expensive and insensitive to turbulence effects that complicate interpretation of the IFTS spectra.

Acknowledgements

Without the support of many individuals, this thesis would not be possible. First, I would like to thank my supervisor and mentor, Prof. Kyle Daun. I would like to use the phrase he always uses to describe someone to describe him, "he's a really nice person." I learned from him much more than inverse analysis and radiation; he taught me through example lessons about kindness, leadership, and friendship that I will take with me for the rest of my life. Kyle, it was an honour and a pleasure to study under your guidance, and I really cannot thank you enough. I would also like to thank him for the opportunity to work with an incredible and hard-working team at WatLIT.

I would like to thank my fellow researchers for their thoughtful insights during the weekly seminar and friendship. To name just a few: Roger Tsang, Mohit Verma, Dr. Samuel Grauer, Natalie Field, Dr. Sina Talebi-Moghaddam, Dr. Timothy Sipkens, Timothy Thompson, Matthew Yao, Nigel Singh, Dr. Paul Hadwin, Dr. Kaihsiang Lin, Fatima Suleiman, Stephen Robinson-Enebeli, Stanislav Musikhin, Cameron Klassen, Cory Yan, Ned Zhou, Tom Zhao, Michael Nagorski, Dr. Paule Lapeyre[1], Daniel Blackmore[1], Nishant Narayanan[1], and Arpan Singh[1]. I am lucky to participate in this wonderful group of people, which made this stage of my life more enjoyable. I would like to extend these acknowledgments to Dr. Brad Conrad from Carleton University and Dr. Johannes Emmert from Technische Universität Darmstadt; although they are not officially part of WatLIT, they participated in this journey.

Of particular note, I would like to thank Samuel Grauer for helping me early in the research to understand and establish the spectroscopy model. Thanks for his insights, patience, and pessimism in

[1] Sadly, I did not have the pleasure to meet in person yet.

new suggested approaches (rightly every time, if I had listened, it would have saved me time). I want to thank Johannes Emmert for his help in the research, with his great ideas and insights. It would not have been possible to complete this work without your collaboration.

I wish to extend my special thanks to Jeremy Thornock for providing the CFD data. Thanks to Milad Zamani for his help collecting valuable experimental data and Prof. Jason Olfert for sharing his wonderful laboratory. Thanks to Prof. Elizabeth Weckman for sharing her wonderful laboratory. My acknowledgments to Dr. Caroline Turcotte and Defence Research and Development Canada for sharing the MWIR IFTS (Hyper-Cam) used to collect data in the study. Finally, thanks to Telops staff, Martin Chamberland, Jean-Philippe Gagnon, Vincent Farley, and Sylvain Gatti for the training and help using the Hyper-Cam.

I wish to show my appreciation to the examination committee members, including Prof. Kyle Daun, Prof. Andrea Scott, Prof. Sean Peterson, Prof. Elizabeth Weckman, and Prof. Philip Smith. Your willingness to review this thesis is greatly appreciated.

Moreover, I want to thank my family, my mother Alaidete, my father Homero, and my sister Paula. They supported me and brought me here. Finally, I thank my daughter Isabela and especially my wife, Heloísa. They often had to accept my absence during this journey and helped me all along. Without you, I would not have made it here.

I would like to thank CAPES. This study was financed in part by the Coordenação de Aperfeiçoamento de Pessoal de Nível Superior - Brasil (CAPES) - Finance Code 001.

Dedication

To my daughter,

Isabela Schroeder Miguel.

Table of Contents

List of Figures

List of Tables

List of Abbreviations

ART	Algebraic Reconstruction Technic
BTEX	Benzene, Toluene, Ethylbenzene and Xylene
CE	Combustion Efficiency
CFD	Computational Fluid Dynamics
CH_4	Methane
CO_2	Carbon Dioxide
CORINAIR	CORe INventory AIR emissions
E&P Forum	Oil/Gas Exploration & Production, Actual Association of Oil & Gas Producers
EEMS	Environmental Emissions Monitoring System
EF	Emission Factor
ESF	Emission Scaling Factor
GHG	Greenhouse Gas
GWP	Global Warming Potential
HITRAN	High-Resolution Transmission Molecular Absorption
HWHM	Half-Width at Half Maximum
ICV	Image Correlation Velocimetry
IFK	Integral Equation of the First Kind
IFT	Inverse Fourier Transform
IFTS	Imaging Fourier Transform Spectrometer
IID	Independent and Identically Distributed
ILS	Instrument Line Shape
InSb	Indium Antimonide
IR	Infrared
LBL	Line-by-Line
LES	Large Eddy Simulation
LHV	Lower Heating Value
LOS	Line-of-Sight
MLE	Maximum Likelihood Estimation
MOPD	Maximum Optical Path Difference
MS	Multispectral (Infrared Camera)
MWIR	Mid-wavelength Infrared

N_2O	Nitrous Oxide
NETD	Noise Equivalent Temperature Difference
NG	Natural Gas
OGI	Optical Gas Imaging
OPD	Optical Path Difference
QOGI	Quantitative Optical Gas Imaging
RTE	Radiative Transfer Equation
SCA	Scene Change Artifacts
SLPM	Standard Litres per Minute
SNR	Signal to Noise Ratio
SO_2	Sulphur Dioxide
TCMR	Thermochemical Manifold Reduction
US EPA	United States Environmental Protection Agency
VIIRS	Visible Infrared Imaging Radiometer Suite

List of Symbols

	Combustion
a-h	Chemical reaction balancing coefficients
M	Molar mass
$\dot{m}$	Mass flow
$\dot{n}$	Mole flow rate
p	Pressure
T	Temperature
U_∞	Crosswind velocity
V_j	Fuel jet velocity
w	Mass fraction
x	Fuel molecule's number of carbon atoms
X	Mole fraction
y	Fuel molecule's number of hydrogen atoms
η_{comb}	Combustion efficiency
ρ	Density
χ	Volume fraction
	Subscripts
∞	Ambient conditions
C	Carbon
fuel	Referent to the fuel state
m	Intermediate hydrocarbon number of carbon atoms
n	Intermediate hydrocarbon number of hydrogen atoms
plume	Referent to the combustion products plume
soot	Soot
i	i^{th} species

	Radiative Transfer
e	Level of energy
f	Lineshape
$I_{0\eta}$	Background radiation spectral intensity
$I_{b\eta}$	Blackbody spectral intensity
$I_{L\eta}$	Spectral intensity at distance L
I_{η}	Spectral intensity in the wavenumber η
L	Optical total length
s	Distance parameter at the LOS
S_{ij}	Spectral line intensity of the ij*th* molecule transition
x_V	Ratio between Lorentz and Voigt lineshape HWHM
β	Extinction coefficient
γ	Line half-width at half-maximum
η	Wavenumber
η_{ij}	ijth molecule transition's line central wavenumber
κ_{η}	Absorption coefficient
λ	Wavelength
σ_0	Normalized center line strength
$\sigma_{s\eta}$	Scattering coefficient
Φ	Scattering phase function
Ω	Solid angle
	Subscripts
p	Photon
ij	Energy states
L	Lorentzian profile
D	Doppler profile
V	Voigt profile
m	m^{th} species
mix	Gas mixture

	Camera Model
a	Asymmetric instrument line shape coefficient
F	Instrument line shape
f_η	Normalized sensor spectral response
G	Warm filter radiative emission
H_x	Interferogram signal
N	Column number density
$\mathbf{S}$	Model spectrally-resolved vector data
$\mathbf{S}^{meas}$	Measured spectrally-resolved vector data
$\bar{u}$	Intensity weighted normal velocity
$\mathbf{x}$	Gas state vector
x_k	Optical path difference
x_m	Maximum optical path difference
$\mathbf{\Gamma}_S$	Signal's covariance matrix
$\mathbf{\delta S}$	Model errors
η_1	Camera's lower wavenumber limit
η_2	Camera's higher wavenumber limit
η_{res}	Spectral resolution
θ	Control surface parametric distance
σ	Characteristic plume width
σ_{SB}	Signal noise standard deviation
τ_η	Optical filter transmissivity

	Velocimetry
$\mathbf{L}$	2nd order Tikhonov smoothness matrix
N_v	Number of vertices in the image
$\boldsymbol{s}$	Intensity derivatives vector
S_t	Intensity changes in time
S_x	Intensity gradient in x direction
S_y	Intensity gradient in y direction
t	Time

u	Velocity component at x direction
v	Velocity component at y direction
$\mathbf{V}$	Velocity vector

Measurement Error Propagation

$\mathbf{F}_{\text{filter}}$	Filter transmissivity matrix
$\mathbf{f}_i$	Filter transmissivity vector
$f_{\eta j,i}$	Filter transmissivity at the j^{th} wavenumber
G	Gaussian LOS profile
$\mathbf{I}$	Identity matrix
$\mathcal{J}_L$	Spectral intensity matrix
$\hat{\mathcal{J}}_{\text{L}}$	Modelled radiative intensity
$\mathbf{J}$	Sensitivity matrix (Jacobian matrix)
$\hat{\mathbf{x}}$	Optimal result
α	Uncertainty translation factor from spectral intensity noise to CE uncertainty
$\mathbf{\Gamma}$	Covariance matrix
η_{pixel}	Pixel combustion efficiency
$\sigma_{\mathcal{J}}$	Spectral intensity's noise standard deviation
	Subscripts
*	Optimal configuration
CE	Combustion efficiency
$\mathcal{J}$	Spectral intensity
MC	Monte Carlo
N	Column number
S	Camera signal

Thermochemical Manifold Reduction (TCMR)

h	Enthalpy
x	TCMR states fractions
X_{R}	Radiant fraction
β	TCMR pure states vector

	Physical Constants
A	Avogadro's number
c	Speed of light
h	Planck's constant
k_B	Boltzmann constant
R_u	Universal gas constant

Chapter 1

Introduction to Flare Combustion Efficiency Measurements

Fossil fuels – coal, crude oil, and natural gas (NG) – have tremendous economic and political importance. Crude oil is mainly used to produce energy. It is also transformed into gasoline, diesel oil, lubricating oils, kerosene, plastics, and asphalt, among other products. Additionally, crude oil and NG are very cost-effective in generating energy; despite being a finite resource, they can be easily found and transported.

Nevertheless, fossil fuels are highly polluting and are responsible for severe environmental problems. During combustion, many pollutants are released into the atmosphere, contributing to climate change. As a result, the global energy matrix is slowly changing from the most pollutant coal to the less pollutant crude oil, and later to NG to reduce emissions and facilitate pipeline transport. However, the pollution from fossil fuels is not solely limited to their use but also to their extraction.

Once petroleum is extracted from the reservoir, the pressure drop causes the NG dissolved into the crude oil to come out of solution as a free gas. The NG usually cannot be stored or utilized locally because of an intermittent gas flow, the low heating value of the gas, the presence of contaminants in the gas, or the lack of sufficient infrastructure [1,2]. In these cases, the unwanted gas must either be flared or directly vented into the atmosphere. Venting presents a serious threat to climate change since methane (CH_4), the main component of NG, has a global warming potential (GWP) 36 times greater than carbon dioxide (CO_2) over 100 years for the same mass [3]. The main objective of flaring is to convert hydrocarbons into CO_2, thereby significantly decreasing the greenhouse footprint of these gaseous by-products. Additionally, oil and gas industry effluents can contain sulphur and mercury

components, solid matter, and aromatic hydrocarbons, including benzene, toluene, ethylbenzene, and xylene (BTEX). These contaminants pose health and environmental risks, which, in some cases, may be reduced by flaring, provided that the combustion process transforms these components into safer species.

Although flaring has a lower environmental impact than venting, it remains a significant contributor to climate change [4]. Satellite measurements (Visible Infrared Imaging Radiometer Suite, VIIRS) suggest that 150 Gm^3 of NG was flared in 2019 [2,5,6]. This flared NG generates 300 Gm^3 of CO_2 annually, equivalent to 0.9% of the global anthropogenic CO_2 emissions [7]. Figure 1 shows the annual volume of flared NG and oil production over the same period. These estimates assume that almost all of the CH_4 is converted into CO_2 (e.g., combustion efficiency of 98% under ideal conditions [8]), but inefficiencies in the combustion process can drastically increase the emissions of anthropogenic greenhouse gases (GHGs). A study in Texas [9] found that combustion efficiencies (CE) of different flares follow a log-normal distribution, so the emission of methane from flares may be more than twice what one would expect by assuming that each flare operates at the mean CE value of 98%. This result shows that few flares are responsible for most of the methane emissions from flaring, and identifying the flares in the tail of the distribution is crucial in order to reduce the impact of flaring on climate change.

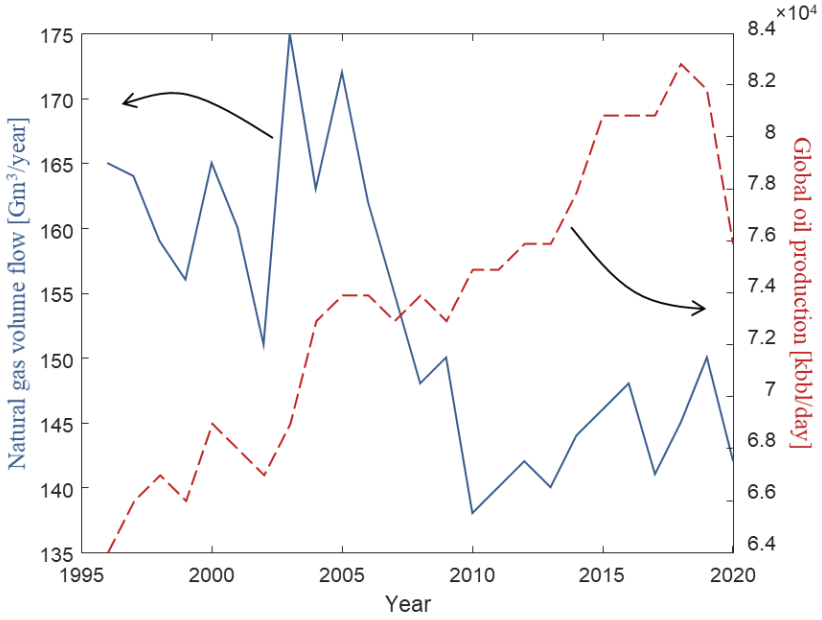

Figure 1 Global natural gas volume flared annually since 1996 in Gm^3 per year compared to global oil production in kilo barrels per day (1-kilo barrel≈0.159m^3), data from [6].

1.1 Motivation

Quantification is a vital step toward reducing anthropogenic GHG emissions. In the case of flaring, the combustion products in the plume need to be measured in order to estimate the real impact of flares. Flare volume is typically self-reported by the operator, and emissions are calculated using emission factors (EFs) based on the fuel flow rate [2]. However, this process is fraught with uncertainty, as exemplified by the wide range of EFs shown in Table 1. The EF depends on the quantity, quality, and composition of the fuel burned, the combustion devices, and operating conditions [10]. According to MacKay, all studies that measured site-level emissions from Canadian oil and gas production found

higher CH_4 emissions than the self-reported data by a factor of 1.5 to 3 times [11]. Furthermore, accidental emissions or discharges are rarely reported by operators [12].

Table 1 Flare methane emission factor from different sources [11].

Year	Agency	Methane EF [g/kg_{Fuel}]
1991	US EPA[2]	20
1994	E&P FORUM[3]	35
1996	US EPA	20
2002	CORINAIR[4]	2.5
2008	EEMS[5]	10-45
2015	US EPA	3

Accurate quantification of flare emissions is necessary in order to assess compliance with environmental policy and regulations within Canada and around the world. The most important is the Paris Agreement, which aims to limit the global average temperature increase to no more than 2ºC, preferably less than 1.5ºC, having the preindustrial temperature as a reference. Following the Paris agreement, Canada committed to reducing GHG emissions by 30% below 2005 levels by 2030 [13]. Reduction targets of CH_4 are based on component-level emissions inventory reported annually, based in part on industry estimation and self-reporting using components EF [11].

1.2 Global Flared Emission Estimates

Satellite data is one means to obtain a coarse "top-down" estimate of global and local flared volumes. The technique is based on estimating two parameters: temperature and the emission scaling factor (ESF), a combination of the flare projected area and emissivity. In the method, two Planck curves

[2] US EPA: United States Environmental Protection Agency
[3] E&P Forum: oil/gas Exploration & Production, actual Association of Oil & Gas producers (OGP)
[4] CORINAIR: CORe INventory AIR emissions
[5] EEMS: Environmental Emissions Monitoring System

weighted by the ESF, which represent the ratio of the flare and background contributions, are fitted to the observed spectra. Additional calculations are then done to estimate source size (m^2), radiant heat intensity (W/m^2), and radiant heat (MW). The amount of NG flared is inferred from the radiant heat, using a calibration coefficient to address the unknown combustion efficiency and radiant fraction [2].

The uncertainty in flaring emission inventories can lead to significant disparities between satellite observations and models. The uncertainties arise from limited access to flaring volume records and lack of field measurements; direct measurements are hard to obtain if they exist at all [14]. Improper instrument calibration, data flaws, or calculation method errors can lead to underestimating or overestimating satellite-derived emissions [15]. The lack of publicly-available field measurements makes the validation of species rates produced on flaring derived from satellite data challenging. The parameters from the satellite model estimates are generally evaluated using data from the laboratory or self-reported data from the oil and gas facilities [14].

A recent study used VIIRS information (temperature and flare area) to estimate the amount of gas flared in southern Texas [16]. They used the reported vented and flared gas estimates from the Railroad Commission of Texas to calibrate a polynomial function. However, the results likely underestimate the true gas emission rate as the data used are self-reported. Independent local measurements of flare emissions are needed to get more accurate satellite flared volume estimates. Furthermore, satellite methods look for brighter flares to discard biomass sources; this procedure can bias the results as it is expected that more efficient combustion will produce a “hotter” flame. Black carbon flare emission studies [17–19] also show uncertainties in the reported EFs. The cited studies show that local and independent data is needed to access actual flares emissions.

1.3 Research Objectives and Overview

This thesis aims to provide an independent, science-based flare emissions measurement method using quantitative optical gas imaging (QOGI). Optical gas imaging (OGI) allows the visualization of a two-dimensional gas distribution. In principle, the image's pixel intensity can be used to estimate the amount of gas between the background and the camera. The gas absorbs or emits radiation affecting the pixel intensity. For a known temperature, the pixel intensity is proportional to the number of gas molecules along the optical path between the background and the camera. The optical path between the background and the camera for each pixel is also called the pixel's line-of-sight (LOS). Although QOGI is used to estimate the number of gas molecules of one species at a known temperature, it is possible to simultaneously estimate the number of molecules and temperature of multiple species using multiple independent signals.

Multispectral (MS) infrared (IR) camera can generate intensities for different IR spectral bands, usually using a set of bandpass filters mounted on a rotating filter wheel in front of the camera. Imaging Fourier transform spectrometers (IFTSs) use the principle of interferometry to realize a much higher spectral resolution, albeit with a lower temporal resolution. With the spectral resolution obtained from MS or IFTS cameras, the number of molecules of multiple species at unknown temperatures can be estimated, assuming that the intensity sensitivity to a change in each species' number of molecules and temperature is unique. Finally, it is possible to estimate the species flow rates and the flare CE by combining the species number of molecules with the apparent gas velocity.

The proposed method aims to estimate flare CE without prior knowledge of flare parameters such as fuel flow, assistance flow, plume temperature, and wind speed. The data generated using the method should help improve top-down measurements using satellite data. Furthermore, this method

should help identify flares responsible for emitting most of the GHGs and, therefore, the best locale to place the infrastructure to capture natural gas or identify flare stacks improvement potential.

In order to advance in an independent method to measure the flare CE, the study can be divided into two main objectives:

1. Assess the potential of QOGI to measure flare CE and compare the MS and IFTS to measure the flare CE without prior knowledge of the flare parameters.

2. Develop procedures to improve the flare CE estimation by reducing the ill-posedness of the problem, either by enhancing the signal independence or adding physically based prior information to the model.

A wide range of process strategies and flare designs have been developed, which may differ based on the origins, composition, and stage in gas production. Chapter 2 defines a flare design and fuel composition typical of Canada's upstream oil and gas operations, which is used throughout the study. Then the NG combustion process is discussed, leading to a definition of flare CE. Although it is assumed that combustion efficiency is above 98%, particular ambient conditions or flow characteristics can lead to inefficiencies in the combustion process, decreasing the flare CE. Some of these effects are discussed in Chapter 2.

The use of an IR camera to measure gas flow is discussed in Chapter 3. It first introduces the principles of IR spectroscopy, absorption coefficient, and radiative transfer model needed to predict the IR radiation that reaches the camera. Next, the MS and IFTS camera models are discussed. These models simulate the camera measurement data knowing the gas state between the background and the camera. However, the parameter of interest is the number of gas molecules represented in each pixel, the species of interest's column density. Then the inverse procedure to obtain the column density from

the camera data is discussed, as is the procedure to obtain the apparent gas velocity from a sequence of images. This chapter then discusses how QOGI is used to obtain the species of interest mass flows and consequently the flare CE, with a review of the QOGI literature.

Chapter 4 presents a general technique to select optimal filters for an MS mid-wavelength IR (MWIR) camera to quantify multiple components of a gas mixture. Filter sets are ranked in terms of the ratio of quantity-of-interest variance to noise variance, which is minimized by the optimal filter set. The suitability of this criterion is demonstrated using a numerical experiment in which the CE of a gas flare is estimated from MWIR images.

Chapter 5 assesses the potential of using IFTSs to measure CE. Simulated measurements using a computational fluid dynamics (CFD) large eddy simulation of a flare in a crosswind are used to establish the technique's viability, followed by experimental measurements on a heated gas vent to validate the model. Then preliminary measurements are carried out on laboratory-scale steam- and air-assisted flares.

Chapter 6 shows how incorporating a thermochemical manifold reduction (TCMR) mechanism into the CE inference procedure reduces the number of unknown parameters, thereby decreasing the ill-posedness of the problem and the computational cost of solving it. The approach is demonstrated on synthetic images of a flare plume representative of those produced with a multispectral camera or an IFTS. The images are generated from CFD data and then used to recover CO_2 and CH_4 column densities.

Finally, Chapter 7 summarizes the conclusions of the thesis, along with suggestions for future work.

Chapter 2

Natural Gas Flares

Natural gas is a by-product of oil extraction, and for various reasons, the utilization of NG can be technically infeasible or economically prohibitive. In this scenario, the NG is flared or vented into the atmosphere, the former being safer and with lower environmental impact. This chapter discusses the origin and composition of flare fuel and stack design. The NG combustion process and CE, likewise the sources of inefficiencies in the combustion process, are also presented. Finally, the methods commonly used to measure flare CE are discussed with a brief literature review of flare CE studies.

2.1 Natural Gas Origin and Composition

Natural gas is typically classified as *conventional* or *unconventional*, depending on its origin [20]. Gas of conventional origin rises from deep reservoirs and is related to oil formation. Gas of unconventional origin is not related to oil formation and is found in shale formations, deep aquifers, coal-bed, and in the form of gas hydrates below the seafloor and Arctic permafrost.

Conventional origin gas can be further classified as *associated* or *non-associated* gas. Associated gas, also called solution gas, is the source for most flaring activity [21]. It emerges when crude oil is brought to the surface; it is often leaner in CH_4 content and richer in heavier hydrocarbons compared to non-associated gas, which is extracted without oil from a reservoir that either does not contain oil or contains only a small quantity of oil.

In terms of composition, NG is categorized according to the quantity of liquid, i.e., *wet* or *dry* gas. Wet gas contains at least 10% of hydrocarbon species having two or more carbon atoms per molecule. Changes in temperature or pressure can condense these species as droplets due to the comparatively higher boiling point of heavier hydrocarbons compared to methane. Wet gas is commonly related to associated gas, as it comes directly from crude oil. In contrast, dry gas is more typical of non-associated gas. Typical compositions of wet and dry gas are shown in Table 2.

Table 2 Natural gas typical composition, adapted from [20], and Alberta NG mean composition from [21].

Species	Wet NG [%]	Dry NG [%]	Alberta NG [%]
Methane	84.6	96	85.8
Ethane	6.4	2	4.8
Propane	5.3	0.6	2.4
Isobutene	1.2	0.18	0.4
n-Butane	1.4	0.12	0.7
Isopentane	0.4	0.14	0.5
n-Pentane	0.2	0.06	
Hexane	0.4	0.1	0.2
Heptane	0.1	0.8	0.2
Carbon dioxide	<=5		1.4
Helium	<=0.5		0.1
Hydrogen sulphide	<=5		0.3
Nitrogen	<=10		3.4
Argon	<=0.05		

Finally, NG can be categorized as *sweet* or *sour* based on its acidic gases, mainly in the form of hydrogen sulphide (H_2S) and, less often, CO_2. Several standard threshold sulphur contents for sweet versus sour gas have been proposed in the literature. NG with amounts higher than 5% of H_2S is considered sour according to Alberta Energy Regulator [22]. Hydrogen sulphide is toxic, flammable, and can damage drilling equipment. Both H_2S and CO_2 can corrode piping during gas production and transportation. When NG is liquefied to be transported, the CO_2 needs to be removed as it freezes and

blocks the flow lines. Therefore, sour gas has different infrastructure requirements and needs to be directed to dedicated sour gas pipelines and processing facilities before entering a sales gas line [21]. The additional cost of the specialized infrastructure to condition the sour gas often makes processing uneconomical, especially at low flow rates. For these reasons, associated sour gas is typically flared.

2.1.1 Flare Stage

Flaring occurs under three main scenarios: emergency flaring, process flaring, and production (upstream) flaring [1]. Emergency flaring is used to protect personnel and infrastructure due to unplanned and emergent events, typically at large facilities such as refineries and gas plants. In these scenarios all production is redirected to the flare, so flow rates through the flare can be very high, resulting in large flames. In these cases, irradiation of surrounding structures must be considered [23]. Process flaring is used to discard gases from typical process discharges as relief valves or condensate separation. Process flaring is located in refineries, sour gas plants, and petrochemical plants. Excluding unique situations (start-up, shutdown, or evacuation and blowdown), process flaring involves a constant low flow rate of process gas, far less than typical of emergency flaring [24]. Finally, production flaring, or upstream flaring, refers to all types of flaring during production at oil and gas fields. This category includes the well-test flare, which continuously burns gas at high flow rates for several days when initiating a gas well, often without smoke suppression or enhanced flame stability devices. Production flaring involves a wide range of gas composition and fuel flow rates. Oil extraction is habitually linked to flammable gas production, even when no gas is initially present in the reservoir [21].

Production flaring is responsible for 90% of the flared gas volume globally, and is used mainly for processing associated gas [2,25]. Production flares are generally simpler than the flare stacks used for emergency and processing flaring, in which steam- or air-assisted smoke suppression is common.

A typical upstream gas flare stack from Alberta is shown in Figure 2; it consists of a 10 m high straight pipe with a 10 cm internal diameter. The flare tip may include a wind shroud, a coaxial cylinder opened on both sides with a larger diameter to protect the flame base from strong crosswinds, and an automated ignition system to ensure that the flare remains lit [1].

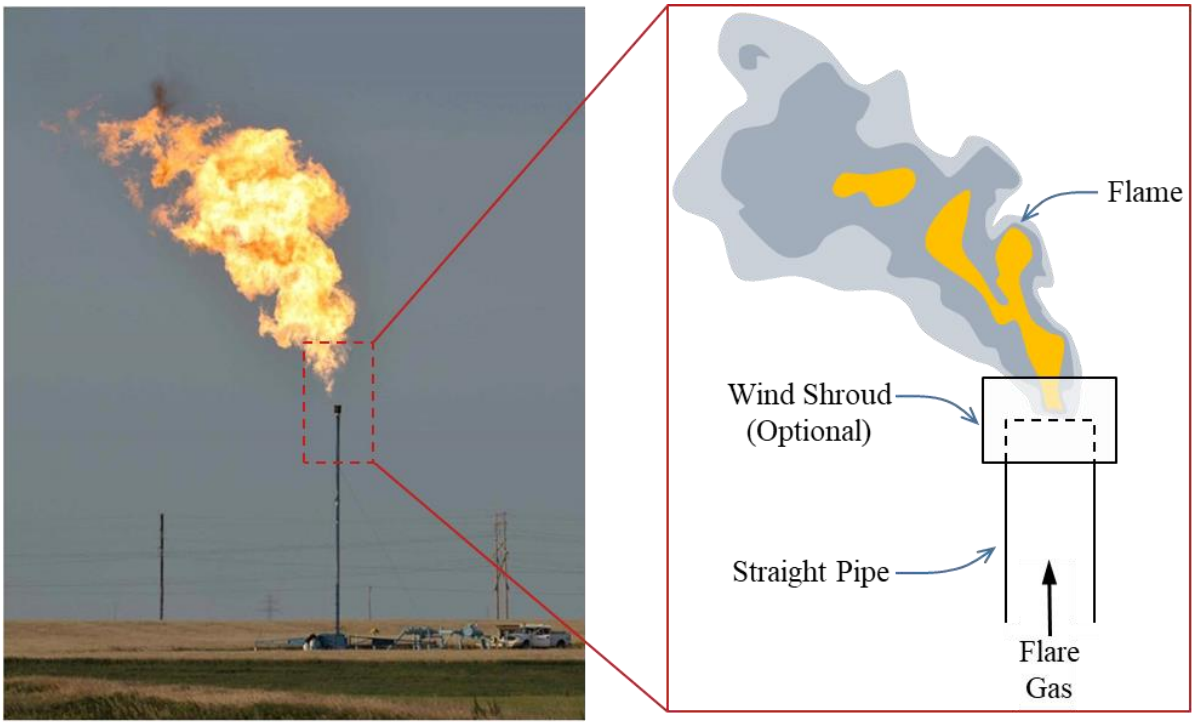

Figure 2 Typical production flare stack [2,26].

Flares in the upstream production phase are the most numerous type of flare. As this kind of flare is simpler than the others, it is also the most susceptible to factors that lower combustion efficiency. Additionally, sour gas processing is more complex and uneconomical, making sour gas flaring more common than sweet gas flaring. Lastly, flaring is commonly collocated with oil extraction wells, as associated gas is almost always present and needs disposal.

2.2 Natural Gas Combustion

Flaring transforms the unwanted NG hydrocarbons into CO_2 through combustion. Under ideal, stoichiometric conditions, the combustion reaction of hydrocarbons is given by

$$C_xH_y + (x + \tfrac{y}{4})O_2 \rightarrow xCO_2 + \tfrac{y}{2}H_2O\,, \tag{2.1}$$

where *x* and *y* are the numbers of carbon and hydrogen atoms in the hydrocarbon molecule, respectively. Nitrogen oxides (NO_x) can also form through thermal, prompt, and fuel mechanisms, but these are usually of secondary importance. Under ideal conditions, enough oxygen is provided to convert all hydrocarbons into CO_2 and H_2O. However, the oxygen supply can be locally limited by mixing difficulties between air and fuel. Therefore, other combustion products can be formed in the process via

$$C_xH_y + aO_2 \rightarrow bCO_2 + dH_2O + eCO + \sum_{m,n} f_{m,n}C_mH_n\,. \tag{2.2}$$

New hydrocarbons that are not initially present in the reactant fuel can be produced through this reaction, which are then released into the atmosphere in the gas phase or may condense into soot. Since CH_4 is the main component of NG, as shown in Table 2, the predominant reaction is

$$CH_4 + aO_2 \rightarrow bCO_2 + dH_2O + eCO + f\,CH_4 + gC_{soot} + \sum_{m,n} h_{m,n}C_mH_n\,. \tag{2.3}$$

Methane and soot are isolated from the other hydrocarbon products since they tend to be present in higher concentrations and are most important from the perspective of flaring CE.

Crosswinds may disturb the combustion process. The mixing caused by the crosswinds affects the transition from laminar to turbulent flow at the flare tip, thereby altering the mixing of the combustion reactants in Eq. (2.3).

2.3 Combustion Efficiency

The flare efficiency in transforming the unwanted hydrocarbons to CO_2, and H_2O can be quantified by the combustion efficiency, η_{comb}, [27]

$$\eta_{comb} = \frac{\dot{m}_{C,CO2}}{\dot{m}_{C,fuel}}, \tag{2.4}$$

where $\dot{m}_{C,CO2}$ is the mass flow of carbon in the form of CO_2 produced by the flame, and $\dot{m}_{C,fuel}$ is the mass flow rate of carbon entering the flame in the form of hydrocarbon fuel, as shown in Figure 3. The mass flow rate of carbon in the form of the i^{th} species is defined as

$$\dot{m}_{C,i} = \frac{M_C}{M_i}\dot{m}_i = \frac{M_C}{M_i} w_i \dot{m}_{plume} = \frac{M_C}{M_i}\chi_i M_i \dot{n}_{plume} = \chi_i M_C \dot{n}_{plume}, \tag{2.5}$$

where M_C is carbon molar mass (12.011 g/mol), M_i is the i^{th} species molar mass, and $\dot{m}_i$ is the species mass flow. Alternatively, this quantity can be calculated from the species mass fraction w_i and the combustion products mass flow rate, $\dot{m}_{plume}$, or the species volume fraction χ_i and the molar flow rate of combustion products, $\dot{n}_{plume}$. The combustion efficiency, Eq. (2.4) can be combined with Eq. (2.5) to write CE in the molar flow rates form assuming a generic hydrocarbon as fuel,

$$\eta_{comb} = \frac{\dot{n}_{CO2}}{x\dot{n}_{CxHy}}. \tag{2.6}$$

In principle, provided the fuel flow and its composition, a simple measurement of CO_2 in the flame products can quantify the CE. However, the fuel composition and flow are generally not measured in real-time and can change significantly throughout the flaring process. Additionally, a method that does not rely on the fuel flow provided by the flare operators is desired in order to support independent fenceline measurements. Consequently, the CE should be estimated by measuring the most abundant, carbon-containing combustion products. Through conservation of species, the combustion

efficiency of a flare burning CH_4 can be written by substituting the fuel mass flow on Eq. (2.4) with the mass flow of combustion products from Eq. (2.3),

$$\eta_{\text{comb}} = \frac{\dot{m}_{\text{C,CO2}}}{\dot{m}_{\text{C,CO2}} + \dot{m}_{\text{C,CO}} + \dot{m}_{\text{C,CH4}} + \dot{m}_{\text{C,soot}} + \sum \dot{m}_{\text{C,C}m\text{H}n}}. \tag{2.7}$$

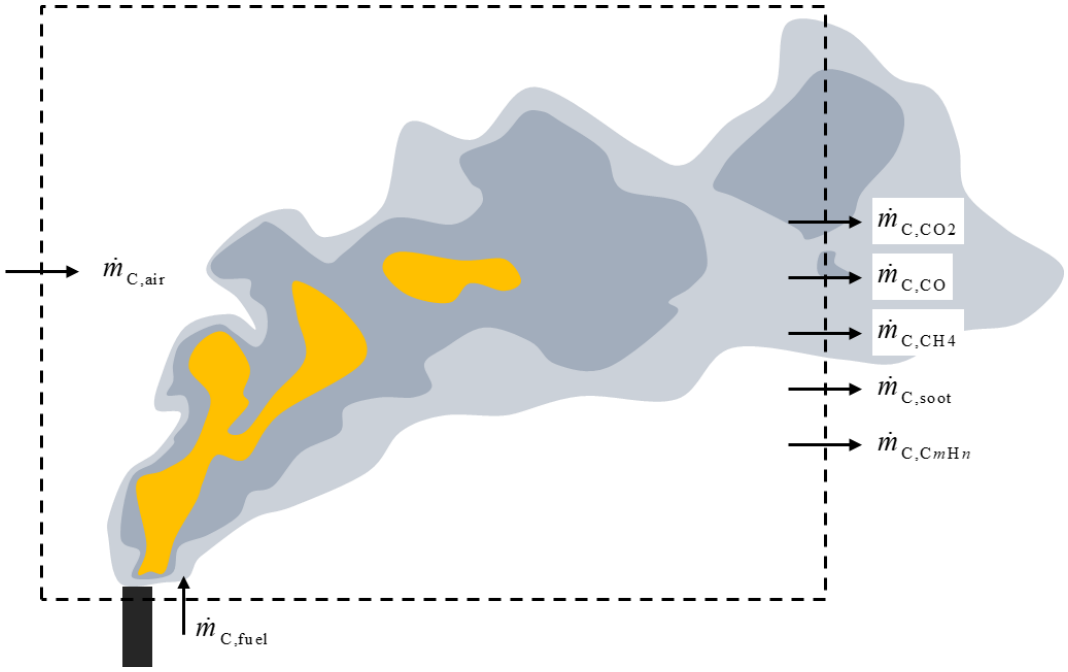

Figure 3 Flare mass flow of carbon balance over the control volume.

Equation (2.7) shows that the CE can be estimated by measuring only the mass flow rate of carbon-containing combustion products in the flare plume. The CE estimate can be further simplified since the contribution of soot is generally less than 0.5% to the overall carbon balance in the case of heavy hydrocarbon fuels [27,28], and less than 0.1% of the carbon-based combustion products for methane-dominated natural gas [29]. Therefore, soot can be neglected when calculating the CE. Although additional hydrocarbons are formed as intermediate steps in CH_4 combustion, they are in

minimal quantities and are typically oxidized in the plume [10,28]. As a consequence, the CE, Eq. (2.7) can be simplified into

$$\eta_{\text{comb}} = \frac{\dot{m}_{\text{C,CO2}}}{\dot{m}_{\text{C,CO2}} + \dot{m}_{\text{C,CO}} + \dot{m}_{\text{C,CH4}}}. \tag{2.8}$$

This equation is further simplified by noting that the primary source of carbon conversion efficiency is due to unburned fuel [27,29]. In the case of steam-assisted flares, steam inhibits the formation of CO by increasing the concentration of OH radicals in the flame, promoting the CO oxidation reaction [30]. Consequently, the CO mass flow can be neglected in Eq. (2.8). If products of combustion are well-mixed downstream of flame, the overall CE can be approximated as the local CE. The local CE can be defined in terms of the volume fraction of each species as,

$$\eta_{\text{local}} = \frac{\chi_{\text{CO2}}}{\chi_{\text{CO2}} + \chi_{\text{CO}} + \chi_{\text{CH4}}}. \tag{2.9}$$

However, in cases where unburned fuel is segregated from the combustion products, this procedure can overestimate the real CE.

Measuring the CE in flares using extractive sampling is an arduous task, as the assumption of well-mixed combustion products does not always hold. In this scenario, the overall CE cannot be assumed equal to the local CE at the sampled point in the plume. On the other hand, collecting the whole emissions from the flame is possible only in laboratory studies. Even when all the combustion plume is collected, it is highly diluted with ambient air; consequently, the ambient concentration of species strongly influences CE estimates.

Flare CE calculation errors will vary with the ambient species concentration and air dilution [29]. Several studies handle this problem with different assumptions and approaches [8,10,27,28,31]. The most precise method for calculating CE with air dilution is given by [29]

$$\eta_{comb} = \frac{x\left(X_{CxHy,\,fuel}\right)B - X_{CO2,\,fuel}F + \left[X_{CO2,\infty}G - X_{CO2,\,plume}\left(X_{CO,\infty} + X_{CH\,4,\infty} + \sum_i xX_{CxHy,\infty}\right)\right]\frac{M_{fuel}}{M_\infty}}{xX_{CxHy,\,fuel}\left(X_{CO2,\,plume} - X_{CO,\infty} + F\right)} \tag{2.10}$$

and

$$\begin{bmatrix} B \\ F \\ G \\ H \end{bmatrix} = \begin{bmatrix} X_{\mathrm{CO2,plume}} - X_{\mathrm{CO2},\infty} \\ X_{\mathrm{CO,plume}} - X_{\mathrm{CO},\infty} + X_{\mathrm{CH4,plume}} - X_{\mathrm{CH4},\infty} + \sum_i x\left(X_{\mathrm{CxHy,plume}} - X_{\mathrm{CxHy},\infty}\right) + H \\ X_{\mathrm{CO,plume}} + X_{\mathrm{CH4,plume}} + \sum_i xX_{\mathrm{CxHy,plume}} + H \\ \dfrac{\rho_{\mathrm{soot}}\chi_{\mathrm{soot}}R_{\mathrm{u}}T_{\mathrm{plume}}}{M_{\mathrm{soot}}p_{\mathrm{plume}}} \end{bmatrix} \tag{2.11}$$

where X are the species mole fractions, ρ_{soot} is the soot density, χ_{soo} is the soot volume fraction corrected to plume temperature, R_{u} is the universal gas constant, T_{plume} and p_{plume} are plume temperature and pressure, respectively. The term H can be set to zero if soot is neglected with good accuracy compared to the full version.

Several studies have endeavoured to measure flare combustion efficiency. Pohl et al. characterized the plume composition of a full-sized flare with the objective of quantifying the effect of soot on the CE calculations, the consequence of considering local CE measurement as overall flare CE, and how CE changes with the size of the flares. Combustion products were extracted from 15 plume positions simultaneously for 20 minutes [28]. The results generated detailed radial and axial combustion products concentration and local CE profiles. The probe area and velocities estimated from jet theory were used to weigh the local CE to obtain the overall CE. The authors collected all the combustion products for small flames, mixed them, and sampled them to confirm material balances and acquire the overall CE. The main conclusions of this study are that: soot has a minor influence in CE, less than

0.5% for sooty flames; using local CE as overall CE results in a slight overestimating of the overall CE; strict closure of mass balance is not necessary to measure the CE; the CE is insensitive to flare diameter. Most unconverted carbon appears as unburned hydrocarbon from fuel in the combustion products, while carbon monoxide plays a comparatively minor role in the overall carbon balance. The authors also discussed using remote techniques to measure the CE, but the methods available in 1986 are primitive compared to today's standards.

Closed-loop wind tunnels have been used to study the influence of crosswinds on the CE. The importance of the crosswind effect depends, in part, on the wind speed relative to the fuel velocity [32]. The flare CE can be calculated using the accumulated balance of species in the system. CO_2 is the most critical species, and an error of 5% on its concentration can generate deviations of 0.4% on the CE measurements from laboratory-scale flares [33]. Johnson and Kostiuk used a closed-loop wind tunnel to characterize the flare CE for different crosswind conditions. The flare CE decreases with the increased crosswind speed, whereas increasing the jet exit velocity makes the flame less susceptible to the crosswind effects [34]. The study also shows that CE decreases abruptly at a crosswind speed threshold depending on the fuel composition.

It is also possible to measure the species distribution downwind of the flare using multipoint sampling in the plume. The plume behaves similarly to a non-reacting buoyant jet, although the CO_2 is concentrated in the plume center, and CH_4 and CO are more abundant on the plume sides [27]. The plume can assume different structures and, consequently, distinct local CE distributions, under different operating conditions. In the case of flares in a crosswind, the combustion products plume can assume three basic shapes depending on the relative velocities of the fuel leaving the stack and the crosswind. For low crosswind velocities, the plume assumes a kidney shape on a plane perpendicular to the flow, as shown in Figure 4 (a). This effect is caused by the counter-rotating vortices formed on the stack

affecting the lower part of the plume, even though the plume is above the stack tip. As the wind speed increases or fuel injection velocity decreases, the plume moves downward and assumes a circular shape with a small part of the combustion products trapped underneath. The trapped combustion products are caused by the influence of wake structures created by the stack, shown in Figure 4 (b). Finally, at the highest crosswind velocities a downwashed plume forms, and a second peak of combustion product concentration appears below the stack tip height. Most of the flame region moves to the stack recirculation zone, and the entire flame is affected by the stack wake structure, as shown in Figure 4 (c).

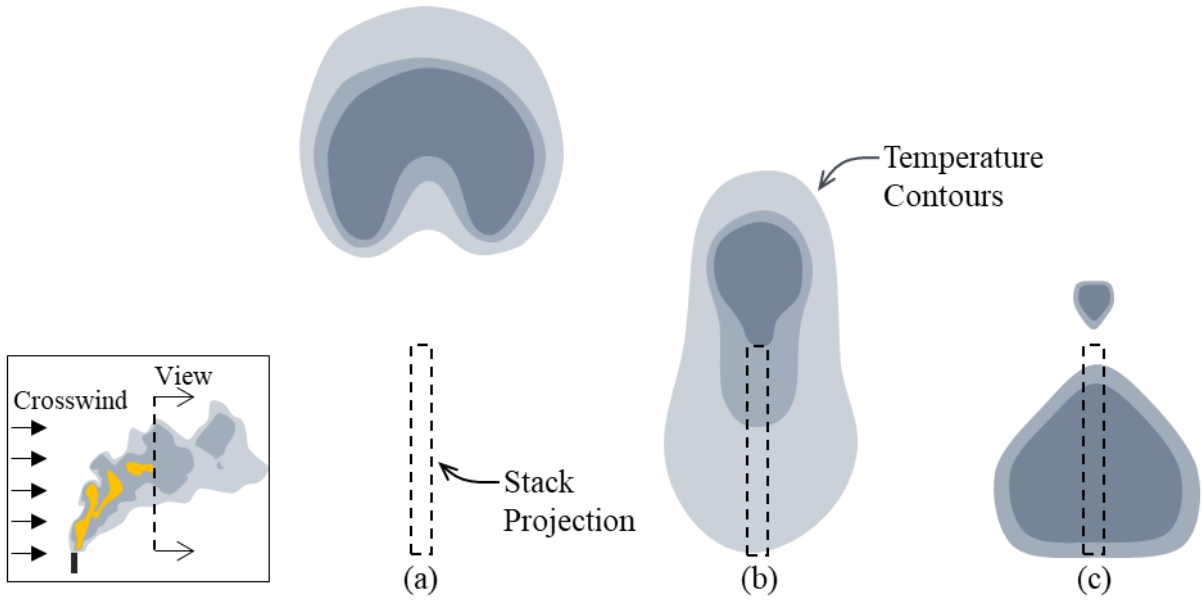

Figure 4 Temperature profile effect scheme on the variation of wind velocity (U_∞) in relation to the fuel jet velocity (V_j) in a plane at downwind the NG flare stack: (a) kidney shape plume $1<U_\infty/V_j^{1/3}<5$ $(m/s)^{2/3}$, (b) circular shape plume $5<U_\infty/V_j^{1/3}<7.5$ $(m/s)^{2/3}$, and (c) downwashed shape plume $7.5<U_\infty/V_j^{1/3}<10$ $(m/s)^{2/3}$, adapted from [27].

2.3.1 Fuel Stripping Mechanism

In the case of a flare in a crosswind, the primary source of combustion inefficiency arises from unburned fuel and can be explained by the stripping mechanism. The stripping mechanism of fuel in wake-stabilized flames can be divided into three parts, as shown in Figure 5 [35]. The images represent the evolution of an unburned fuel packet and show the characteristic flame pockets formed in the wake-stabilized flame. As the coherent turbulent structures move downstream from the flare tip, they entrain fuel, and the lean concentration of fuel between the pockets causes local extinction of the flame. Most fuel is burned in these "flame pockets" and the recirculation zone behind the flare stack. The low pressure in the recirculation zone forms vortices that drive the unburned fuel downward between these pockets into a region beneath the flame. The surging of unburned fuel occurs along the entire length of the flame as the horizontal velocities of the flame pockets and unburned fuel are the same. However, the flame pockets and unburned fuel are separated by buoyant forces, which drive the flame pockets upward. In contrast, the unburned fuel is colder and moves horizontally with the surrounding air. The amount of unburned fuel is more prominent beneath the flame, and the region of the plume downstream of the flame is a minor source of unburned fuel.

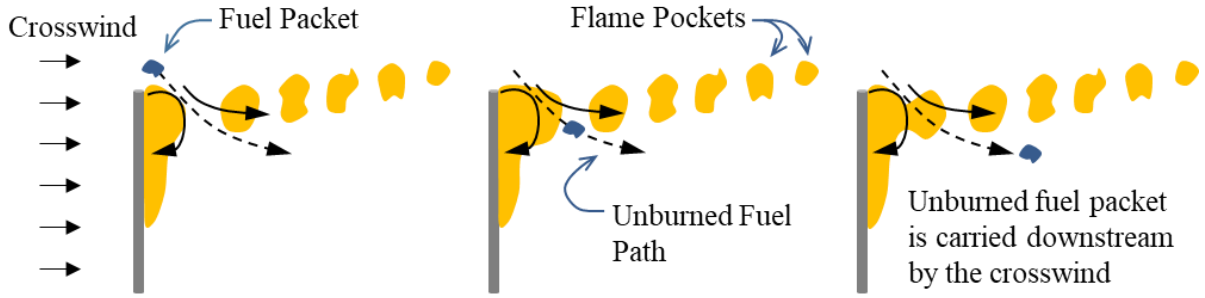

Figure 5 Wake stabilized flames evolution in time of the fuel stripping mechanism, adapted from [35].

2.3.2 Assisted Flares

Injecting air or steam into the flared gas near the stack exit can create “smokeless” and high-efficiency flares. The additional flow increases the gas exit velocity, enhances turbulence mixing of fuel and air, and improves fuel combustion [36]. Additionally, the mixing reduces soot, luminosity, and thermal radiation from the flame [37].

Steam injection adds momentum to the fuel exit, helps to reduce smoke by dilution, and participates in the combustion reaction. Consequently, steam injection is more effective in reducing smoke than air injection, and air assistance is only used when steam is not available [38]. Although water vapour reacts with combustion in several ways, the primary mechanism that suppresses smoke is caused by radicals that inhibit the formation of carbon particles [30]. Water dissociation at flame temperature produces H- and -OH radicals, facilitating the carbon conversion into gaseous CH_2- and -CHO radicals instead of forming soot.

Although the assistance fluid reduces smoke from the flare, soot does not account for a considerable portion of flare hydrocarbon emissions. Furthermore, while lower injection rates may reduce gas-phase emissions through improved mixing, excessive amounts of air- or steam-assist leads to partial flame extinction, releasing unburned fuel [39]. The effects of excessive amounts of steam- and air-assist on flare emissions are easy to replicate in the laboratory, allowing the control of combustion efficiency and complete capture of the plume [36].

In addition to the studies commented above, Torres and coworkers [10,40,41] conducted a comprehensive series of full-scale flare CE measurements based on extractive sampling and optical measurements. The studies focus on low-flow and low fuel lower heating values conditions. The authors used stack diameters of 610 mm and 915mm (24” and 36”), which were air-assisted and steam-

assisted, respectively. The fuel was diluted with nitrogen to control the fuel's lower heating values. One of the study's objectives was to determine whether flares actually achieve 98% CE over realistic operating conditions. Another goal was to assess the feasibility of emissions quantification using competing remote sensing techniques. The observed CE was between 50% to 99% for all flares, and generally above 90% and 95% for air- and steam-assist flares, respectively. However, flare emissions were several times above those estimated using emission factors under some experimental conditions. A comparison of remote sensing performance using a single-blind approach is included in the study report. Two independent contractors did plume measurements using an IFTS (Telops Inc.), and a passive and active Fourier transform infrared (PFTIR, AFTIR) spectroscopy (Industrial Monitor and Control Corporation). The PFTIR and AFTIR provide the spectral data along a single LOS, while the IFTS provides the spectral data in a two-dimensional array of LOS, represented by pixels. The PFTIR and IFTS record the radiation emitted by the gas against an ambient background, while the AFTIR makes absorption measurements and requires an artificial radiative source as background. While the requirement of a radiative source significantly complicates the experimental apparatus and would be infeasible under most real conditions, the absorption-only measurement is more straightforward, and it facilitates the quantification of colder gases that may not be visible in strictly emissions-based measurements. The test description of PFTIR and AFTIR can be found at Wormhoudt et al. [42]. The CE values inferred using PFTIR and AFTIR were within 2.5% of probe-derived measurements, while IFTS was within 15%. The remote measurements teams were required to process their results within six weeks of the campaign, which was not possible for the IFTS because of the challenges of this measurement. Although the IFTS generates the same data as PFTIR for each camera pixel, the longer

measurement time needed to obtain the data cube increases the errors caused by scene changes artifacts (SCAs)[6].

2.4 Conclusions

Globally, production flaring is responsible for the greatest volume of flared gas and the largest number of flares stacks. The NG in the production phase is a by-product of oil extraction. It is categorized as associated gas, typically wet and sour. Even in the case of wet gas with more heavy hydrocarbons, CH_4 is the main component, accounting for at least 84% of the gas composition by volume. Furthermore, production flares stacks are simpler in design, and are therefore more susceptible to combustion inefficiencies.

The objective of production flaring is to transform the associated gas in CO_2 through combustion. However, crosswind turbulence can generate regions outside the fuel flammability range, generating unburned fuel emissions. The primary source of combustion inefficiencies is unburned fuel, while soot and heavier hydrocarbons have negligible impact on CE estimates. Although assisted flares are less common compared to production flares, excessive use of assistance fluid produces unburned fuel, and can therefore be a significant contributor to overall methane emission rates from flares.

Local flare combustion efficiency has been measured using probes or along a single line-of-sight using spectrometers, but the fact that the method only gives the concentration of a gas species at a point inherently limits the reliability of quantities like emission fluxes that must be integrated over a volume or area. For this reason, combustion efficiencies derived from point measurements are known

[6] Causes and effects of SCAs will be discussed in Section 3.1.4

to overestimate the true CE [28]. Another problem with using physical measurements methods is that flares are often in areas difficult to access or require personnel to work under hazardous conditions. Flare CE can be better estimated by measuring the mass flow rate of carbon-containing combustion products in the flare plume.

Advances in MWIR optoelectronics make standoff flare CE measurements theoretically possible. QOGI is widely used to identify and quantify emissions of methane and other gases and is well-suited to this task. The resulting two-dimensional imaging can be used to map gas species concentrations spatially. QOGI is particularly useful in scenarios where gas species concentration and velocity are non-uniformly distributed within a plume.

Chapter 3

Quantitative Optical Gas Imaging

Flare plumes often provide limited physical access, and species and temperature vary temporally and spatially. As a result, there is a movement towards using optical techniques to estimate flare CE from standoff measurements. Multispectral cameras, which produce images integrated over multiple spectral bands, and hyperspectral cameras, which generate a hypercube of images, each at a discrete wavelength, have been used in conjunction with Beer-Lambert-type spectroscopy for quantitative remote sensing [43]. The possibility of generating a two-dimensional representation field of gas column densities makes it possible to visualize species distribution within the entire plume. This data is then combined with a velocity field, inferred from the apparent motion of pixels between frames, to obtain the total mass flow of each species. This chapter will first discuss the procedure for estimating column densities, followed by the velocimetry algorithm, and, finally, how these parameters are combined to estimate the CE.

3.1 Infrared Spectroscopy

Spectroscopy involves identifying and quantifying molecules by analyzing the interaction between light and matter as a function of wavelength or frequency. The absorption coefficient of molecular gases varies strongly with wavelength because molecules can only occupy discrete (quantized) energy levels. The absorption coefficient in the IR region depends on the quantum spacing of these levels, as shown in Figure 6, as well as the temperature, pressure, and concentration of the species.

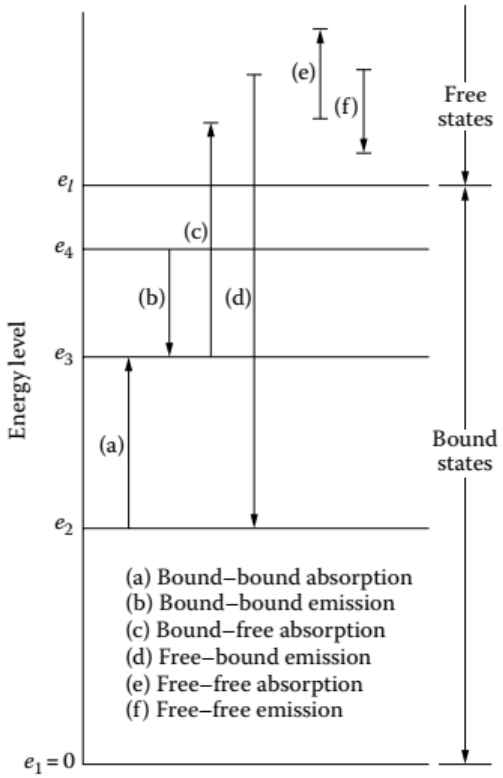

Figure 6 Schematic diagram of energy states and transitions for atom or ion. e_1 is the ground state and e_l the ionization energy for the gas [44].

At IR wavelengths, gas molecules undergo transitions between bound energy states. Thus, only photons having the exact amount of energy required for the molecule to transition from one state to another can be absorbed. For instance, a photon with energy equal to e_3-e_2 will be absorbed, and the molecule will change state from e_2 to e_3, energy jump (a) from Figure 6. Meanwhile, a molecule changing state from e_3 to e_2 will emit a photon having an energy e_3-e_2.

Photons having energy, e_p, corresponds to an electromagnetic wave having a wavelength λ or a wavenumber $\eta = 1/\lambda$ according to

$$e_p = e_j - e_i = hc\eta_{ij}, \tag{3.1}$$

where h is Planck's constant, c is the speed of light, and η_{ij} is the line central wavenumber, e_j and e_i are the levels of energy that a particle can assume [44].

In the case of polyatomic molecules, emission and absorption of infrared radiation involves simultaneous transitions between vibrational and rotational states. Transitions between rotational levels of the same vibrational level in the same electronic state involve low energy photons, corresponding to spectral lines in the far-IR region. Meanwhile, transitions between rotational levels of different vibrational states involve photons in the near to mid-IR region. Only diatomic or polyatomic molecules have vibrational-rotational states and therefore emit/absorbs photons in this spectral region. Consequently, molecules with more atoms have a higher number of spectral lines than simple molecules. The difference in spectral lines generates a "fingerprint" for each molecule that allows identification and, in principle, quantification.

3.1.1 Absorption Coefficient

The spectral absorption coefficient is proportional to the probability of a photon encountering a molecule along the optical path having a quantum transition that matches the photon's energy. In principle, the spectral absorption coefficient should thus be represented by a series of infinitesimally-thin vertical lines at the specific wavenumbers corresponding to possible transitions between quantized energy levels. However, in reality, various phenomena cause the spectral lines to broaden, as shown in Figure 7. The broadened line structure is defined by the line intensity, S_{ij}, the line width, along with the line shape; these parameters relate the spectral absorption coefficient with the temperature and concentration of the gas species.

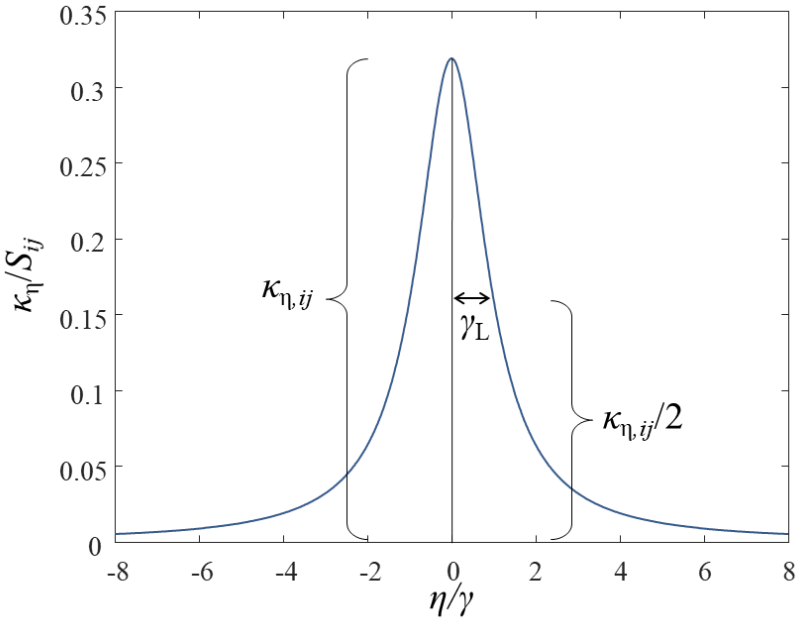

Figure 7 Lorentz line profile.

The broadening mechanisms are natural broadening, Doppler broadening, Stark broadening, and collision broadening. In most molecular gases, broadening is dominated by collision and Doppler broadening. Collision broadening is caused by the varying repulsive or attractive forces between colliding molecules, which change the energies requires to transition from one energy state to another. Collisions between neutrally-charged particles result in a Lorentzian line shape

$$\frac{\kappa_{\eta,ij}}{S_{ij}} = \frac{\gamma_L/\pi}{\gamma_L^2 + (\eta - \eta_{ij})^2} \cdot \frac{\chi p}{k_b T} \tag{3.2}$$

where S_{ij} is the line intensity, which is the area under the line profile, and γ is the line half-width at half-maximum (HWHM), as shown in Figure 7. The collision half-width is determined by the collision rate, which depends on the pressure and molecule collision cross-section. In the case of mixtures, it is important to note that, in addition to collisions between molecules of the species of interest ("self-

broadening"), collisions between molecules of other species should also be accounted for. When the balance of the gas mixture is air, this is termed "air-broadening" and is primarily due to collisions between the target species and nitrogen molecules.

Doppler broadening is caused by the velocity distribution associated with the thermal energy of the gas molecules, which generates a shift in the photon wavenumber depending on the velocity of the molecule relative to the observer. As the velocity of the molecules in one direction obeys a Maxwell-Boltzmann distribution, the effect of Doppler broadening is a Gaussian lineshape. However, the impact of Doppler broadening depends on the molecular velocity, which in turn depends on the gas temperature. The Doppler broadening effect can be neglected at relatively low temperatures and normal pressures. Figure 8 shows the Gaussian lineshape generated by the Doppler broadening effect compared to the Lorentz profile caused by collision broadening.

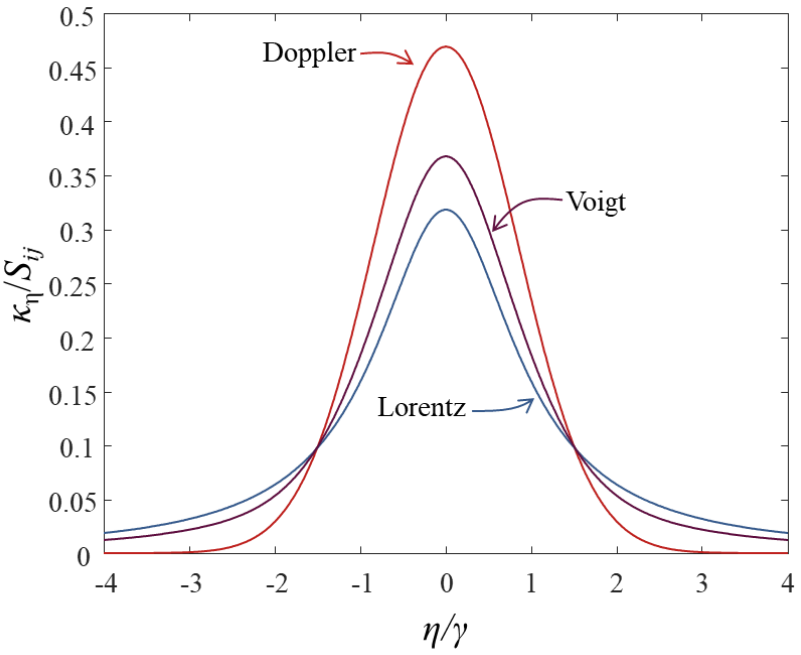

Figure 8 Doppler, Lorentz, and Voigt lineshape for the same HWHM and line strength.

The Voigt shape accounts for the effects of collision broadening (Lorentzian line shape, f_L) and the Doppler effect (Gaussian line shape, f_D). Figure 8 shows a Voigt profile assuming equal HWHM for the Gaussian and Lorentz profiles. Although the Voigt profile is typically used in combustion applications [45], in the flare plume Doppler broadening effects should be negligible due to the ambient pressure and relatively low temperatures downstream of the flame. The Whiting correlation was used to generate the Voigt lineshape computing the convolution of Lorentz and Gaussian profiles. The Whiting correlation return errors of less than 3% to the real Voigt profile with low computational cost and it converges precisely to pure Lorentz profile when the Doppler effect is neglectable [46]. The Voigt lineshape was implemented using the algorithm described by Gharavi and Buckley [45]

$$f_V = \sigma_0 \left\{ (1-x_V)\exp\left(-0.693 y_V^2\right) + \frac{x_V}{1+y_V^2} + 0.016(1-x_V)x_V \left[\exp\left(-0.084 y_V^{2.25}\right) - \frac{1}{1+0.0210 y_V^{2.25}} \right] \right\} \tag{3.3}$$

where $x_V = \gamma_L/\gamma_V$ is the ratio between Lorentz lineshape HWHM and Voigt lineshape HWHM, and $y_V = |\eta - \eta_{ij}|/\gamma_V$. The Voigt HWHM is given by the following equation

$$\gamma_V = 0.5346\gamma_L + \left(0.2166\gamma_L^2 + \gamma_D^2\right)^{0.5}, \tag{3.4}$$

where γ_D is the Doppler HWHM. The normalized center line strength is given by

$$\sigma_0 = \frac{1}{2\gamma_V\left(1.065 + 0.447 + 0.058 x_V^2\right)}. \tag{3.5}$$

In the case of common atmospheric molecules, the line parameters needed to calculate the line profile, i.e., line intensity, line HWHM, and line position, are available in the HITRAN database [47]. In this study, the CH_4, CO_2, CO, and H_2O parameters were obtained from HITRAN. Each line is

generated independently, and the absorption coefficient of the gas is the summation of the absorption coefficients of each spectral line, as shown in Figure 9, known as the line-by-line (LBL) approach

$$\kappa_{\eta,\mathrm{m}} = \sum_{\mathrm{ij}} \kappa_{\eta,\mathrm{ij}} \,. \tag{3.6}$$

Although simplified models (narrowband, wideband, and global models) are used for quantitative heat transfer calculations, the LBL method is the most accurate model.

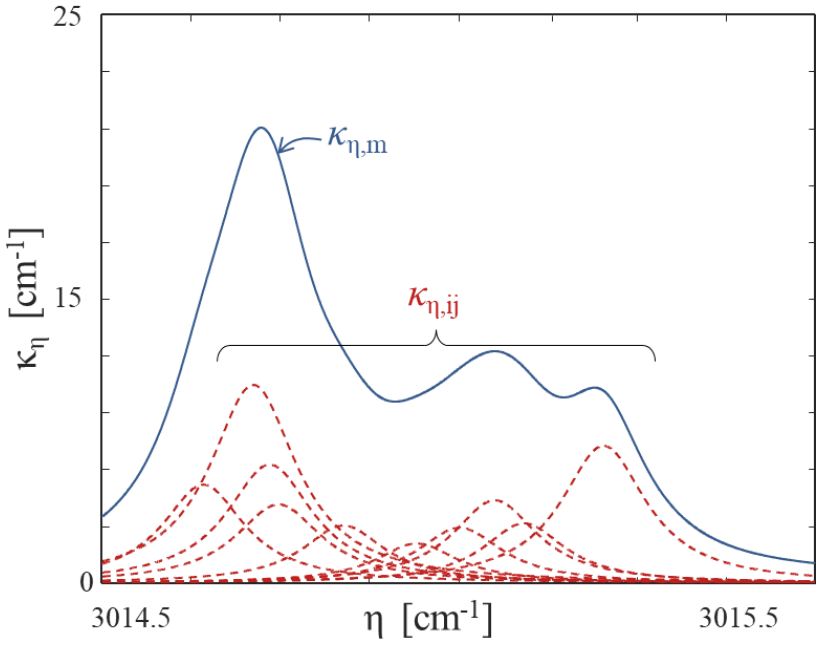

Figure 9 Methane absorption lines and absorption coefficient.

The transition-specific coefficient for each molecule is given by

$$\kappa_{\eta,ij}(s) = S_{ij}\left[T(s)\right] f_{\mathrm{V}}\left[\eta,\eta_{ij},T(s),p\right]\frac{\chi(s)\,p}{k_{\mathrm{B}}T(s)}, \tag{3.7}$$

where S_{ij} is the spectral line intensity of the ij^{th} molecule transition, k_{B} is the Boltzmann constant.

Lookup tables were created for each species as a function of wavenumber, temperature, volume fraction, and pressure, to reduce the computational cost of the LBL approach. A spectral band is composed of one cold and several hot bands characterized by excited vibrational lower levels. As the temperature increases, the hot bands become more important. Usually, ten bands are used for CO_2 at 300 K instead of more than two hundred bands that contribute considerably to absorption at 3000 K [48]. The absorption coefficient of CO_2 over 4.3 μm (2325 cm^{-1}) band for 300 K and 800 K is shown in Figure 10. At 300 K the spectral lines are more prominent at the band center, but at high temperatures, hot bands become stronger while the cold band becomes weaker, which increases the prominence of the band wings. These effects are particularly important for two reasons. First, hot gas will emit more on the band wings in nonuniform temperature LOS profiles, and cold gas will absorb more on the band center; consequently, absorption by ambient species between the plume and the camera is most pronounced at the band center. In the case of CO_2, this manifests as red and blue "spikes" in the measured spectrum. Second, the volume fraction affects the absorption coefficient almost linearly as the effect of self-broadening is weak on the species like CO_2 [49].

Different species of a gas mixture can absorb and emit simultaneously over the same spectral region. However, there is no significant correlation between the spectra of distinct species, and the absorption coefficients of the species can be modelled as independent. Therefore, the spectral absorption coefficient of a mixture at any point is found by

$$\kappa_{\eta,\mathrm{mix}} = \sum_{\mathrm{M}} \kappa_{\eta,\mathrm{m}} , \tag{3.8}$$

where $\kappa_{\eta,\mathrm{m}}$ is the absorption coefficient of each species of the mixture. This assumption means that the collision broadening between two species in the gas mixture is approximated as collisions between one species and air. Although recent updates on the HITRAN database contain collision broadening caused

by H_2O for different species [50], this effect is expected to be small and is excluded from this analysis. The used lookup tables approach is only possible assuming that the mixture absorption coefficient is the sum of each species' absorption coefficient. Knowing the gas state makes it straightforward to obtain the gas mixture's absorption coefficients necessary to model the radiative intensity that reaches measurement equipment.

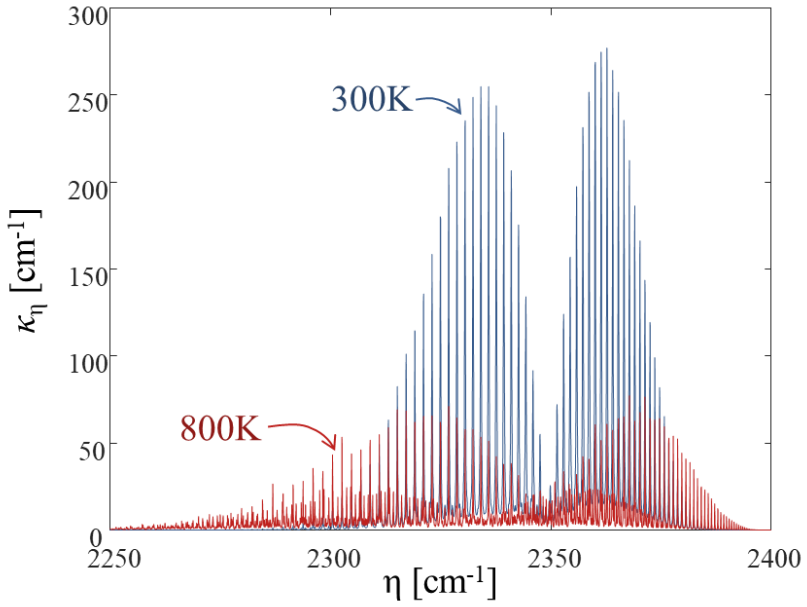

Figure 10 Absorption coefficient of pure CO_2 at 300 K and 800 K.

3.1.2 Radiative Transfer Equation

The radiative transfer equation (RTE) represents the change in spectral intensity along a LOS caused by absorption, emission, and attenuation or augmentation by scattering in a wavenumber. In differential form, the RTE is given by

$$\frac{dI_\eta}{ds} = -\beta(s) I_\eta(s) + \kappa_\eta(s) I_{b\eta}(s) + \frac{\sigma_{s\eta}(s)}{4\pi} \int_{\Omega_i=4\pi} I_\eta(s,\Omega_i) \Phi_\eta(s,\Omega,\Omega_i) d\Omega_i \tag{3.9}$$

where I_η is the spectral intensity in the wavenumber η, $\sigma_{s\eta}$ is the scattering coefficient, and $\beta = \kappa_\eta + \sigma_{s\eta}$ is the extinction coefficient. The scattering phase function is Φ, Ω is the solid angle, s is the distance in the LOS, and $I_{b\eta}$ is the blackbody intensity at the gas temperature given by Planck's law. In the case of molecular gas at IR wavelengths, scattering can be neglected. With this assumption, Eq. (3.9) can be rewritten as

$$\frac{dI_\eta}{ds} = -\kappa_\eta(s) I_\eta(s) + \kappa_\eta(s) I_{b\eta}(s), \tag{3.10}$$

and in the integral form with LOS length parameter equal to s and total length equals to L,

$$I_{L\eta} = I_{0\eta} \exp\left(-\int_0^L \kappa_\eta(s) ds\right) + \int_0^L \kappa_\eta(s) I_{b\eta}(s) \exp\left(-\int_s^L \kappa_\eta(s') ds'\right) ds, \tag{3.11}$$

where $I_{L\eta}$ is the radiative spectral intensity that reaches a detector at L, and $I_{0\eta}$ is the background radiation. The exponential term multiplying the background radiation is the fraction of radiation transmitted through the gas, as demonstrated in Figure 11. The rightmost term of Eq. (3.11) accounts for the emission from the hot gas, and the exponential part accounts for self-absorption through the remaining gas in the LOS.

If the gas is optically thin (i.e., the gas concentration is low along the LOS, or the absorption coefficient is weak in the particular wavenumber), reabsorption of the plume's emission is negligible. In this scenario, Eq. (3.11) can be further simplified and rewritten as

$$I_{L\eta} = I_{0\eta} \exp\left(-\int_0^L \kappa_\eta(s) ds\right) + \int_0^L \kappa_\eta(s) I_{b\eta}(s) ds. \tag{3.12}$$

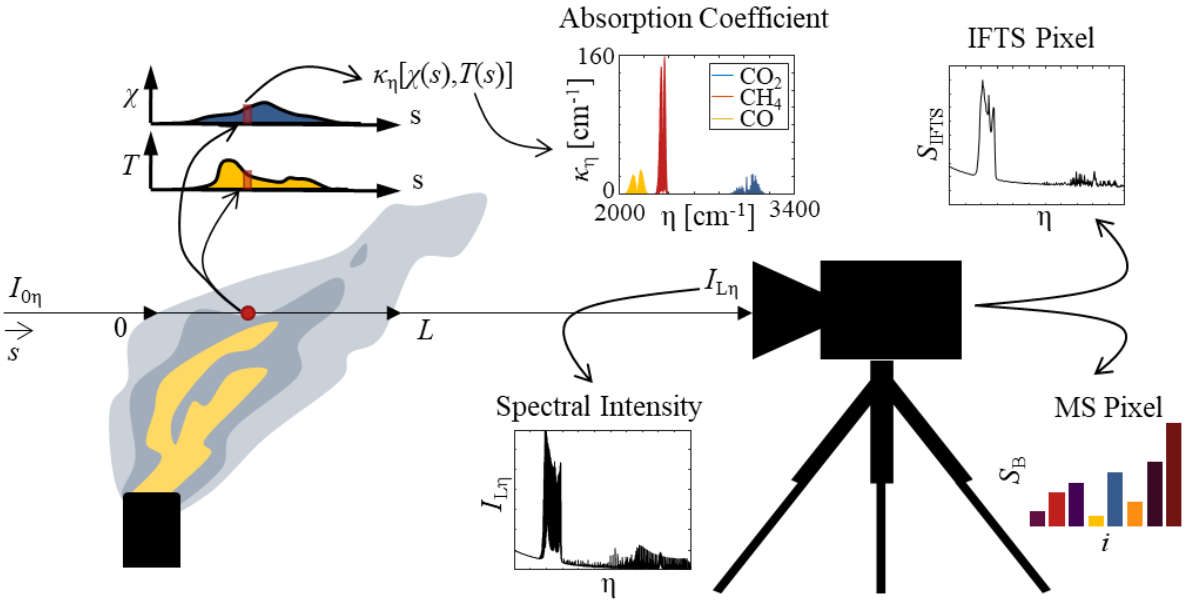

Figure 11 IR intensity along an optical path through the gas. The volume fractions and gas temperature distribution along the LOS affect the local absorption coefficient and the spectral intensity that reaches the camera lens. The participating gas absorbs part of the monochromatic intensity. In contrast, the gas emits radiation, and the gas reabsorbs the emitted radiation in the rest of the path. The spectral intensity that reaches the camera is further processed and downsampled.

However, it is hard to define an optically thin medium when the background is colder than the medium. In the case of a medium that is hotter than the background, the emission term and reabsorption term have a similar magnitude, even for a small amount of gas. This effect is exacerbated in a nonuniform temperature profile medium, as hotter gas emits with a lower absorption coefficient, and it is absorbed by colder gas with a more significant absorption coefficient on the spectral band center. On the other hand, if the medium is cold compared with the background emission source, the gas emission term can be neglected, which results in the Beer-Lambert law

$$I_{L\eta} = I_{0\eta} \exp\left(-\int_0^L \kappa_\eta(s)\, ds\right). \tag{3.13}$$

Although the RTE governs the spectral intensity that reaches the camera aperture, each camera model will transform the received intensity in the camera signal, represented in Figure 11. In the case of MS cameras, each signal corresponds to a broadband signal integrated over the transparent region of the corresponding filter. Therefore, spectral bands can be selected to target species of interest. IFTSs transform the incident spectrum into a large number of images through interferometry. The processes through which these cameras work is detailed in the next sections.

3.1.3 Broadband Multispectral Cameras

Broadband IR cameras are comparatively low-cost and have been used to identify gas leaks and quantify single-species mass flow for many years [51]. Broadband cameras are generally used to measure one species at a time at a known temperature [52,53]. In principle, broadband images can be used to determine the concentration of multiple species by comparing spectrally-filtered images, each of which corresponds to a spectral band of the species of interest. Multispectral (MS) cameras use multiple filters to limit the spectral range of the camera to fit spectral areas of interest, i.e. the spectral bands with stronger influence by the species of interest absorption. In an ideal scenario, each species emits in a distinct spectral band so that the broadband signal will change independently with the concentration or temperature of the corresponding gas.

The concentration estimation on each camera pixel needs at least one independent signal for each target species. Nevertheless, the pixel brightness depends on the species concentration and gas temperature. An additional independent signal is needed to quantify the temperature. A well-mixed

plume needs at least n+1 independent signals where n is the number of species. If the species are at different temperatures, 2n independent signals are required.

Optical filters are used to isolate spectral bands and generate distinct broadband signals. Filters are classified as either cold filters or warm filters. Cold filters are mounted with the camera sensor, shown in Figure 12 (a), which is cooled to improve the signal-to-noise ratio. In the case of cold filters, the radiative emission from the filter can be neglected, and the gas effect in the signal is stronger than the noise. However, as it is mounted with the sensor, it is built into the camera and, therefore, cannot be changed. Although experimental multispectral cameras use multiple filters built in the sensor house, cold filters are typically linked to single signal IR cameras [54].

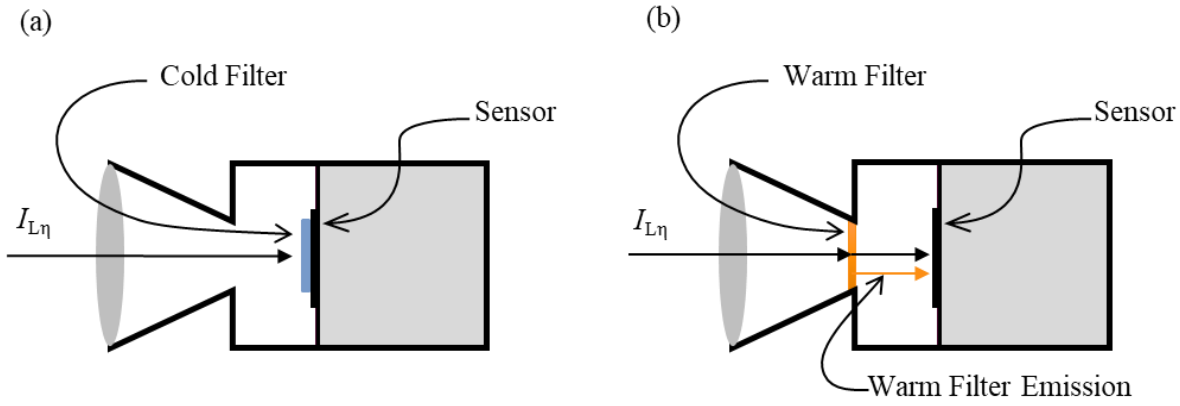

Figure 12 Cold and warm filter montage scheme. The cold filter is placed with the cryogenically cooled sensor, and the filter radiative emission can be neglected. Warm filters are placed between the lens and sensor at ambient temperature, so radiative emission from the filter may be significant.

In contrast, the warm filter is mounted in the camera's optics, as shown in Figure 12 (b), and can be changed easily, sometimes automatically, using filter wheels. As the camera optics are at ambient temperature, the warm filter is not cooled, and therefore a significant amount of the radiation

measured by the sensor is due to radiative emission from the filter. The broadband camera signal, S_B, can be modelled as

$$S_B = \int_{\eta_1}^{\eta_2} f_\eta \tau_\eta I_{L\eta} d\eta + G\left(\tau_\eta, T_F\right), \tag{3.14}$$

where η_1 and η_2 are the camera's lower and higher wavenumber limit, respectively, τ_η is the filter transmissivity, and T_F is the filter temperature. The spectral intensity, $I_{L\eta}$, that reaches the detector can be obtained from Eq. (3.11) or Equations (3.12) or (3.13), depending on gas conditions. Naturally, the warm filter emission term G can be neglected in cryogenic temperatures ($T_F \leq 80$ K) of a cold filter. The sensor spectral sensitivity, f_η, is the normalized capacity of the sensor to convert a photon into an electron as a function of wavenumber. The spectral sensitivity of an indium antimonide (InSb) sensor (used in a FLIR MWIR camera) is plotted in Figure 13.

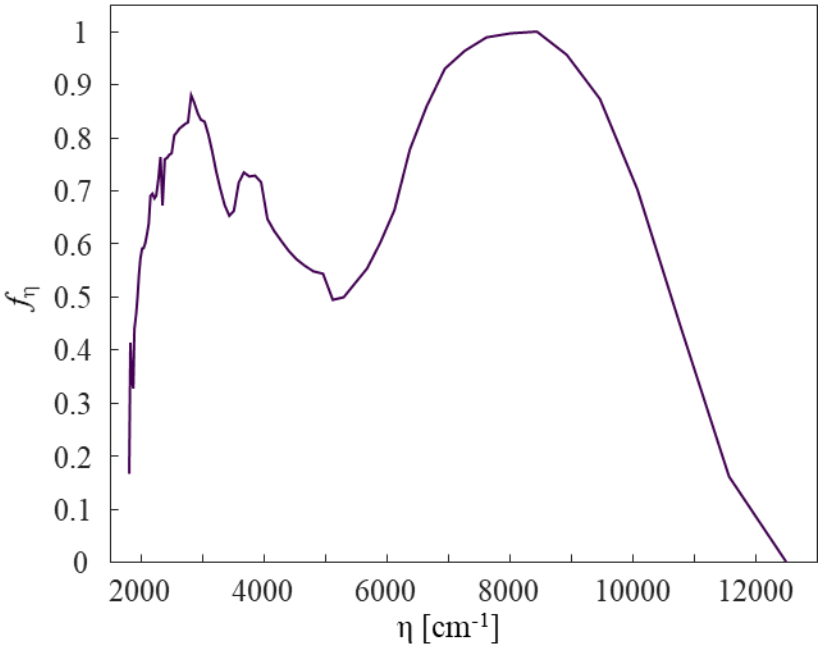

Figure 13 Broadband FLIR InSb sensor normalized spectral response curve from [55].

Filters with different transmissivity profiles can be chosen to highlight specific vibrational-rotational bands of gases. The measurement of three gases concentrations is necessary to obtain the flare CE (four if the H_2O concentration is inferred). At least three broadband IR signals are needed to estimate the CE, while most commercial cameras generate only one broadband signal. One option is to use a camera equipped with a filter wheel. The filter is changed in each frame, generating images with a slight temporal difference but with the same field of view. The Telops MS-IR MW is a cooled MS infrared camera with an InSb sensor to a spectral response in the MWIR (3.0 – 4.9 μm), with a spatial resolution of 640×512 pixels that allows the use of eight warm filters in the filter wheel, shown in Figure 14.

Figure 14 Telops MS-IR series. The camera uses an motorized filter wheel with eight spots, the filter position changes synchronized with the camera framerate generating signals with distinct spectral ranges almost simultaneously [56].

Infrared cameras are primarily used to measure temperature, and, therefore, they are usually characterized by their noise equivalent temperature difference (NETD). The characterization compares the sensor's electronic noise standard deviation to a blackbody temperature difference. Mid-wavelength cameras use semiconductor sensors, and the semiconductor bandgap energy corresponds to the camera's higher wavelength limit; as the power needed to jump this gap is relatively low in order to

detect low energy photons, electrons can also jump this gap by thermal excitation, causing the noise. Usually, photon detectors over the mid and long-wavelength infrared are cryogenically cooled to reduce noise [57]. To use the NETD reported by the camera manufacturer in the camera model given by Eq. (3.14), the NETD needs to be transformed back to the signal noise standard deviation by

$$\sigma_{\mathrm{SB}} = \int_{\eta_1}^{\eta_2} I_{\mathrm{b}\eta}\left(T_{\mathrm{REF}} + \mathrm{NETD}\right)d\eta - \int_{\eta_1}^{\eta_2} I_{\mathrm{b}\eta}\left(T_{\mathrm{REF}}\right)d\eta \tag{3.15}$$

In the case of mixtures of participating gases, the convolution of spectral lines makes it difficult to distinguish the presence of multiple gases having a partially-overlapping absorption spectra. Moreover, the absorption coefficient is dependent on the temperature, allowing more than one combination of gas concentrations and temperatures generate the same broadband signal set. Accordingly, the filter set needs to be carefully chosen to create an independent signal for each parameter of interest and, at the same time, maximize the signal sensitivity to a change in these parameters. An MS camera filter selection technique based on the minimization of CE variance given a measurement noise will be presented in Chapter 4. Alternatively, the number of signals can be increased with a higher spectral resolution camera, and several signals can be used to infer the parameters of interest.

3.1.4 Imaging Fourier Transform Spectrometer

Imaging spectrometers combine spectrally resolved data with two-dimensional spatial data, generating a 3D "hypercube." An IFTS uses a Michelson interferometer to create interference patterns in two-dimensional frames. The Michelson interferometer uses a beam splitter to divide the incoming light into two components of equal amplitude, each reflected by a pair of mirrors, as shown in Figure 15. One of the mirrors moves to change the difference between the optical path lengths travelled by the

light. The optical path difference (OPD) creates a phase difference between both light waves, generating constructive and destructive interference patterns when the waves are combined back by the beam splitter. The camera detector captures the result of the combined light. Carrying out this measurement over several OPDs results in a transformation from the wavenumber domain of the spectral intensity that reaches the equipment into the spatial domain. Therefore, the instrument's output is an estimation of the field autocorrelation, also known as an interferogram. An inverse Fourier transform (IFT) is applied to these interferograms to produce the 3D data cube consisting of 2D images with an additional spectral dimension, called a hyperspectral cube.

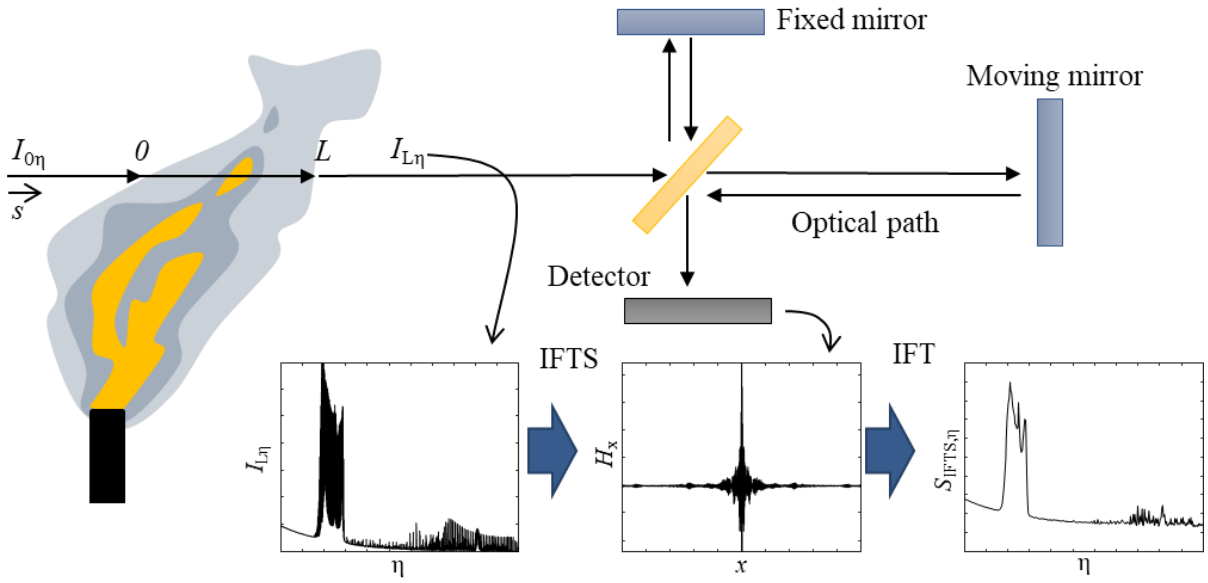

Figure 15 The IFTS transforms the spectral intensity incident upon the camera into a measurement spectrum. The incident spectral intensity reaches a bean splitter and half of the IR is directed to a fixed mirror and the remainder is directed to a mirror with adjustable distance. The IR is recombined in the bean splitter after traveling different optical paths. The difference of the optical path generates interference patterns recorded by the detector, the interferogram. The spectral intensity is obtained by numerically processing the interferogram using the inverse Fourier transform.

In an ideal spectrometer, the interferogram can be modelled as a function of OPD [58]

$$H_{\mathrm{x}}(x_{\mathrm{k}}) = \frac{1}{2}\int_0^{\infty} I_{\mathrm{L}\eta}[1+\cos(2\pi x_{\mathrm{k}}\eta)]d\eta \quad , \tag{3.16}$$

where x_{k} is the OPD. Applying the IFT on the interferogram generates the measured spectrum. However, the interferogram data is discrete and has a limited maximum optical path distance (MOPD); for these reasons, the measured spectral intensity differs from the spectral intensity that reaches the IFTS. The effects of finite MOPD are equivalent to truncating the higher frequencies on the Fourier transform, and the spectral intensity that reaches the equipment is apodized. The down-sampled data can be obtained by a convolution of the incident spectral intensity and the instrument line shape (ILS) function, Figure 16, with the same results as building the simulated truncated interferogram from Eq. (3.16) and applying the IFT

$$S_{\mathrm{IFTS},i} = \int_0^{\infty} I_{\mathrm{L}\eta} F(\eta_i - \eta)\, d\eta \tag{3.17}$$

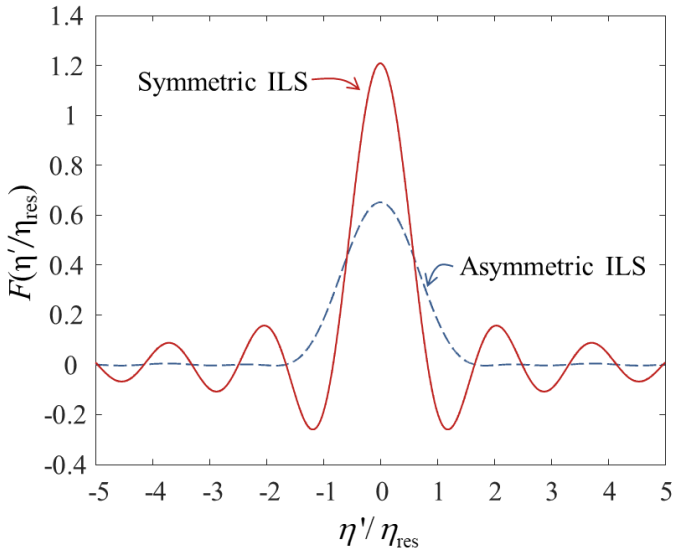

Figure 16 ILS of the IFTS transformed from symmetric and asymmetric boxcar function.

The instrument line shape can be modelled as a function of the MOPD, x_m, and the divergence contribution to the ILS is negligible because of each pixel's small instantaneous field of view (IFOV) [59]. In the ideal case of symmetric MOPD interferometer, the ILS is the FT of the boxcar function given by

$$F(\eta') = 2x_m \operatorname{sinc}(2\pi x_m \eta') \tag{3.18}$$

where sinc(x) = sin(x)/x. The MOPD is related to the spectral resolution, η_{res}, according to

$$x_m = \frac{1.20671}{2 \times \eta_{res}} \tag{3.19}$$

In the case of asymmetrical MOPD as the one used on Telops mid-wavelength IFTS for the spectral resolution of 0.25cm^{-1}, the MOPDs are 0.9 and 2.4 cm because of geometric limitations. The corresponding ILS is given by [59]

$$F_{asym}(\eta', x_m) = \frac{2x_m[4(1-2a)x_m^2\eta'^2 - 1]}{(1+2a)(4x_m^2\eta'^2 - 1)} \operatorname{sinc}(2\pi x_m \eta'), \tag{3.20}$$

where a is 0.428752.

Although the camera coupled to the interferometer has a high frame rate, the time required to measure a single data cube is approximately the sum of the time required to record an image multiplied by the number of discrete OPDs. For instance, the time to capture 2370 images needed for a spectral resolution of 4 cm^{-1} and integration time of 350 µs is around 12.5 s. During this time, a turbulent feature may traverse through several pixels in the images, and in the pixel's point of view, the gas state change while the interferogram is being built. Turbulent fluctuations that occur as the mirror transits through its OPD may cause scene change artifacts (SCAs) in the recovered intensity spectrum [60,61]. The mitigation of the SCAs can be done while acquiring the data by reducing the time required to record

each frame by decreasing the spatial resolution and reducing the total hyperspectral cube acquisition time using a low spectral resolution. [62]. The impact of SCAs can be reduced by taking the median of many interferograms in the postprocessing phase.

3.2 Combustion Efficiency using Quantitative Optical Gas Imaging

Modelling the camera signal is straightforward if the gas state, concentration, pressure, and temperature are known. However, inferring the mass flows of the species of interest using the camera data is more challenging. First, a control surface is defined that transects the plume and is aligned perpendicular to the camera image represented in Figure 17. This control surface is used to estimate the mass flow rates of carbon in the form of the species needed to compute the CE. The mass flow rate of carbon in the form of the i^{th} species can be approximated by combining the species column density with the apparent gas velocity normal to the control surface by

$$\dot{m}_{\mathrm{C},i} = \frac{M_{\mathrm{C}}}{M_i}\dot{m}_i = \frac{M_{\mathrm{C}}}{M_i}\int_0^{\Theta} \rho_i(\theta)\bar{u}(\theta)\,\mathrm{d}\theta, \tag{3.21}$$

where ρ_i is the column density of the i^{th} species in the pixel located at parametric distance θ along the control surface, $\bar{u}$ is the intensity weighted normal velocity, and M_{C} and M_i are the carbon molar mass and i^{th} species molar mass, respectively.

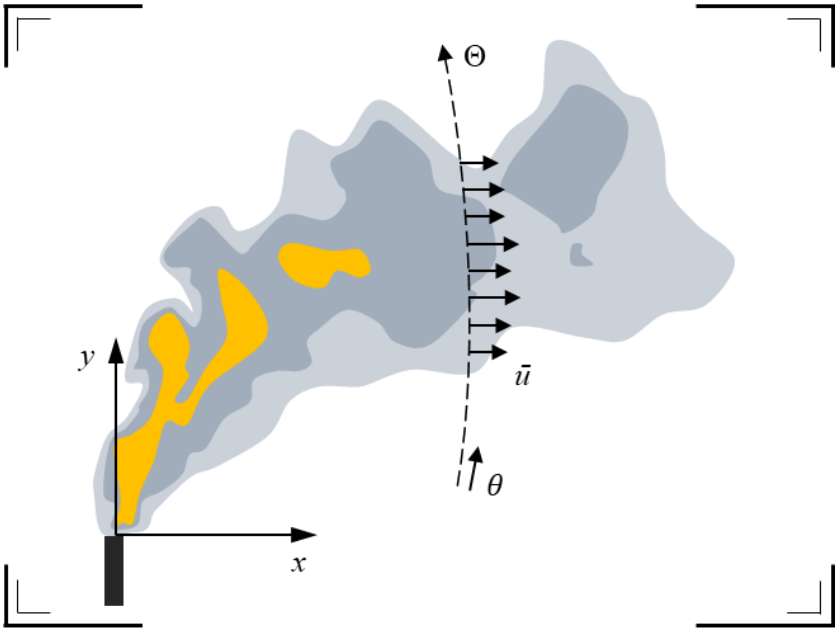

Figure 17 Representation of the camera image containing the flare. The control surface to estimate the mass flow of carbon on the flare plume appears as a line as it is oriented entering the picture.

The pixel column density of each pixel is the sum of all gas molecules along the LOS, expressed in units of mass. This quantity is derived from the ideal gas law

$$\rho_i = \frac{M_i}{A} N_i = \frac{M_i}{A} \int_0^L \frac{\chi_i(s)\, p}{k_B T(s)} ds \tag{3.22}$$

where A is Avogadro's number, N_i is the column number density, χ is the species volume fraction along the LOS, T is the temperature along the LOS, and k_B is Boltzmann's constant. Substituting Eq. (3.21) in Eq. (2.8), the CE can be written as

$$CE = \frac{\frac{M_C}{M_{CO2}}\int_0^{\Theta}\rho_{CO2}(\theta)\bar{u}(\theta)\mathrm{d}\theta}{\frac{M_C}{M_{CO2}}\int_0^{\theta}\rho_{CO2}(\theta)\bar{u}(\theta)\mathrm{d}\theta+\frac{M_C}{M_{CO}}\int_0^{\theta}\rho_{CO}(\theta)\bar{u}(\theta)\mathrm{d}\theta+\frac{M_C}{M_{CH4}}\int_0^{\theta}\rho_{CH4}(\theta)\bar{u}(\theta)\mathrm{d}\theta}, \quad (3.23)$$

and with further simplifications using Eq. (3.22)

$$CE = \frac{\int_0^{\Theta}N_{CO2}(\theta)\bar{u}(\theta)\mathrm{d}\theta}{\int_0^{\Theta}N_{CO2}(\theta)\bar{u}(\theta)\mathrm{d}\theta+\int_0^{\Theta}N_{CO}(\theta)\bar{u}(\theta)\mathrm{d}\theta+\int_0^{\Theta}N_{CH4}(\theta)\bar{u}(\theta)\mathrm{d}\theta}. \quad (3.24)$$

The control surface corresponds to a row of pixels in the 2D image, so Eq. (3.24) can be written in discrete form by summing over the pixels that form the control surface

$$CE = \frac{\sum_k N_{CO2,k}\bar{u}_k}{\sum_k N_{CO2,k}\bar{u}_k+\sum_k N_{CO,k}\bar{u}_k+\sum_k N_{CH4,k}\bar{u}_k}. \quad (3.25)$$

Therefore, the column number density and the intensity weighted normal velocity are the parameters that must be inferred from the camera data to estimate the CE.

3.2.1 Column Number Density Estimation

According to Eq. (3.22), the column number density calculation requires the species volume fraction and temperature distribution along the LOS. In principle, the column number density can be obtained by fitting volume fractions and temperature to minimize the difference between the camera measurement and the model results. However, the problem is ill-posed due to spatial (LOS) and spectral dimensions convolutions. Consequently, several candidate temperatures and volume fraction distributions along the LOS can produce identical camera data corresponding to unique species column densities. Specifically, in the absence of emission or emission with negligible reabsorption, Eq. (3.11) becomes a Fredholm integral equation of the first-kind (IFK), which has an infinite set of solutions.

The ill-posedness is exacerbated by the spectral convolution in Eqs. (3.17) for the IFTS, especially (3.14) for the multispectral camera. Since the species of interest contain overlapping spectral absorption bands, multiple volume fraction combinations from other species can generate the same broadband signal.

The spatial ill-posedness needs to be addressed by parameterizing the volume fraction and temperature distributions along each LOS. While it is theoretically possible to estimate the temperature profile along the LOS, as each absorption line has a unique sensitivity to temperature, the impact of volume fraction on spectral intensity is almost linear due to the weak self-broadening effect on molecules like CO_2, making it impossible to estimate the volume fraction profile based on the emitted intensity alone [49]. Accordingly, the temperature and species concentration distributions are typically assumed to be uniform along the LOS [43,63–65]. While, in most cases, the temperature and species volume fractions are far from uniform, this simplification introduces manageable model error in instances where the plume is colder than the background. As already noted, in this scenario, the spectral intensity amounts to a Fredholm IFK; the actual species distribution along the line-of-sight is immaterial to the transmittance, provided the overall column density is the same.

On the other hand, in cases where the background is colder than the gas, the alignment of the temperature and species concentration distributions becomes critical in order to obtain the correct column densities. Simulated IFTS measurements from a hot free turbulent jet showed that modelling the species volume fractions and temperature distributions as Gaussian along each LOS provided more accurate mass flows than assuming uniform distributions [66]. For this reason, the distributions along the LOS are parametrized by

$$\chi_i(s) = \chi_{i,\max} \exp\left(-\frac{s^2}{2\sigma^2}\right), \quad T(s) = \left(T_{\max} - T_\infty\right)\exp\left(-\frac{s^2}{2\sigma^2}\right) + T_\infty \,, \tag{3.26}$$

where $\chi_{i,\max}$ is the peak volume fraction, σ is the characteristic plume width, $T_{\max}$ is the plume peak temperature, and T_∞ is the ambient temperature.

With the parametrized LOS distribution, the model gas state for CH_4 combustion can be described by the vector $\mathbf{x} = [\chi_{CH4,max}, \chi_{CO2,max}, \chi_{CO,max}, \chi_{H2O,max}, T_{max}]^T$. The width parameter σ may also be included as an unknown or estimated directly from the visible plume width. It is important to note that even though H_2O is not a species of interest, it is a combustion product that emits radiation in the same spectral region; therefore, it needs to be estimated to explain the camera signal. The next step is to find the gas state that best explains the measurement data; the maximum likelihood estimate (MLE) is found, as represented in Figure 18, from weighted nonlinear least-squares regression,

$$\hat{\mathbf{x}} = \arg\min_{\mathbf{x}} \left\{ \left[\mathbf{S}(\mathbf{x}) - \mathbf{S}^{\text{meas}}\right]^{\mathrm{T}} \boldsymbol{\Gamma}_S^{-1} \left[\mathbf{S}(\mathbf{x}) - \mathbf{S}^{\text{meas}}\right] \right\}, \tag{3.27}$$

where $\mathbf{S}^{\text{meas}}$ is a vector containing the measured spectrally-resolved data from a pixel, $\boldsymbol{\Gamma}_S$ is the covariance matrix, and $\mathbf{S}(\mathbf{x})$ is the model data from the pixel given by Eq. (3.14) or (3.17) depending on the chosen camera. For the IFTS, the elements of $\mathbf{S}$ correspond to a unique wavelength signal, while for the multispectral camera, each element corresponds to the signal generated using each filter. For both cameras, measurement noise is often modelled as independent, in which case the covariance matrix is simply a diagonal with elements corresponding to the camera noise variance.

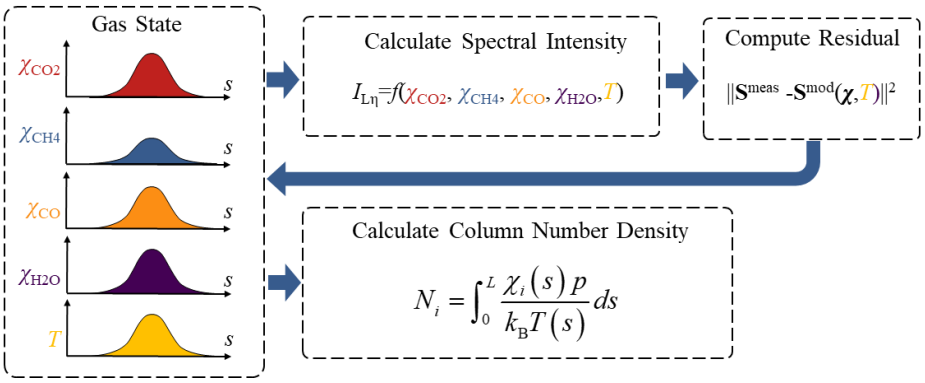

Figure 18 Procedure for inferring column number density for a pixel. The gas state parameters are changed to reduce the residuals between measured and modelled pixel signal; after the residual is minimized, the column densities of each species are computed.

This procedure is not expected to recover the "exact" set of parameters because the measurements are corrupted by both measurement noise and model error. Specifically, it can be written

$$\mathbf{S}^{meas} = \mathbf{S}(\mathbf{x}) + \delta\mathbf{S}^{noise} + \delta\mathbf{S}^{model} \tag{3.28}$$

where $\delta\mathbf{S}^{noise} \sim p(0,\boldsymbol{\Gamma}_S)$ and $\delta\mathbf{S}^{model}$ are errors arising from the simplifications made to derive the model, e.g. parameterizing the species and temperature distributions along each LOS with Gaussian profiles. Even though these errors may be small, they may be amplified during data inversion due to the ill-posedness of the inverse problem into large errors in the recovered parameters.

In principle, the ill-posedness introduced by the spectral convolution can be mitigated by increasing the resolution of the IFTS or carefully selecting independent optical filters for the multispectral camera. Nevertheless, increasing the resolution of the IFTS increases the time needed to acquire the data and consequently increases the noise from SCAs created by turbulence. On multispectral cameras, selecting narrow spectral bands to isolate features with higher sensitivity to a change of one parameter has a similar effect; the signal decreases while the primary noise source is

constant. Alternatively, this problem can be mitigated by adding prior information to the system, like possible reactions and mixing pathways. Adding combustion reaction information to minimize the spectral convolution ill-posedness will be investigated in Chapter 6.

3.2.2 Normal Velocity Estimation

The connection between the three-dimensional velocity field in the plume and the apparent motion of the plume projected into the image plane is not necessarily obvious. However, calculating the mass fluxes only requires the velocity components normal to the control surface, as shown in Figure 17; the velocity components going into and out of the image plane do not contribute to the flow estimation, assuming that the full plume crosses the control surface. Although the image needs to be somewhat perpendicular to the flow (e.g., as determined by wind direction), this does not need to be enforced precisely. If the measurement deviates from perpendicular to the plume movement by an angle φ, the velocity component normal to the control surface is reduced by cos φ, while the plume thickness and column density increase by 1/cos φ [67].

The flow velocity is inferred by analyzing the apparent motion in pixel brightness between successive images, as represented in Figure 19. The apparent velocity of the brightness patterns can be directly associated with the turbulence features movement in the flow. The broadband images are analyzed using the Horn-Schunck optical flow algorithm [68]. The optical flow algorithms assume that the brightness is conserved, $dS/dt=0$. Accordingly, the temporal changes in the pixel brightness, S, between successive images are credited only to advection, and the gradient constraint equation is given by

$$\frac{DS}{Dt} = \frac{\partial S}{\partial x}\frac{\partial x}{\partial t} + \frac{\partial S}{\partial y}\frac{\partial y}{\partial t} + \frac{\partial S}{\partial t} = 0\,, \tag{3.29}$$

assuming that $S_x = \partial S/\partial x$, $S_y = \partial S/\partial y$, $S_t = \partial S_l/\partial t$ and u and v are the x and y velocity components. Equation (3.29) can be written as

$$S_x u + S_y v = -S_t . \tag{3.30}$$

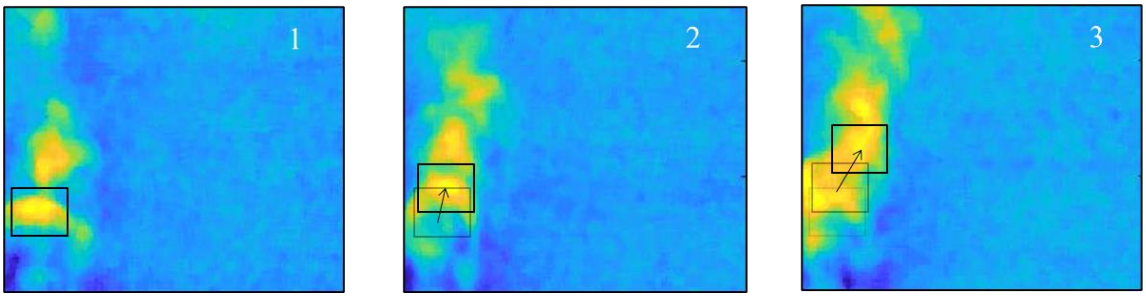

Figure 19 Schematic of the optical flow of a turbulent feature in a jet flow.

The derivatives are estimated using centred first-order finite-difference for pixels vertices and from two successive image frames. For images, the equation can be written in matrix form with derivatives stored in vectors $\mathbf{s}_x$, $\mathbf{s}_y$, and $\mathbf{s}_z$.

$$\left[\mathbf{S}_x, \mathbf{S}_y\right]\begin{bmatrix}\mathbf{u}\\ \mathbf{v}\end{bmatrix} = \mathbf{AV} = -\mathbf{s}_t , \tag{3.31}$$

where $\mathbf{S}_x = \mathrm{diag}(\mathbf{s}_x)$ and $\mathbf{S}_y = \mathrm{diag}(\mathbf{s}_y)$ and $\mathbf{V}$ contains the unknown velocities. However, for a flow field consisting of N_v vertices, Eq. (3.31) produces a system of N_v equations and $2N_v$ unknown velocity components, so the problem is underdetermined and additional information must be introduced to solve both velocity components. The set of equations is closed using a 2nd order Tikhonov smoothness prior at each vertex resulting in an overdetermined matrix equation given by

$$\begin{bmatrix} \mathbf{A} \\ \lambda \mathbf{L}_{uv} \end{bmatrix} \mathbf{V} = \begin{bmatrix} \mathbf{S}_x & \mathbf{S}_y \\ \lambda \mathbf{L} & 0 \\ 0 & \lambda \mathbf{L} \end{bmatrix} \begin{bmatrix} \mathbf{u} \\ \mathbf{v} \end{bmatrix} = \begin{bmatrix} -\mathbf{s}_t \\ 0 \\ 0 \end{bmatrix}, \tag{3.32}$$

where matrix **L** is found by vertex-wise construction. Each row of **L** corresponding to a vertex is constructed from nine Laplacian coefficients, as shown in Figure 20. In the case of a boundary vertex, the row is renormalized, resulting in a Neumann boundary condition, $\partial u/\partial x = 0$ or $\partial v/\partial y = 0$. Finally, the **V** is solved using least-squares minimization.

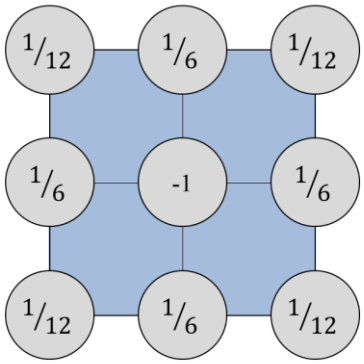

Figure 20 Laplacian coefficients for vertices needed to estimate the velocity at the central vertex. The scheme shows the weight of each neighbour in the inferred velocity uniformity. The weight of vertices further away is considered zero.

3.3 Quantitative Optical Gas Imaging Development

While OGI was originally deployed to detect leaks of methane and other gases, a further natural step is using OGI to quantify these leaks. While this technique is widely used to measure emissions of methane and other single-component gases at room temperature, to the best of the author's knowledge, there is

currently only one commercial equipment to quantify flare CE using OGI [69,70], and there is very little information about the principles that underlie this approach. (Tests results with the available information on the product patent are available in Appendix).

A few studies focused on quantifying one species using OGI are worth mentioning. Sandsten et al. [71–73] used a MWIR camera for real-time detection and later quantification of a gas leak. The authors employed a Cassegrainian telescope to record the scene through two different filters simultaneously: one for reference and one that features the species of interest. The reference signal was generated by filtering the image through a gas correlation cell that contains a known concentration of the target species [74–76]. The concentration and distribution of the target species were then inferred by differential analysis of images captured with and without filtering.

In terms of quantifying gas mixtures, most previous studies are based on hyperspectral imaging. Gross et al. [64] use an MWIR IFTS to quantify the concentrations of industrial smokestack emissions. The data was used to estimate each pixel's gas temperature and species column densities at the stack exit. The LOS width was estimated from the smokestack diameter, and the concentration and temperature were assumed to be uniform through the LOS. The values calculated by this technique were consistent with CO_2 and sulphur dioxide (SO_2) concentrations inferred from probes. The transient effects were mitigated by averaging 20 minutes of data. With the same data, Harley and Gross [77] used sequential images from the interferogram to estimate the velocity in the center of the steam, which was combined with the column densities to obtain species mass flows. Harley et al. [78] use an IFTS in a turbulent $CH_4/H_2/N_2$ flame. The authors discussed the effect of flame's turbulent fluctuations in the interferograms and used the averaged data of 512 interferograms to mitigate SCAs.

Watremez et al. [79] used three IFTS in the long-wave IR region to reconstruct a 3D methane flow. The data was acquired from measurements of 36 CH_4 jets with flow varying from 1g/s to 50g/s. The mass flow was estimated by assuming that the flow velocity was identical to the measured wind velocity. The authors captured the background image recording the scene without gas and used Algebraic Reconstruction Technic (ART) to reconstruct the concentration distribution.

Gålfalk et al. [43] use an MWIR IFTS to quantify CH_4 and nitrous oxide (N_2O) emissions simultaneously with various backgrounds. In the authors' approach, the air humidity and the sky's reflection in the background were considered. The IFTS-simulated signal was pre-computed for different mixture concentrations to accelerate the computations. They show that concentration accuracy depends on the temperature difference between the gases and background. It is necessary to have a difference of at least 1 K to obtain robust results.

Grauer et al. [66] simulated an IFTS using a large eddy simulation (LES) of a CH_4 free jet. The concentration and temperature distribution along the LOS were modelled as a Gaussian profile instead of the uniform profile assumed in previous works [43,49,73]. This approach reduces the column density estimation errors, 26.5% for uniform and 11.7% using Gaussian profile. The flow velocity was obtained with image correlation velocimetry (ICV) using the software LaVision. The mass flow of CH_4 estimation had an error of 5.4%.

The number of studies using IFTS to measure the flare CE is limited. Allen and Torres [41] conducted field tests to measure flare emissions as part of a Texas Commission on Environmental Quality (TCEQ) study, including CE measurement. The study involved an IFTS blind test described in Section 2.3.2.

3.4 Conclusions

QOGI allows the measurement of the species column density and apparent velocity in each image's pixel and, consequently, the species mass flows. Fence-line CE estimates can be done using MS MWIR cameras or MWIR IFTS. The CE measurement is done by estimating the column number densities of the species containing carbon in a control surface cutting the combustion plume, a line crossing the plume in the image, then combining this data with the apparent gas velocity in the same pixels. The gas velocity is estimated using the sequence of images brightness patterns changes through an optical flow algorithm.

The radiative spectral intensity that reaches the camera can be modelled by knowing the gas state along the LOS. First, the gas state is used to obtain the absorption coefficient along the LOS; then, the RTE is used to calculate the spectral intensity. The spectral intensity needs to be further processed to include the equipment effects on the measurement data. However, the combination of spatial convolution on the RTE and spectral convolution on the camera models makes inferring the column density from the camera data an ill-posed problem. The spatial ill-posedness is solved by parametrizing the volume fraction and temperature distribution along the LOS as a Gaussian profile. The spectral ill-posedness can be addressed by using high spectral resolution data from an IFTS to resolve each species' several spectral lines. Alternatively, optimal spectral bands can be selected to maximize the information needed to infer CE using an MS camera.

Chapter 4

Optimal Filter Selection for Quantitative Gas Mixture Imaging

This chapter presents a general technique to select optimal filters for an MS MWIR camera to quantify multiple components of a gas mixture. Filter sets are ranked in terms of the ratio of quantity-of-interest variance to noise variance, which is minimized by the optimal filter set. This criterion's suitability is demonstrated using a numerical experiment in which the CE of a gas flare is estimated from MWIR images of the flare plume. Synthetic spectral intensity data are generated using the spatially-resolved thermochemical state of a simulated flare-in-crosswind. Then the multispectral images for commercially-available filter sets are computed, and the concentration of key species (CH_4 and CO_2) and temperature along LOS that correspond to sampled pixels are estimated. These distributions are converted to an estimate of the CE, and the accuracy of this estimate is compared for a filter set to the selection criterion. This procedure verifies that the selection criterion is a good predictor of CE accuracy. While the focus of this work is on estimating flare combustion efficiency, this technique can be applied to any number of quantitative multispectral gas imaging scenarios. The results and procedure presented in this chapter are presented in the published article [80][7]

[7] This paper is coauthored by Johannes Emmert who helped in the creation of the concept and methodology; Samuel J. Grauer who helped in the creation of the concept; Jeremy Thornock who provided the LES data; and Kyle J. Daun who helped in the creation of the concept, methodology, supervision, review, editing, project administration, supervision, and funding acquisition.

4.1 Introduction

IFTSs offer an excellent spectral resolution, but their high cost and low temporal resolution limit their range of applicability, particularly in scenarios that feature turbulent flows [58,60]. MS cameras are far less expensive than IFTSs and offer fast imaging that can resolve key structures in a turbulent flow. On the other hand, MS cameras have significantly lower spectral resolution than IFTSs, which decreases sensitivity to multiple species in a mixture. Therefore, spectral bands must be chosen with care to obtain accurate measurements of multiple species with an MS camera. Band selection is typically conducted by a heuristic search for bandpass filters that maximize the sensitivity of images to the species-of-interest; e.g., filters may be aligned with dominant ro-vibrational bands. Filter widths also pose a trade-off between spectral selectivity and the signal-to-noise ratio (SNR), which has been exploited for filter selection [57]. However, this procedure ignores the interaction of multiple species with overlapping bands as well as the influence of other parameters like the ambient humidity and temperature.

This chapter outlines a general method to optimize the filter set for an MWIR MS camera using a statistical framework. The approach minimizes the expected quantity-of-interest variance relative to the measurement noise. The metric is derived from the data evaluation method, which involves the nonlinear fitting of the RTE. The uncertainty associated with camera noise is propagated through the evaluation procedure to obtain posterior uncertainties of the quantity-of-interest. The error propagation is linear under the assumption of a large SNR resulting in an efficient estimation of the selection metric. While the framework can be used to evaluate any theoretical filter, practical filter selection is subject to engineering constraints, such as the need to balance the filter wheel and commercial availability. The result is a combinatorial optimization problem that targets discrete combinations of existing filters as opposed to continuous real-valued parameters that specify filter transmittance functions. Nevertheless,

there are hundreds of millions of candidate filter sets, and a sophisticated, numerically-efficient selection procedure is required.

4.2 Vectorized Broadband Camera Model

A multispectral high-speed MWIR camera, MS M100k (Telops, Inc.), is chosen for the CE experiment. The camera has a spatial resolution of 640×512 pixels, a spectral range of 2041 to 3333 cm^{-1} (3 to 4.9 μm), a framerate of 115 Hz, and a filter wheel that holds eight filters. The filter wheel rotation is synchronized with the framerate so that each sequence of eight images corresponds to the full set of filters. The camera and filters are calibrated to compensate for the filter emission and transmission losses. The camera signal (pixel brightness, S_B) for the i^{th} filter is modelled using Eq. (3.14) , assuming a spectrally-uniform camera response function, and $I_{L\eta}$ is the spectral radiative intensity reaching the pixel, given by Eq. (3.11). By discretizing the integral in Eq. (3.14) over a sufficiently fine set of wavenumbers ($\Delta\eta = 0.05\ cm^{-1}$), the pixel signal can be written as the scalar product of filter transmissivity and the spectral intensity vector,

$$S_i = \sum_{j=1}^{n} f_{\eta j,i} I_{L\eta,j} \Delta\eta = \mathbf{f}_i \cdot \mathcal{J}_L \quad , \tag{4.1}$$

where $f_{\eta j,i}$ is the filter transmissivity at the j^{th} wavenumber, $I_{L\eta,j}$ is the spectral intensity at the j^{th} wavenumber. In the case of uniform discretization, the filter transmissivity can be expressed by the vector $\mathbf{f}_i = [f_{\eta 1,i}; f_{\eta 2,i}; \ldots; f_{\eta n,i}]\Delta\eta$ and, likewise, $\mathcal{J}_L = [I_{L\eta,1}; I_{L\eta,2}; \ldots; I_{L\eta,n}]^T$. The signal corresponding to each filter in a pixel is organized into vector $\mathbf{S} \in \mathbb{R}^{1,m}$, where $m = 8$ is the number of filters. For the full vector **S**, Eq. (4.1) can be summarized as a matrix product,

$$\mathbf{S} = \mathbf{F}_{\text{filter}} \cdot \mathcal{J}_L \, , \tag{4.2}$$

where $\mathbf{F}_{\text{filter}} \in \mathbb{R}^{n,m}$ is the filter matrix, $\mathbf{F}_{\text{filter}} = [\mathbf{f}_1; \mathbf{f}_2; \ldots \mathbf{f}_m]$.

4.3 Inferring Flare Combustion Efficiency

In principle, the data vector of each pixel, **S**, can be used to infer the species column densities of CO_2 and CH_4, which can be used in Eq. (2.8) to evaluate the global CE or Eq. (2.9) to evaluate the local CE at a pixel. The concentration of the species-of-interest must be inferred simultaneously with the temperature distribution and H_2O concentration since these parameters also influence $I_{L\eta}$. Representing the gas state as a vector, $\mathbf{x} = [\chi_{CH4,max}, \chi_{CO2,max}, \chi_{H2O,max}, T_{max}]^T$, the MLE is found by weighted nonlinear least-squares regression, Eq. (3.27). The measurement error can be approximated as independent, in which case the $\mathbf{\Gamma_S}$ is a diagonal matrix where each element is the camera noise variance with the corresponding filter.

The "spatial ill-posedness" is addressed by parameterizing the concentration and temperature profiles along a LOS. Hence, in this work, the concentration and temperature profiles are parameterized using Eq. (3.26). In principle, the characteristic plume width could be included as an additional parameter to be inferred. However, to keep the problem dimension manageable, this value is treated as fixed and specified based on the observed plume thickness in the image. These profiles are substituted into Eqs. (3.11) and (3.14) to generate the modelled spectral intensity, $I_{L\eta}$, and modelled filter set signal, **S(x)**, where $\mathbf{x} = [\chi_{CH4,max}, \chi_{CO2,max}, \chi_{H2O,max}, T_{max}]^T$. The distribution of concentrations and temperature are found by minimizing the objective function in Eq. (3.27) using the trust-region reflective algorithm, with bound constraints of zero and unity placed on the peak volume fractions. Iteration is terminated under one of three conditions.

1. The magnitude of the gradient becomes lower than a defined threshold (i.e. the Karush–Kuhn–Tucker conditions [81] are approximately satisfied);

2. The change in the objective function between successive iterations falls below a threshold value (5×10^{-9}); or

3. The change in the elements of **x** fall below a threshold value (10^{-6}).

In principle, simultaneous filtered images obtained with a broadband camera can be used to quantify each species in a homogeneous mixture, provided there is at least one independent image for each species and that the gas temperature is known. Since many of the absorption bands of the species-of-interest partially overlap, it is crucial to identify filters that maximize the independence of these images to each species. The sensitivity of the camera signal to temperature will also depend on each species' concentration because of the band weighting of the blackbody distribution, i.e., filters at lower wavenumbers will be more sensitive to temperature differences. In addition, the uncertainty of each gas column density estimation will have a different weight in the CE estimation. These effects may be taken into account through the error propagation technique described in the next section.

4.4 Filter Selection Procedure

A realistic set of sample LOS was calculated using a CFD simulation of a flare to incorporate the effects of different concentrations and temperature distributions along the LOS.

4.4.1 Synthetic Spectral Intensity

The CFD simulates a flare on top of a 102 mm inner diameter stack, representing those used for upstream oil and gas processing. Methane is injected at 298 K and 21.6 g/s into the air at the same temperature and has a crosswind velocity of 3.056 m/s. These conditions correspond to a Reynolds number of ~24,000 and a fire Froude number of 0.027, indicating turbulent flow at the fuel output and a buoyancy-controlled flame [82]. The temperature and species concentration fields are simulated using

the Arches (CFD-LES) component of the Uintah Computational Framework Software Suite [83–85], which includes a discrete ordinates solver to account for radiant losses from the hot gas and particulate. The total gas properties are inferred from the Sarofim and Hottel gas emittance charts [86]. The simulation uses the simplified oxidation mechanism proposed by Westbrook and Dryer [87], and the LES turbulence sigma model. The spatial domain is 3.5 m × 3 m × 5 m, encompassing the combustion zone and the plume, which was discretized into 1.3×10^7 elements of 5 cm × 5 cm × 5 cm. Data were collected from 30 frames with timesteps of 0.1 s. More information about the simulation can be found in Ref. [88]. Figure 21 shows a plot of the instantaneous "ground truth" pixel combustion efficiency, based on Eq. (2.9), at one instant in the CFD simulation via

$$\eta_{\text{pixel}k} \approx \frac{N_{\text{CO2},k}}{N_{\text{CO2},k} + N_{\text{CH4},k}}. \tag{4.3}$$

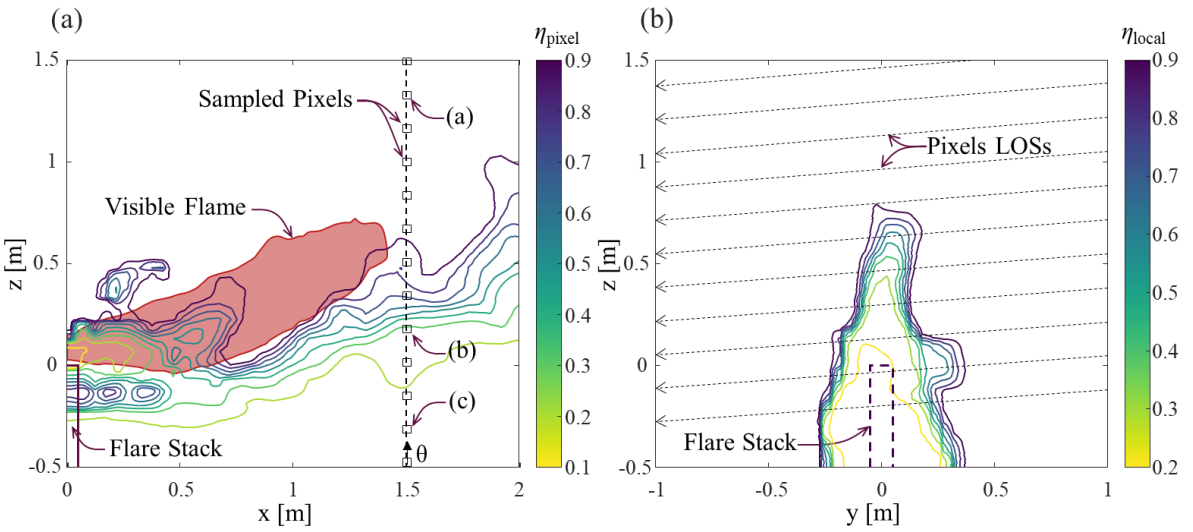

Figure 21 CFD simulation of local combustion efficiency of the flare in a crosswind (timestep 30): (a) lateral view, squares denote the 13 sample pixels; (b) control surface local CE, lines denote the sampled pixels LOS. Note the low CE region below the flare caused by the aerodynamic fuel stripping mechanism. Results for individual pixels (a), (b), and (c) are shown in Figure 23.

The spectral intensities corresponding to each pixel are obtained from the concentration and temperature distribution along the corresponding LOS. The LOS position vectors through the CFD domain were derived using a pinhole camera analogy derived from the camera's sensor size and the problem geometry [66,88]. The simulated camera was positioned 120 m from the flare stack with a height difference between the camera and the stack tip of 8.5 m. The synthetic camera image corresponds with a telescope magnification of 0.25 over the camera's standard field-of-view, 6.4°×5.1°.

In an actual CE calculation, the inferred concentration parameters would be combined with the velocity field inferred from optical flow, Section 3.2.2, to obtain a combustion efficiency via Eq. (3.25) . In this study, the focus is on the pixel combustion efficiency. The red line in Figure 21 marks the flame envelope, and the squares denote sample pixel locations used to identify the optimal filters and then assess their optimality. The LOS species concentrations and temperature were obtained from the 13 pixels over six different timesteps, for a total of 78 samples.

The LOS coordinates were used to get the species volume fractions and temperature from 50 discrete segments of the CFD results. The volume fractions and temperature were used to obtain each species' absorption coefficient to generate the mixture absorption coefficient using Eq. (3.8), as shown in Figure 22. The spectral line profiles were approximated using the Lorentz profile. The mixture absorption coefficient is the input of Eq. (3.11) to generate the synthetic spectral intensity that reaches the camera. Finally, the spectral intensity is down-sampled to the camera spectral resolution using Eq. (3.14) or Eq. (4.2), generating the synthetic MS camera data.

Each species absorption coefficient is precomputed and stored in lookup tables with spectral increments of 0.05 cm^{-1}, volume fraction increments of 0.05, and temperature increments of 1 K to

reduce the computation time. The absorption coefficient line strengths and line shape parameters are taken from HITRAN [47], assuming air broadening.

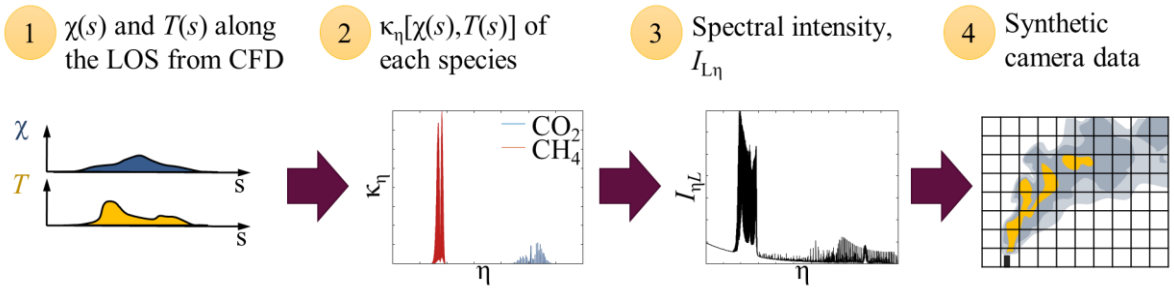

Figure 22 Simulation of synthetic camera data. 1) The volume fraction and temperature profile along the LOS is obtained from CFD results. 2) The absorption coefficient is computed for each point along the LOS using the local species volume fraction and gas temperature. 3) The spectral intensity is computed using the background spectral intensity, gas temperature, and absorption coefficient. 4) The computed spectral intensity is downsampled to the camera spectral resolution.

4.4.2 Ideal Case Parameters Estimation

Next, the parameters of Gaussian concentrations and temperature distributions were inferred from the fully resolved spectral intensity measurements for each sampled pixel. This represents the best-case scenario in which all the spectral information is available to infer the quantities-of-interest, and corresponds to a measurement made using an IFTS camera. The radiative emission from the pixels obtained from CFD parameters was stored in the vector $\mathcal{J}_L$, and the modelled radiative intensity, $\hat{\mathcal{J}}_L$, is generated from the Gaussian distribution, Eq. (3.26), with a discretization of 51 elements over a length of 200 cm with a characteristic plume width of 20 cm. The MLE,

$$\hat{\mathbf{x}} = \arg\min_{\mathbf{x}} \left\{ \left[\hat{\mathcal{J}}_{\mathrm{L}}(\mathbf{x}) - \mathcal{J}_{\mathrm{L}} \right]^{\mathrm{T}} \boldsymbol{\Gamma}_{\mathcal{J}}^{-1} \left[\hat{\mathcal{J}}_{\mathrm{L}}(\mathbf{x}) - \mathcal{J}_{\mathrm{L}} \right] \right\} \tag{4.4}$$

was then used to estimate the optimum result, $\hat{\mathbf{x}}$, where $\boldsymbol{\Gamma}_{\mathcal{J}}$ is the spectral intensity measurement noise covariance matrix. For each $\hat{\mathbf{x}}$ the model Jacobian, $\mathbf{J}_{\mathcal{J}}$, describing the sensitivity of spectral intensity on concentration and temperature values, was calculated for later use in the linear error propagation. Figure 23 compares the inferred Gaussian concentrations for CH_4 and CO_2 with instantaneous values for the sample pixels in Figure 21. The pixels' LOS transect unique features in the combustion products, including: (a) ambient concentrations of CH_4 and CO_2, (b) a non-Gaussian distribution, and (c) a CH_4-rich distribution in the fuel-stripping region. Noise substantially influences the estimate at pixel (a), resulting in significant uncertainty in the pixel CE, and model errors corrupt the estimates at pixel (b). The actual plume thickness is thinner than the plume thickness parameter in the model for pixel (c). Although the flare conditions generate a kidney shape combustion products plume, the unburned fuel tends to form a narrow structure as it is driven by the low-pressure region caused by the stack wake.

While, in principle, filter selection can be envisioned as a continuous optimization problem, in practice, only a finite set of commercially-available bandpass, long/shortwave-pass, and broad-bandpass filters over the wavelengths of interest are available, so choosing the best filter combination amounts to solving a combinatorial optimization problem. Engineering considerations impose further constraints, e.g. filter wheel balancing requires the filters to have equal mass. The filters must also have the same effective optical path length so as to not change the camera focus; therefore, they must be made of the same substrate and thickness. The optimal filters are chosen from a set of 43 candidate 1-mm thick sapphire filters from a commercial supplier [89] that are compatible with the camera. The transmittances are idealized as having a rectangular "boxcar" spectral profile, so the corresponding **f** vectors are binary, with 1's corresponding to the filter transparent window and 0's for the opaque

elements. Choosing eight filters from 43 candidates results in a total of 1.45×10^8 possible combinations. Hence, a fast and computationally inexpensive measure is needed to quantify the quality of each of these filter sets. These requirements are fulfilled by the CE uncertainty estimation presented in the following section.

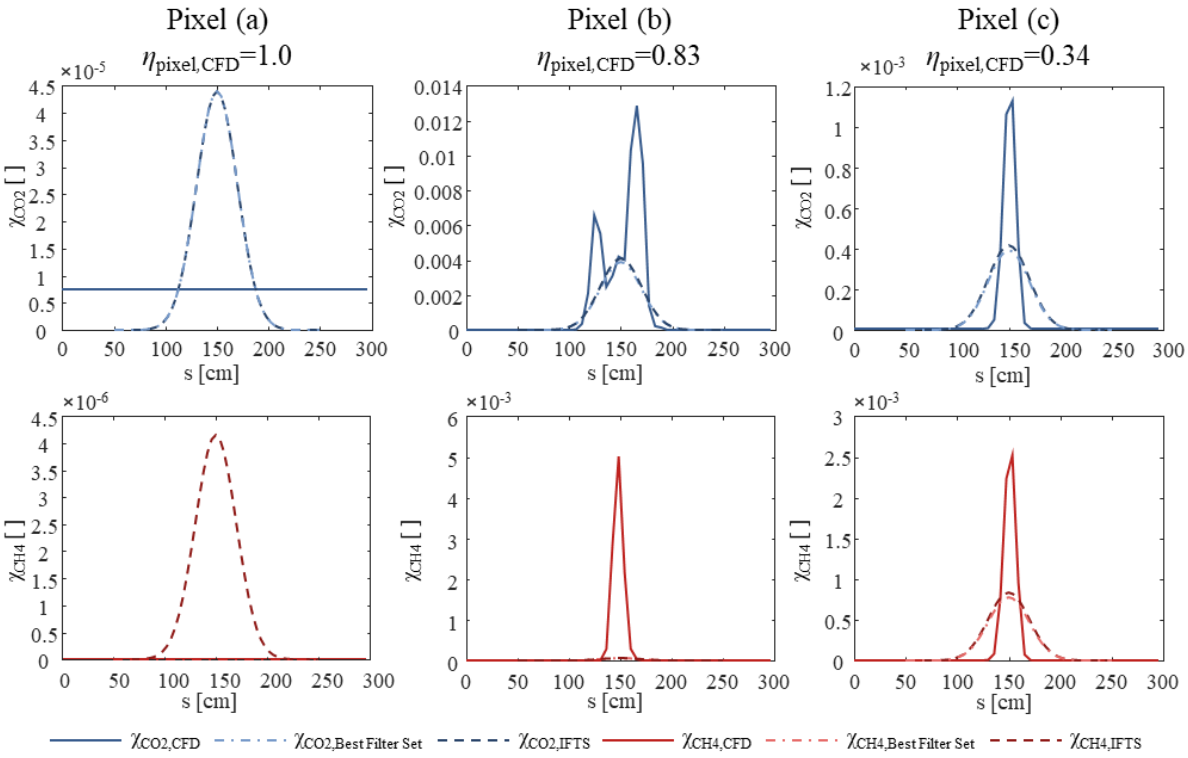

Figure 23 Comparison of the CFD's instantaneous CO_2 and CH_4 concentration profiles with inferred peak concentration using the Gaussian profile for three different pixels.

4.5 Model Error Propagation

The set of optimal filters is found through a design-of-experiments procedure based on minimizing the estimated pixel CE variance. The variance of the estimated flare CE is modelled by the propagation of the measurement noise through the spectroscopic model discussed in Chapter 3. First, the spectral

intensity covariance matrix, representing the measurement noise, is propagated to the filtered camera signal giving the covariance matrix of the filtered signal. Then, the resulting covariance matrix is propagated to the estimated gas state, species number density, and estimated CE. The resulting error propagation is a function of the spectral intensity noise, assumed as constant, and the uncertainty translation factor function. The set of optimal filters that minimizes this function also minimizes the CE uncertainty. To make the uncertainty estimation computationally-tractable, it is assumed that the expected value of the MLE is the same for the filtered evaluations as for the spectrally-resolved evaluation, Eq. (4.4). Put differently, the error in CE due to measurement noise is assumed to have a zero mean. The assumption allows for the linearization of the measurement model around the MLE, $\hat{\mathbf{x}}$.

Considering the signal of one pixel, the covariance matrix of the hypothetical spectral intensity measurement noise is assumed to be independent and identically-distributed (IID)

$$\mathbf{\Gamma}_{\mathcal{J}} = \sigma_{\mathcal{J}}^2 \mathbf{I}, \tag{4.5}$$

where $\sigma_{\mathcal{J}}$ is the measurement noise standard deviation, and $\mathbf{I}$ is the identity matrix whose dimension is the number of spectral bins, *n*. (The assumption of IID noise can be relaxed were one to have a camera-specific noise model.) According to Eq. (4.4), the measurement error covariance matrix for a given filter set described by $\mathbf{\Gamma_S}$ is then

$$\mathbf{\Gamma}_{\mathrm{S}} = \mathbf{F}_{\mathrm{filter}} \mathbf{\Gamma}_{\mathcal{J}} \mathbf{F}_{\mathrm{filter}}^{\mathrm{T}}. \tag{4.6}$$

As the measurement noise is normally-distributed and the measurement model is assumed to be locally-linear, the uncertainty of the MLE of the gas state is also normally-distributed, i.e., the expected values of $\mathbf{x}$ are $\mathcal{N}(\hat{\mathbf{x}}, \mathbf{\Gamma_x})$, with the covariance matrix given by

$$\mathbf{\Gamma}_{\mathbf{x}} = \left(\mathbf{J}_{\mathrm{S}}^{\mathrm{T}} \mathbf{\Gamma}_{\mathrm{S}}^{-1} \mathbf{J}_{\mathrm{S}} \right)^{-1}, \tag{4.7}$$

where $\mathbf{J}_S$ is the filtered sensitivity (Jacobian) matrix, which describes the sensitivity of the pixel brightness with each filter to a variation of the gas state. This Jacobian is found from

$$\mathbf{J}_S = \mathbf{F}_{\text{filter}}\,\mathbf{J}_{\mathcal{J}}, \tag{4.8}$$

where $\mathbf{J}_{\mathcal{J}}$ is the sensitivity of the radiative intensity with the variation of the spectral absorption coefficient caused by gas concentrations or temperature changes around the solution to Eq. (4.4), $\hat{\mathbf{x}}$,

$$J_{\mathcal{J},\text{ij}} = \left.\frac{\partial I_{\eta L,\text{i}}}{\partial x_{\text{j}}}\right|_{\hat{\mathbf{x}}}. \tag{4.9}$$

The uncertainty is further propagated into the species column number density, Eq. (3.22), by

$$\mathbf{\Gamma}_{\text{N}} = \mathbf{J}_{\text{N}}\mathbf{\Gamma}_{\text{x}}\mathbf{J}_{\text{N}}^{\text{T}}, \tag{4.10}$$

where $\mathbf{J}_{\text{N}}$ is the sensitivity (Jacobian) matrix of the column number densities to a variation of the estimated gas state, $\hat{\mathbf{x}}$, given by the partial derivatives of Eq. (3.22),

$$\mathbf{J}_{\text{N}} = \begin{vmatrix} \dfrac{\partial N_{\text{CO2}}}{\partial \chi_{\text{CO2,max}}} & \dfrac{\partial N_{\text{CO2}}}{\partial \chi_{\text{CH4,max}}} & \dfrac{\partial N_{\text{CO2}}}{\partial \chi_{\text{H2O,max}}} & \dfrac{\partial N_{\text{CO2}}}{\partial T_{\text{max}}} \\ \dfrac{\partial N_{\text{CH4}}}{\partial \chi_{\text{CO2,max}}} & \dfrac{\partial N_{\text{CH4}}}{\partial \chi_{\text{CH4,max}}} & \dfrac{\partial N_{\text{CH4}}}{\partial \chi_{\text{H2O,max}}} & \dfrac{\partial N_{\text{CH4}}}{\partial T_{\text{max}}} \end{vmatrix}. \tag{4.11}$$

The sensitivity of the column number density of the k^{th} species to the peak value of the same species is given by

$$\frac{\partial N_{\text{k}}}{\partial \chi_{\text{k,max}}} = \frac{p}{k_{\text{B}}}\int_0^L \frac{G}{\left(T_{\text{max}} - T_{\text{amb}}\right)G + T_{\text{amb}}}\,\text{ds}, \tag{4.12}$$

where $G = \exp\left(-s^2/2\sigma^2\right)$, while the sensitivity of the column number density to temperature peak is given by

$$\frac{\partial N_{\mathrm{k}}}{\partial T_{\max}} = \frac{p}{k_{\mathrm{B}}} \int_0^L \frac{-\chi_{\mathrm{k,max}} G^2}{\left[\left(T_{\max} - T_{\mathrm{amb}} \right) G + T_{\mathrm{amb}} \right]^2} \mathrm{ds} \quad . \tag{4.13}$$

The column number density for one species is independent of other species, so the other elements of this matrix are equal to zero. Noise effects are propagated to the pixel CE by

$$\mathbf{\Gamma}_{\mathrm{CE}} = \mathbf{J}_{\mathrm{CE}} \mathbf{\Gamma}_{\mathrm{N}} \mathbf{J}_{\mathrm{CE}}^{\mathrm{T}} , \tag{4.14}$$

where $\mathbf{J}_{\mathrm{CE}}$ is the sensitivity matrix of the CE values to column number density variation given by the partial derivatives of Eq. (4.3).

$$\mathbf{J}_{\mathrm{CE}} = \begin{vmatrix} \dfrac{N_{\mathrm{CH4}}}{\left(N_{\mathrm{CO2}} + N_{\mathrm{CH4}} \right)^2} & \dfrac{-N_{\mathrm{CO2}}}{\left(N_{\mathrm{CO2}} + N_{\mathrm{CH4}} \right)^2} \end{vmatrix} . \tag{4.15}$$

Summarizing the covariance matrixes given by Eqs. (4.10), (4.7), (4.6), and (4.5), in Eq. (4.14), the pixel CE variance can be rewritten as

$$\mathbf{\Gamma}_{\mathrm{CE}} = \mathbf{J}_{\mathrm{CE}} \mathbf{J}_{\mathrm{N}} \left[\mathbf{J}_{\mathrm{S}}^{\mathrm{T}} \left(\mathbf{F}_{\mathrm{filter}} \mathbf{I} \mathbf{F}_{\mathrm{filter}}{}^{\mathrm{T}} \right)^{-1} \mathbf{J}_{\mathrm{S}} \right]^{-1} \mathbf{J}_{\mathrm{N}}^{\mathrm{T}} \mathbf{J}_{\mathrm{CE}}^{\mathrm{T}} \sigma_{\vec{J}}^2 = \alpha^2 \sigma_{\vec{J}}^2 , \tag{4.16}$$

where α is the uncertainty translation factor from spectral intensity noise to CE uncertainty. So, in order to minimize CE uncertainty, α is minimized under variation of the filter sets,

$$\mathbf{F}_{\mathrm{filter}}{}^{*} = \arg\min_{\mathbf{F}_{\mathrm{filter}}} \left\{ \alpha \left(\mathbf{F}_{\mathrm{filter}}, \mathbf{x} \right)^2 \right\} , \tag{4.17}$$

where $\mathbf{F}_{\mathrm{filter}}{}^{*}$ specifies the optimal filter configuration. It is important to note that the variance depends on the expected gas state, **x**, as a result of the non-linearity of the model and the sensitivities matrixes are linearized around the MLE, Eq. (4.4). Hence, α is calculated for each one of the 13 sample pixels and six time steps as described in the previous section, and the average α^2 weighted by the number density of carbon atoms in each pixel is used to quantify the quality of the filter set.

4.6 Filter Selection Results

Conducting the uncertainty propagation for all 1.45×10^8 possible filter sets took ten days on a computer with six cores and a 3.2 GHz (AMD Ryzen 5 1600) processor. After sorting the resulting CE uncertainties for the ten best and the ten worst filters set choices, several examples from this rank order are discussed. Figure 24 shows the filter sets yielding the best (Table 3), the second-best, the 10th best, and the worst α value.

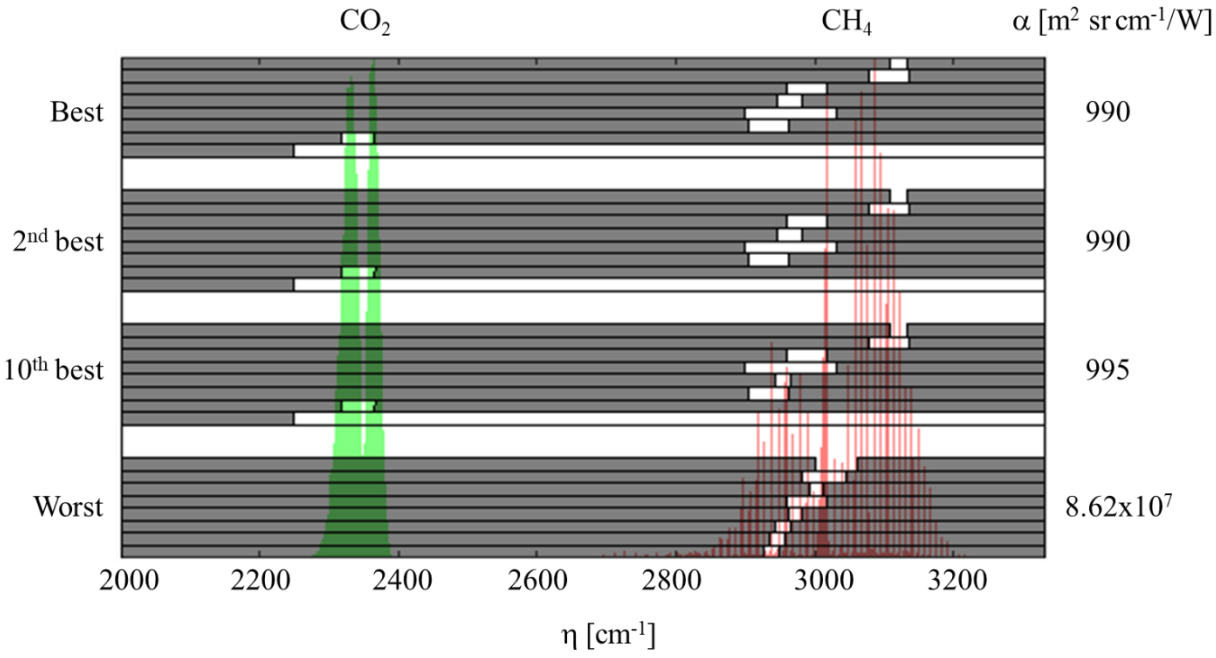

Figure 24 Rank order of the filter combinations according to uncertainty propagation factor, α. Transparent sections of the filter bars correspond to high transmissivity regions. The location of the absorption spectra for CO_2 and CH_4 at 400 K are shown in the background.

To interpret these filter choices, here are some heuristic statements about the likely attributes of a good filter set:

1. As CE depends on the methane and carbon dioxide number density, the absorption bands of both species need to be covered by independent filters.

2. The temperature also needs to be inferred since the absolute number densities of each species depend on temperature, and, importantly, the measured intensity is due to both species' concentration and temperature. Hence, the filter sets need to cover spectral portions of each band with opposing temperature behaviour — for example, the two ends of a band.

These points lead to the heuristic expectation that, for a good filter set choice, the band of each species needs to be covered by at least two filter windows with a small overlap to enable the inference of temperatures.

Table 3 Multispectral broadband camera filter set optimized to estimate flare CE.

Filter[8]	η_{Low} [cm-1]	η_{High} [cm-1]	τ
NB-3205-025nm	3108	3132	0.5
NB-3220-060nm	3077	3135	0.7
NB-3345-065nm	2961	3019	0.65
NB-3375-040nm	2946	2981	0.8
NB-3375-150nm	2899	3030	0.8
NB-3410-068nm	2904	2962	0.6
NB-4270-085nm	2319	2366	0.7
SP-4500nm	2249	3333	0.85

The rank order found with the design-of-experiments procedure supports these expectations: the best filter sets feature at least two filter windows for each species band, and these bands are sufficiently orthonormal in order to estimate the temperature. Of course, most pixels feature

[8] NB-CWL-FWHM denotes a narrowband filter with center wavelength (CWL) and full width at half maximum (FWHM) transmissivity. The short-pass filter nomenclature is SP-cutoff at 5% of peak transmittance, η_{Low} and η_{High} are the low and high half transmittance wavenumber, and τ is the peak transmittance.

significantly lower methane content than carbon dioxide content, making the CE highly sensitive to the methane concentration. Hence, a majority of the filter windows are placed on the methane band in order to decrease the uncertainty in methane concentration; this highlights the importance of minimizing the covariance of the derived quantity (here CE, Eq. (4.14)) when deriving the objective function, as opposed to minimizing the covariance of the species-of-interest, Eq. (4.10). The second-best filter set follows a similar scheme with a slightly wider (1.6 cm^{-1}) narrowband filter in the CO_2 spectral band. This filter set is rated somewhat lower than the first because the combination of the two filters in the CO_2 spectral band provides less specific information about the thermodynamic state of the gas.

Nonetheless, the difference between these filter sets is minimal. On the other hand, the α-factor is five orders of magnitude higher for the worst filter set than for the 10^{th} best set, as the filter set essentially disallows the inference of a carbon dioxide concentration and thus of a CE value. Furthermore, the filter windows on the methane band strongly overlap, which impairs the ability to obtain a robust temperature estimate.

The predictive ability of the design-of-experiments procedure is quantitatively assessed using a Monte Carlo approach for a subset of 40 candidate filters, including the best and worst filters. For each filter set, simulated measurements are contaminated with a random Gaussian noise vector, and the MLE is evaluated according to Eq. (3.27). The performance of each filter is assessed from 640 trials, consisting of the 20 sample pixels with satisfied Karush–Kuhn–Tucker condition using the resolved spectrum intensity in different locations and time steps, each with 32 random noise vectors drawn from the same error distribution. The empirical value α_{MC} calculated from these sets is retrieved and compared with the estimate from the propagation-of-error procedure, Eq. (4.16).

Figure 25 shows that the linear error propagation and the Monte Carlo simulation values follow the same trend, validating the design-of-experiments technique. In some cases, the trust-region reflective algorithm did not converge; this mostly occurred for very poor filter choices due to the ill-posedness of the underlying filter. Discrepancies can be partially explained by the assumption of a locally-linear measurement model used in the uncertainty propagation. In reality, the underlying problem is nonlinear, and the recovered state found by minimizing Eq. (3.27) depends on the initial values, in the case of a large variance between the inferred values.

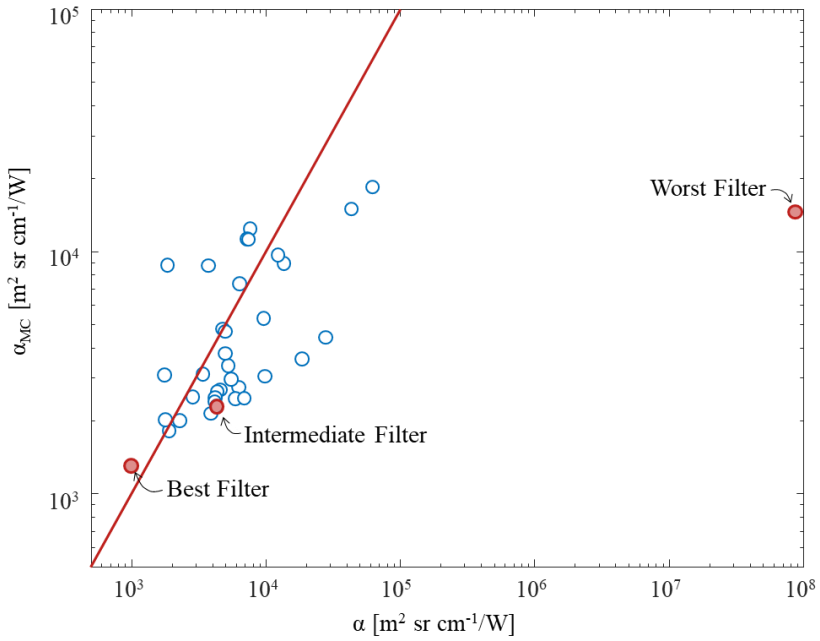

Figure 25 Comparison of the uncertainty translation factor inferred from the sensitivity analysis.

On the other hand, when a small amount of noise contaminates the measurement data, numerical error dominates the solutions, and the ratio between the input noise and CE uncertainty is contaminated with numerical error. Moving to filters with the worst estimated uncertainty, the variance of the solutions becomes limited by upper and lower bounds imposed on the variables during nonlinear

regression, resulting in an upper limit for α_{MC}. However, the significance for the best filter sets is not impaired.

Further insight is obtained by plotting the CFD ground truth combustion efficiency versus the optically-inferred value from the noisy data. Figure 26 illustrates that the best filter set minimizes the variance of the CE estimates, as predicted by Eq. (4.16), while the intermediate filter and worst filter have higher variances. Figure 26 also shows the estimates obtained by minimizing the residual between noisy data and the Gaussian model over each discrete wavenumber, which would be obtained using an IFTS. These values are nearly always superior to the estimates obtained using the filter wheel camera, highlighting the fact that the spectral convolution over each filter, Eq. (3.14), makes the inference problem ill-posed and more susceptible to measurement noise as well as the model error involved in assuming that the species and temperature distributions obey a Gaussian distribution along each LOS.

The inferred CE becomes less accurate for higher CE values, and at a CE of unity the inferred value is unreliable for all filter sets. This is because the CE is highly sensitive to uncertainty in CO_2 concentration since it is in the denominator of Eq. (4.3). As shown in Figure 21, Pixel (a) lies outside the flare plume, and the corresponding CO_2 concentration is relatively small. Thus the SNR of the corresponding MWIR measurement is low and, therefore, highly susceptible to noise. Figure 27 shows that the most reliable estimates for N_{CO2} and N_{CH4} are for the low combustion efficiency case. In the case of the worst filter set, the variance in N_{CO2} is especially large because, as shown in Figure 24, there are no filters at the CO_2 spectral band and no change in the filtered signals with a change in CO_2 concentration, i.e. any concentration of CO_2 can generate the same measured signal.

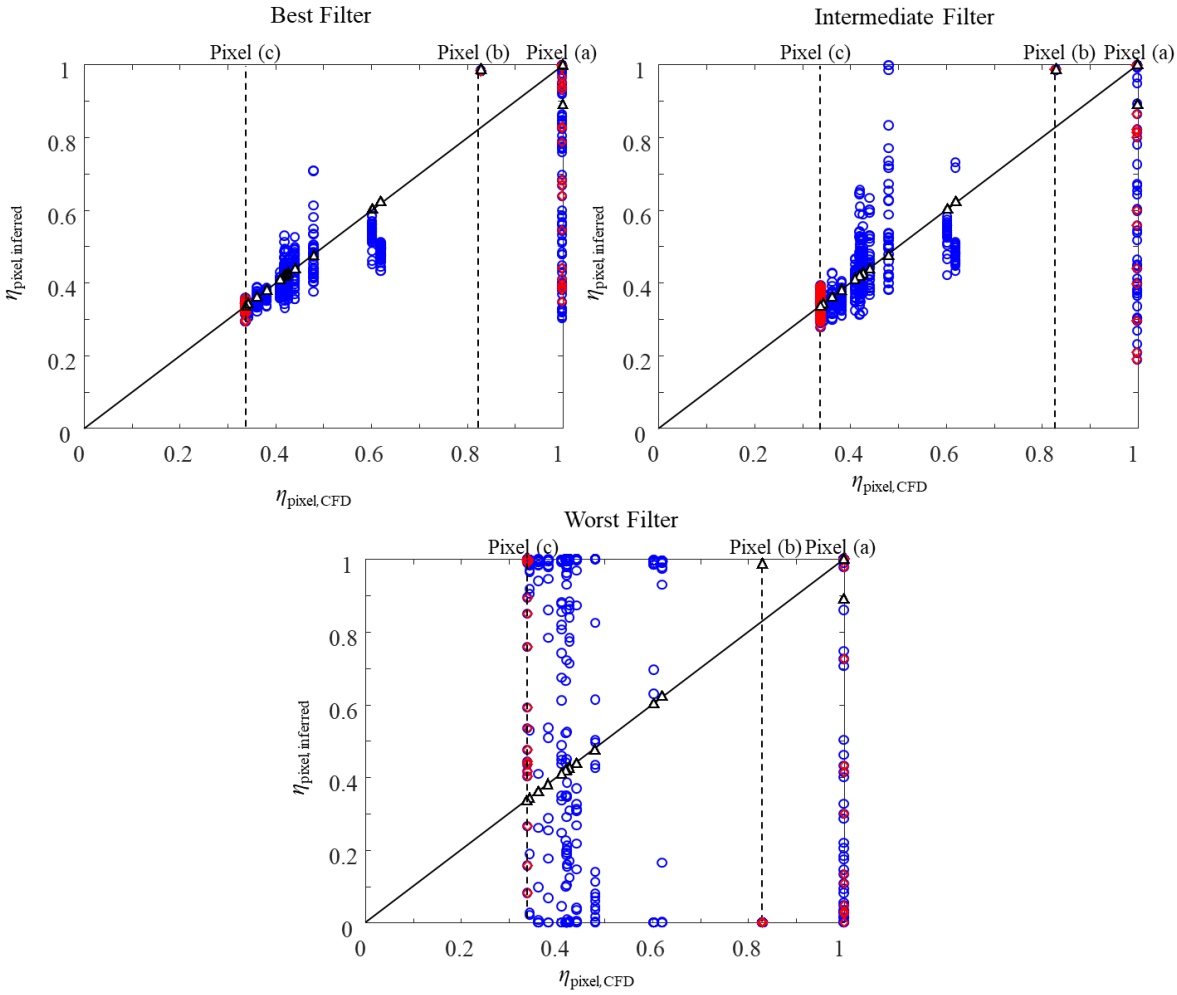

Figure 26 Comparison of MWIR CE estimates with CFD ground truth values. "Best," "Intermediate," and "Worst" filters refer to those shown in Figure 24. Red diamonds indicate pixels a, b, and c, shown in Figure 21, blue circles are other pixels, and black triangles are values found using spectrally-resolved data (IFTS measurement).

The large variance of pixels with low concentrations of CH_4 and CO_2 does not significantly affect the filter selection as the objective function defined by Eqs. (4.5) - (4.16) is weighted by the species-of-interest column number, and the overall flare CE is calculated using the mass flow of each species by Eq. (3.25).

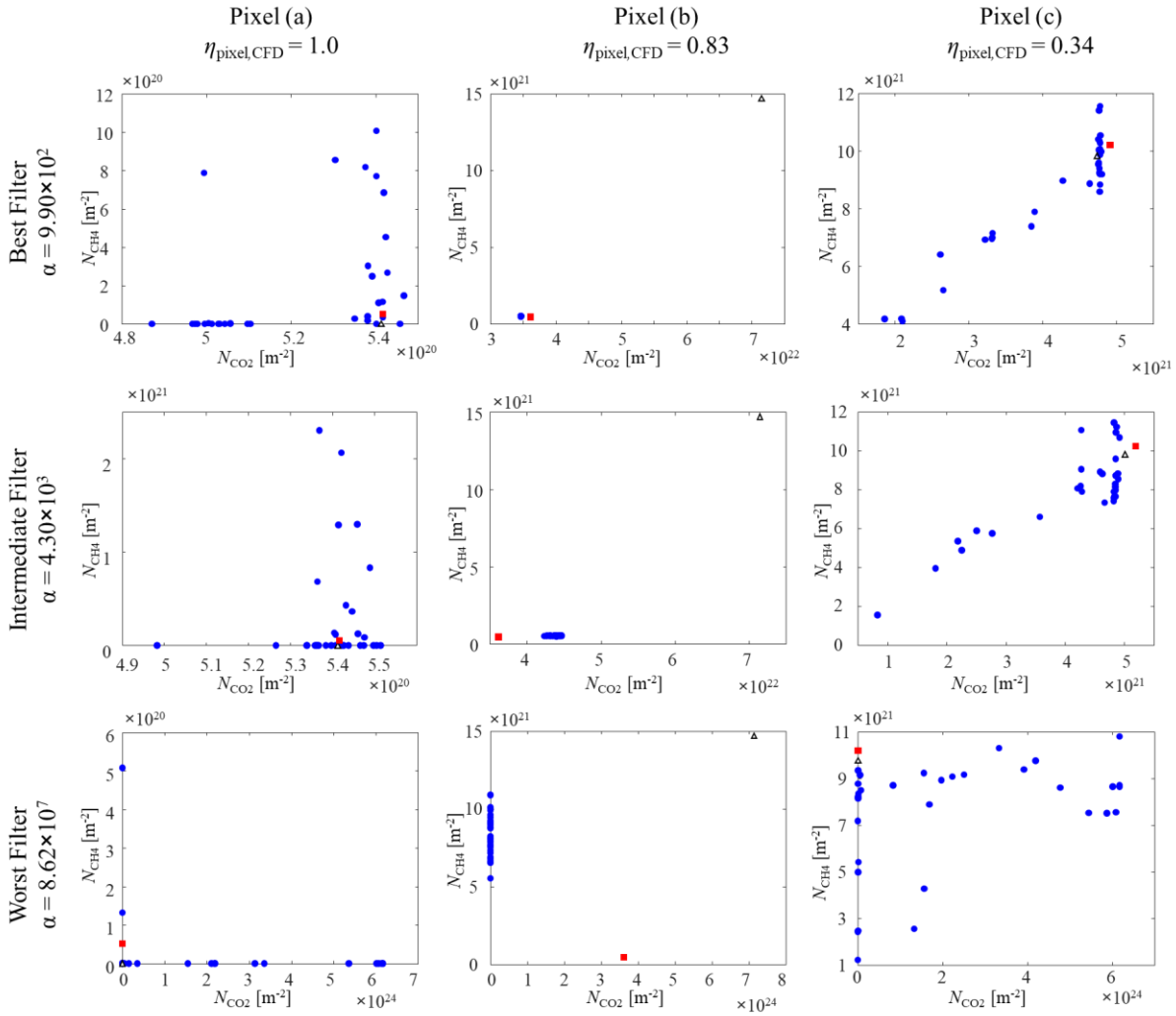

Figure 27 Recovered CO_2 and CH_4 path integrated number densities for pixels (a), (b), and (c) in Figure 21 and the best, intermediate, and worst filters shown in Figure 24 for randomly-noised data. Blue circles show estimates derived from multispectral MWIR images, while the black diamond shows the IFTS estimate. The CFD ground truth is shown as a red square.

4.7 Conclusions

QOGI is becoming a mainstay technique for estimating the concentration and mass flux of mixtures containing a single radiatively-participating species. It can be extended to assess gases containing multiple participating species by analyzing near-simultaneous IR images taken over different spectral ranges.

This chapter presents a generalized procedure for optimizing the detection spectra for multi-species QOGI, which is demonstrated in the case of estimating the CE of a flare. The filter selection method is based on a simplified evaluation of measurement error propagation to the CE uncertainty. The linearization and assumption of unbiased error distribution results in a numerically-efficient method, allowing for the rating of 1.45×10^{8} filter sets in 10 days on a personal computer. The results are found to be physically-plausible, and a comparison to Monte Carlo simulations conducted on a subset of filter choices supports the given rank order. Furthermore, the presented method can easily be transferred to remote sensing problems that allow for sample data generation.

The results of this chapter showed that accuracy of the quantity-of-interest inferred from QOGI using multispectral cameras strongly depends on the chosen measurement spectrum. A good set of filters contains specific spectral features that are sensitive to individual fitting parameters. However, in the case of MS cameras, reducing the filter spectral window to capture independent signals decrease the SNR as noise is mainly from electronic source. The next chapter explores how an imaging Fourier transform spectrometer, which provides highly-spectrally resolved information about the flare plume, may circumvent this shortcoming.

Chapter 5

Assessing Flare Combustion Efficiency using Imaging Fourier Transform Spectroscopy

Concerns about the impact of flaring on climate change, particularly when considering non-ideal flaring conditions, motivate a need for reliable techniques to quantify flare CE. Recent advancements in mid-infrared optoelectronics, particularly the development of the IFTS, make stand-off measurements of flare CE theoretically possible. These instruments combine the spectral resolution of a line spectrometer and the spatial resolution of an IR camera to provide 2D hyperspectral images of a scene. In the context of quantifying gas emissions, many IFTSs have sufficient spectral resolution to "fingerprint" gaseous species from absorption and emission lines.

This study assesses the potential of using IFTSs to directly measure the combustion efficiency by combining species column densities estimated from the spectroscopic model with intensity-weighted velocities found using the optical flow model. The theoretical viability of this approach is established by inverting synthetic IFTS data generated using a CFD-LES of a flare in a crosswind. Next, the measurement model is verified by recovering mass flow rates of CH_4 and CO_2 mixtures from a heated vent apparatus. Finally, preliminary measurements are presented on a laboratory-scale steam- and air-assisted flare. While the simulated measurements and heated vent experiments support the feasibility of this approach, experimentally-derived spectra from the lab-scale flare were contaminated with SCAs

attributed to turbulent fluctuations, which complicates the quantitative interpretation of the IFTS data. The results and procedure presented in this chapter are presented in the published article [90][9].

5.1 CFD Prof-of-Concept Study

The viability of this measurement procedure, in particular the approach used to infer the species column densities from the recorded intensity spectrum, is assessed using simulated measurements carried out on the plume of a flare in a crosswind. Synthetic camera data were generated using the CFD data and procedure described in Section 4.4.1. As this case uses an IFTS instead of the MS camera in Chapter 4 the spectral intensity is downsampled using Eq. (3.17) to simulate an ideal MWIR IFTS having a resolution of 4 cm^{-1} and spectral range of 2000 to 3300 cm^{-1}.

Since the objective of this analysis is to assess the accuracy of the species column density, pixel CE is defined according to Eq. (4.3), where the column densities are computed from Eq. (3.22). Figure 28 shows sampled pixels used in this study with the local CE at one instant in the CFD simulation. The red line indicates the 800 K isotherm, which roughly corresponds to the flame envelope.

[9] This paper is coauthored by Sina Talebi-Moghaddam who helped in the methodology and software; Milad Zamani helped in the investigation; Caroline Turcotte provided the resources, review, and editing; Kyle J. Daun helped in the creation of the concept, methodology, supervision, review, editing, project administration, supervision, and funding acquisition.

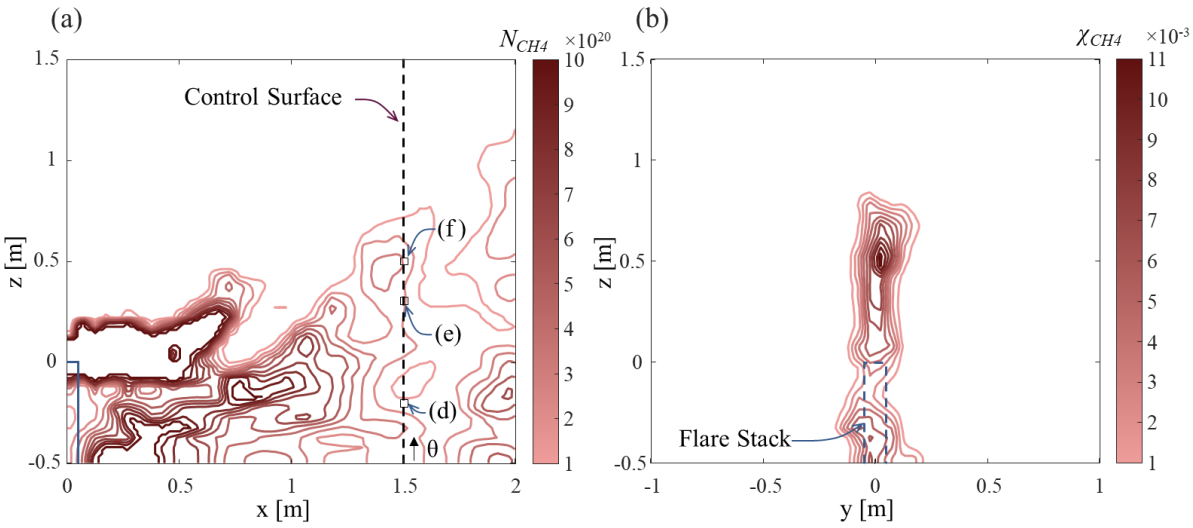

Figure 28 CFD timestep 30 CH_4 (a) column number contour plot, and (b) volume fractions contour plot at x = 1.5. The dashed line indicates the plane used to extract the data shown in Figure 29 and the pixels used to infer the CE, while the squares indicate the location of the LOS in Figure 30, (d) at z = -0.2 m, (e) z = 0.3 m, and (f) z = 0.5 m. Figure 21 shows the CE for the same timestep.

5.1.1 Column Density Estimation

Concentrations of CH_4, CO_2, H_2O, and temperature along each LOS must be obtained simultaneously from the spectroscopic data since all these variables influence the spectral intensity that reaches the camera. As discussed in Section 3.2.1, this process is ill-posed as multiple temperatures and concentration distributions along each LOS exist that produce nearly identical spectra when substituted into the measurement equations. Consequently, species volume fractions and temperature distributions are parameterized as Gaussian, Eq. (3.26). The plume thickness parameter, σ, is specified based on the observed plume height along the chord length in the camera image and is assumed to be the 1 m for both the temperature and volume fraction of every species. This approximation becomes reasonable in

flows dominated by turbulent mixing. MLE for the species and temperature distribution parameters, $\mathbf{x} = [\chi_{CH4,max}, \chi_{CO2,max}, \chi_{H2O,max}, T_{max}]^T$, are found using Eq. (3.27) where $\mathbf{S^{meas}}$ contains the synthetic IFTS data, **S(x)** is the corresponding modelled intensities generated using the Gaussian profiles. The measurement error covariance matrix, $\mathbf{\Gamma_S}$, is modelled as diagonal, where each element is the corresponding camera noise variance for each spectral bin. The MLE parameters, $\hat{\mathbf{x}}$, are then used to infer the column number densities of the species-of-interest using Eq. (3.22).

5.1.2 Proof-of-Concept Results

The CO_2 and CH_4 column number densities corresponding to the measurement plane in Figure 28 are plotted in Figure 29 (a). The high concentration of unburned CH_4 below the flare is due to the aerodynamic fuel stripping mechanism. In both cases, the IFTS-inferred concentrations reasonably agree with the CFD ground truth values and generally reproduce the CO_2 and CH_4 column density trends with *z*. When these column numbers are substituted into Eq. (4.3), they accurately reproduce the ground-truth pixel CE derived from the CFD data, as shown in Figure 29 (b).

Differences between the CFD and IFTS-inferred column densities can be attributed to the ill-posedness of the underlying inference problem and model error introduced by assuming a Gaussian distribution along each LOS for each species concentration and the temperature distribution (*i.e.*, the well-mixed plume approximation.) Were the species concentration inferred through absorption spectroscopy, Eq. (3.13), the overall column density would be less sensitive to the parameterization of the species concentration and temperature along each LOS. In the limiting case of an isothermal gas, and assuming that the intensity measured at a given wavelength is due only to the k^{th} species,

$$\ln\left(I_{0\eta}/I_{L\eta}\right) = \int_0^L \kappa_{\eta,k}(s)\,ds \quad . \tag{5.1}$$

Substituting the absorption coefficient from Eq. (3.7) gives

$$\ln\left(I_{0\eta}/I_{L\eta}\right)=S_{k,ij}\left(T\right)f_V\left(\eta;\eta_{ij},T,p\right)\int_0^L\frac{\chi\left(s\right)p}{k_BT}ds \tag{5.2}$$

in which case the parameterization assumed for $\chi_k(s)$ does not matter, as the integral part of the equation is the column number density. In the case of emission spectroscopy and a nonisothermal gas, the parameterizations of $T(s)$ and $\chi_k(s)$ are connected through the emission term in the RTE and the ideal gas law. For instance, assuming an optically thin spectral line, Eq. (3.12), and negligible background radiation, $I_{0\eta} = 0$, the monochromatic intensity due to an individual species is given by

$$I_{L\eta}=\int_0^L\kappa_{\eta,k}\left(s\right)I_{b\eta}\left[T\left(s\right)\right]ds, \tag{5.3}$$

so accurate retrieval of $\kappa_{\eta,k}(s)$, and hence $\chi_k(s)$ and N_k, depend on the accuracy of the presumed distributions for both $\chi_k(s)$ and $T(s)$.

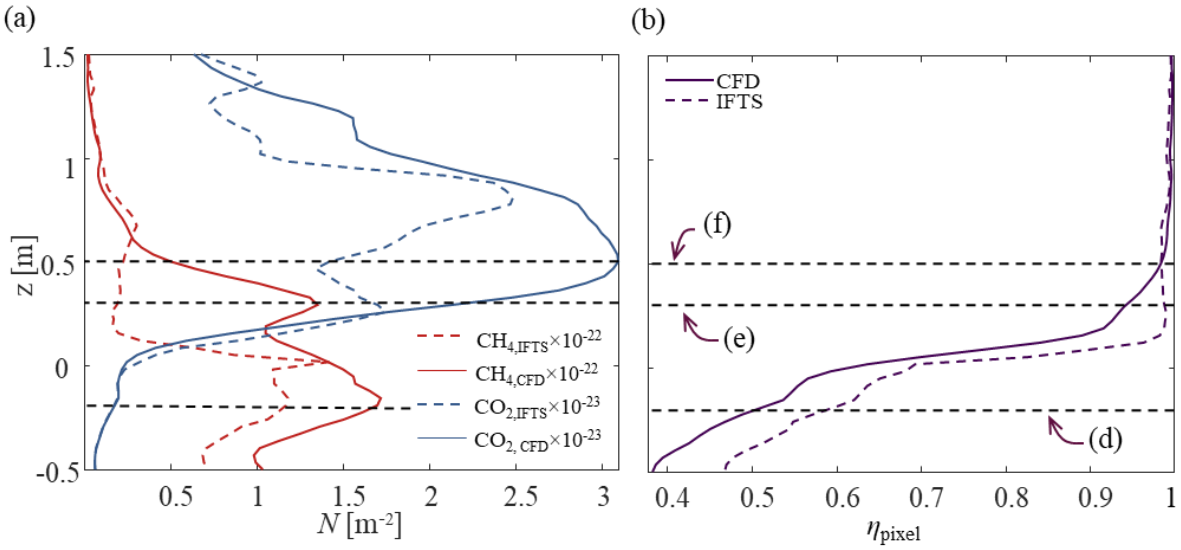

Figure 29 (a) CO_2 and CH_4 column densities along the control surface shown in Figure 28; (b) the corresponding local CE from Eq. (4.3). Dashed lines indicate the LOS positions in Figure 28.

Further insights into this aspect of the inference problem are found by plotting temperature and species volume fractions along LOS at −0.2, 0.3, and 0.5 m, pixels (d), (e), and (f) shown in Figure 30. At $z = -0.2$ m (pixel (d)), the CE is overpredicted because the CH_4 column density is underpredicted, as shown in Figure 29 (a). Although the temperature profile does not follow a Gaussian distribution, it is close to ambient temperature and does not generate a significant error in the inferred column density. Instead, as the plume thickness assumed for both species is broader than the ground truth, both peak concentrations are underestimated. However, the CO_2 ground truth distribution has a small "bump" before the plume centre that aligns with the temperature peak, increasing the spectral intensity over the CO_2 bands and, consequently, the inferred CO_2 concentration. At $z = 0.3$ m (pixel (e)), the inferred CE is close to unity, while the ground truth CE is lower. The CE overprediction is because the CH_4 concentration is underpredicted, as shown in Figure 29 (a).

Figure 30 shows that the distribution shapes for temperature and CO_2 are generally similar, as one would expect since the combustion reaction releases CO_2 and locally increases the gas temperature. For the same reason, high concentrations of CH_4 correspond to low concentrations of CO_2. As the inferred temperature is higher than the CFD temperature in regions of high CH_4 concentration, the inferred CH_4 concentration is lower than the ground truth concentration to generate an equivalent spectral intensity over the CH_4 bands. At $z = 0.5$ m (pixel (f)), the inferred CE is close to the ground truth, but the temperature is overpredicted, and the column densities of both CO_2 and CH_4 are underpredicted. Nevertheless, the ill-posedness of the inference problem and the assumption of Gaussian profiles having a specified width results in significant differences between the inferred volume fractions along a LOS and the CFD ground-truth. These errors are, to a large extent, "integrated out" when obtaining the column densities and the local CE, suggesting the overall feasibility of this technique.

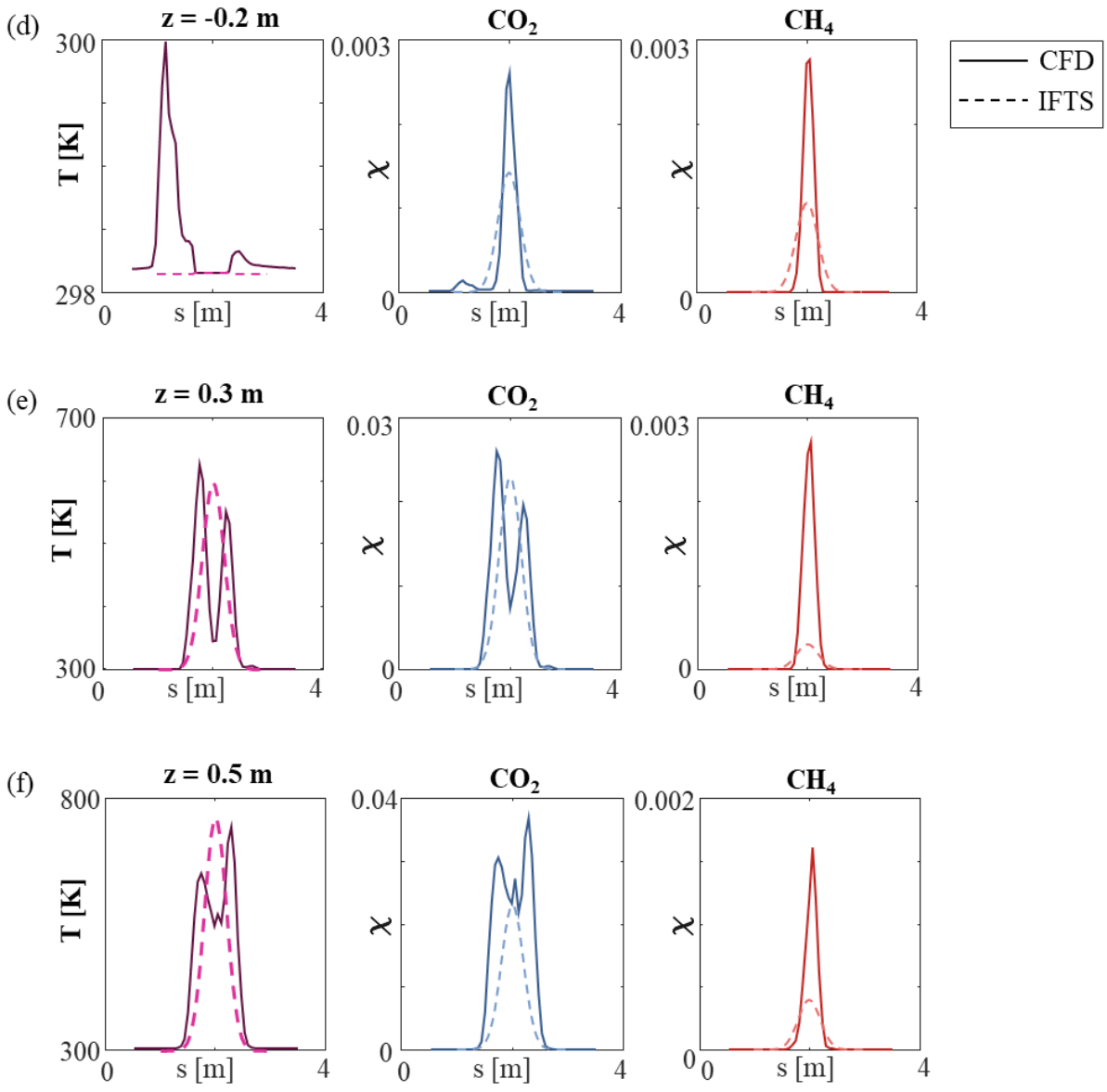

Figure 30 Plot of CFD-derived and IFTS-inferred species concentrations for the pixels indicated in Figure 28. Top row (d) *z* = –0.2; middle row (e) *z* = 0.3; bottom row (f) *z* = 0.5 m.

5.2 Experimental Analysis

The viability of this measurement technique is next assessed by measuring gas concentrations and flow rates in an experimental setting, using a Telops Hyper-Cam MWIR with a measurement resolution of 4 cm^{-1}. The analysis is done in two stages: first, the Hyper-Cam is used to recover the concentration and flow rates of a heated mixture of CH_4/CO_2 without combustion. Next, the instrument is used to analyze the plume of lab-scale steam- and air-assisted flares.

5.2.1 Heated Vent Experiments

Heated plumes of a CH_4/CO_2 mixture were generated using the apparatus shown schematically in Figure 31. Flow rates were controlled using two mass flow controllers (Brooks GF40) to produce a CH_4/CO_2 volume mixture fraction of 0.5 while maintaining a total volumetric flow of 10 standard litres per minute (SLPM). The gas flowed through a heated line before being discharged from a 19 mm diameter nozzle. The gas temperature was measured using a K-type thermocouple in the gas flow at the nozzle discharge, which was maintained at approximately 40 K above the ambient temperature of 294 K.

The gas plume discharged against a background of four 15 cm × 15 cm aluminum plates arranged vertically behind the plume. The plates are painted matt black (Krylon k01602 Ultra-Flat black) with a spectral emissivity ranging between 0.95 and 0.97 over the measurement spectrum of the IFTS and approximated as perfectly black in the radiative transfer model. The plates were maintained at 273 K using a water/ethylene glycol mixture, which produced a background intensity one may expect when carrying out a field measurement on a cloudy day. This temperature is higher than the ambient dew point, ensuring no condensation is formed on the plates. The IFTS aperture is 2.1 m away from the plume centerline and 2.2 m away from the background plates.

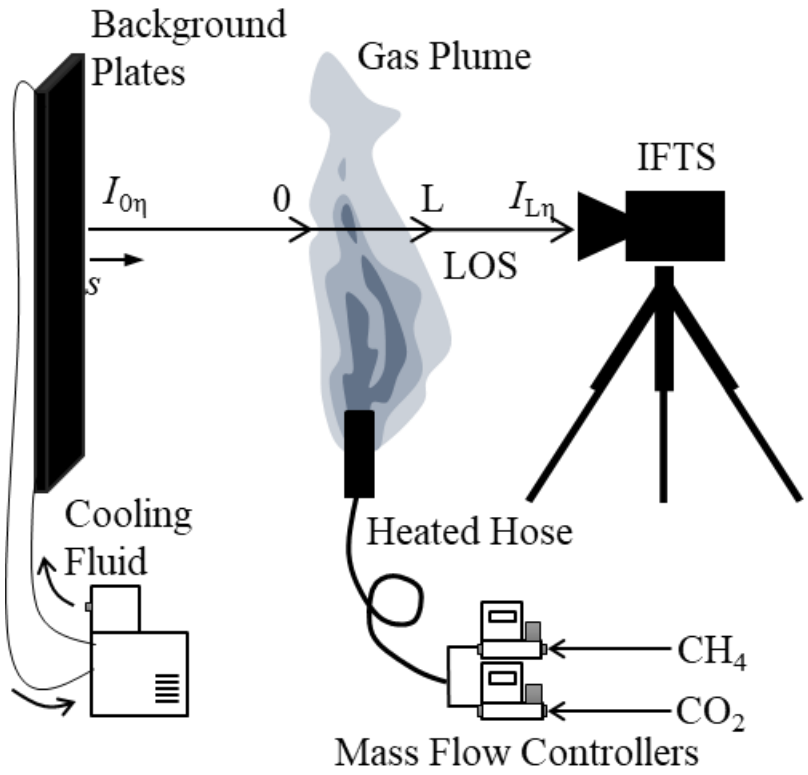

Figure 31 Schematic of the heated vent experiment. The mixture of CO_2 and CH_4 is heated and released between a cold black background and the IFTS.

Figure 32 shows sample IFTS images corresponding to wavenumbers of 2336 cm^{-1} and 2453 cm^{-1}, along with the spectral intensity corresponding to the median of 50 datacubes of the indicated pixel. The plume is most visible in the 2336 cm^{-1} image but also at 2453 cm^{-1}, outside the CO_2 or CH_4 band, due to scene change artifacts.

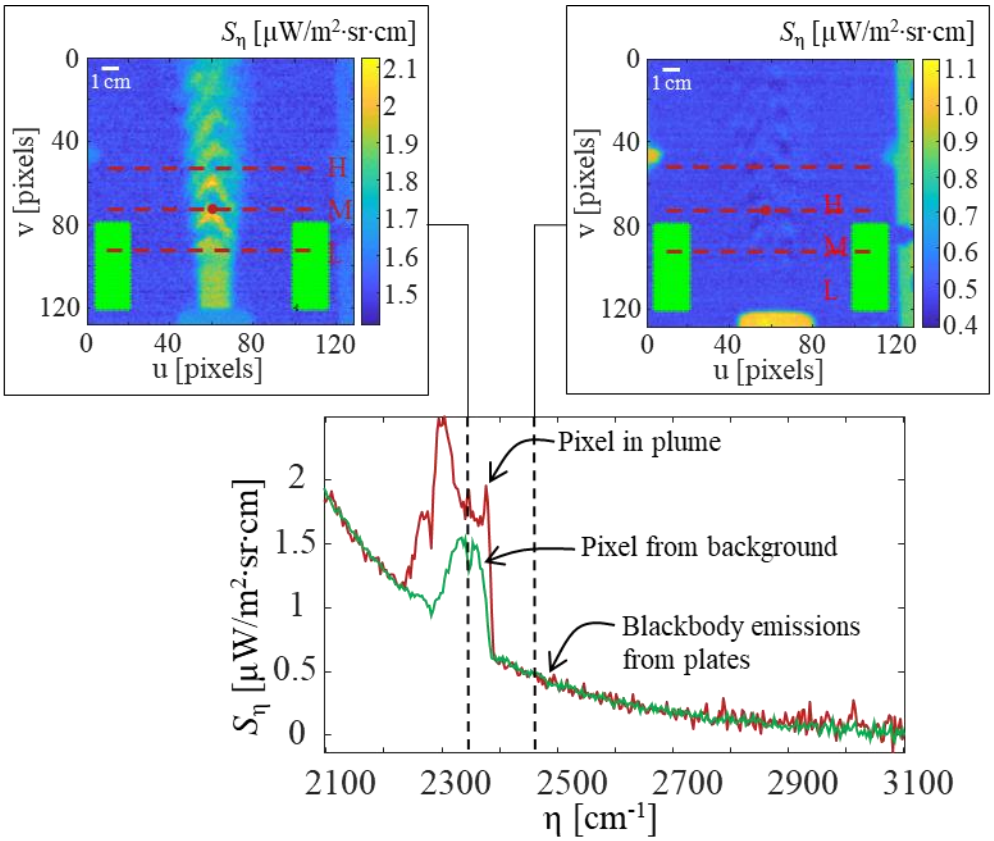

Figure 32 Hyperspectral images of the 50%/50% CH_4/CO_2 plume at 2336 cm^{-1} and 2453 cm^{-1}, and corresponding measurement spectra for pixels from the background and within the plume. The red dashed lines in the hyperspectral image show the integration surface, while the background pixels used to obtain the distributions in Figure 33 are green. The spectrum is found by averaging 50 datacubes.

The hypercubes are analyzed as follows. First, pixels from outside the plume, shown in green, are analyzed to infer the background intensity and ambient CO_2 concentration and temperature. The ambient gas is modelled as homogenous between the background and the camera aperture. The RTE measurement model is used to recover the ambient state for the LOS corresponding to the background pixels. Probability distributions of the background temperature, ambient CO_2 temperature, and

concentration are shown in Figure 33. Ambient H_2O was also inferred from the background spectrum; however, the spectral intensity has the same order of magnitude as the measurement noise. The result did not converge, showing that ambient H_2O does not affect the measurements over the path length between the plume and the camera.

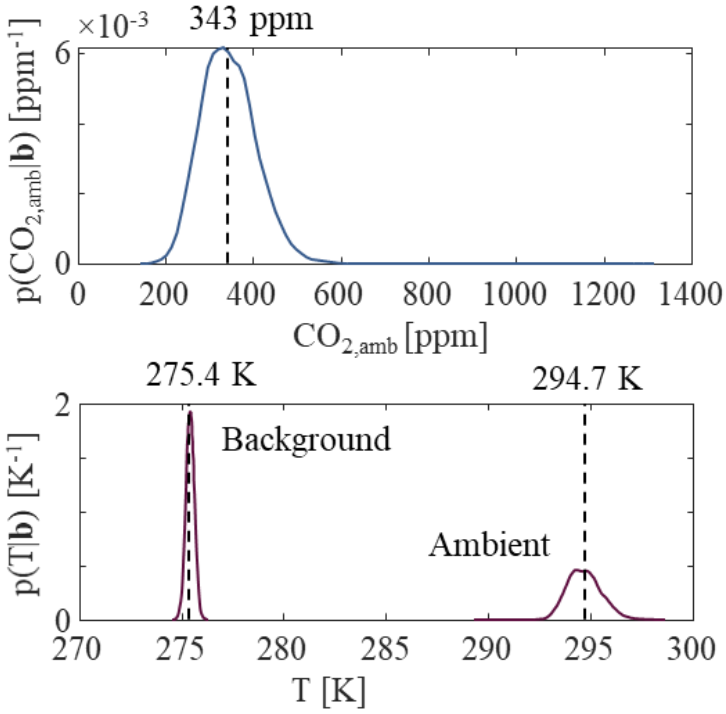

Figure 33 Probability density functions for CO_2, background temperature, and ambient gas temperature inferred using the background (green) pixels shown in Figure 32.

Mean values for these parameters are then incorporated into the RTE model used to analyze the pixels along the control surfaces (red dashed lines) shown in the hyperspectral images in Figure 32. The peak volume fractions and temperature were inferred using Eq. (3.27) for a characteristic plume width, σ, of 6 cm, based on the visible plume in the images. Recovered CO_2 and CH_4 peak volume fractions and temperature profiles inferred on the control surface "M" are plotted in Figure 34 (a). The

peak volume fractions follow a roughly Gaussian distribution with respect to θ, which supports the Gaussian plume hypothesis for this scenario. The peak volume fraction for CH_4 is noisier than CO_2, which may be due to the weaker signal and lower SNR over the spectral region corresponding to the 2900 cm^{-1} band, compared to the 2300 cm^{-1} band.

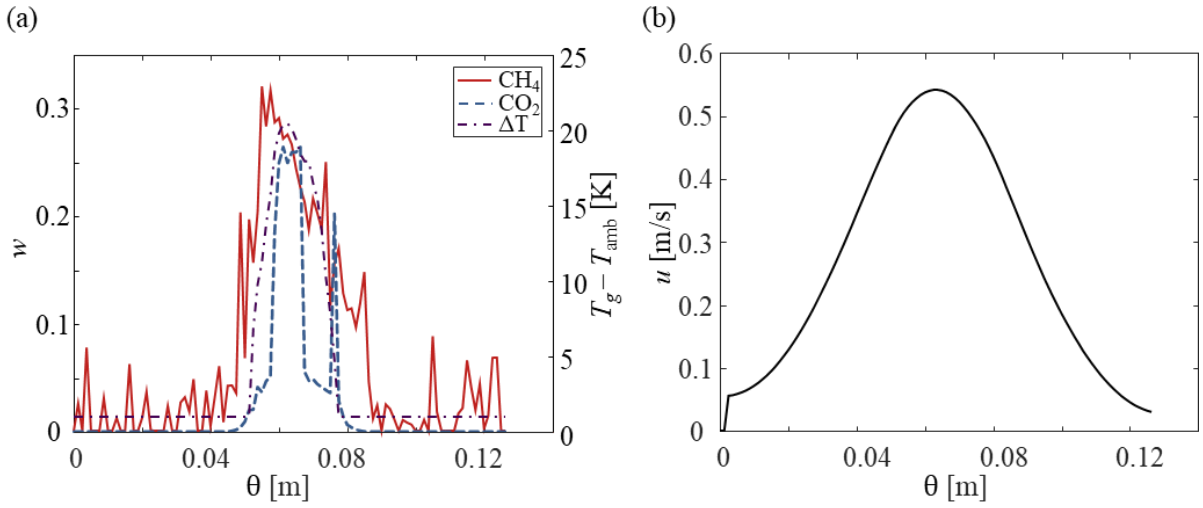

Figure 34 (a) Peak mass fractions and gas temperature and (b) velocity profile along the control surface "M" shown in Figure 32.

The velocity profile along the control surfaces is inferred using the optical flow algorithm described in Section 3.2.2. Figure 34 (b) shows the averaged *y*-component velocity of 2600 timesteps calculated using sequential broadband images evaluated over OPDs of $x_k \in$ [-1.247 mm, -0.424 mm], and $x_k \in$ [0.424 mm, 1.247 mm], which avoids artifacts caused by the peak interferogram fluctuations when the mirror is close to its centre position. Combining the velocity profile with the species column densities results in the mass flow rates shown in Table 4. The results are in good agreement with the values inferred from the mass flow controllers and the equivalent CE derived by substituting the mass flow rates into Eq. (2.8). Note that the CE calculation is sensitive to the shape of the velocity profile,

which is used to weigh the column densities according to their location relative to the velocity field, but not the overall velocity magnitude, since the mass flow rate appears in the numerator and denominator in Eq. (3.25).

Table 4 The heated vent experiment imposed and inferred species mass flows and CE.

	Ground Truth (MFC)	IFTS L	IFTS M	IFTS H
$\dot{m}_{CH4}$	0.060 g/s	0.050 g/s	0.066 g/s	0.063 g/s
$\dot{m}_{CO2}$	0.162 g/s	0.167 g/s	0.189 g/s	0.192 g/s
η_{comb}	0.494	0.549	0.513	0.527

5.2.2 Laboratory-Scale Steam- and Air-Assisted Flare

The IFTS is next used to characterize the plume of a laboratory-scale flare, shown in Figure 35. The flare consists of an annular burner having an inner diameter of 11.3 mm, a wall thickness of 0.7 mm, and an outer diameter of 22.9 mm. Fuel is supplied to the annulus, while the assisting fluid, air or steam, is injected through the central tube. Vertical mesh screens confine the flare to prevent the flame from drifting while allowing the air entrainment into the flame and plume. An exhaust hood collects flare combustion products with its flow controlled by a Venturi valve to maintain turbulent flow and keep the combustion products well-mixed. The exhaust duct contains a probe that directs an exhaust gas sample to a photoacoustic extinctiometer (PAX), which measures the concentration of black carbon. The four background plates were aligned horizontally due to the width of the flare plume at 60 cm above the burner tip and used to maintain a background temperature of 276.5 K. More information about the experimental setup can be found in Ref. [36,39].

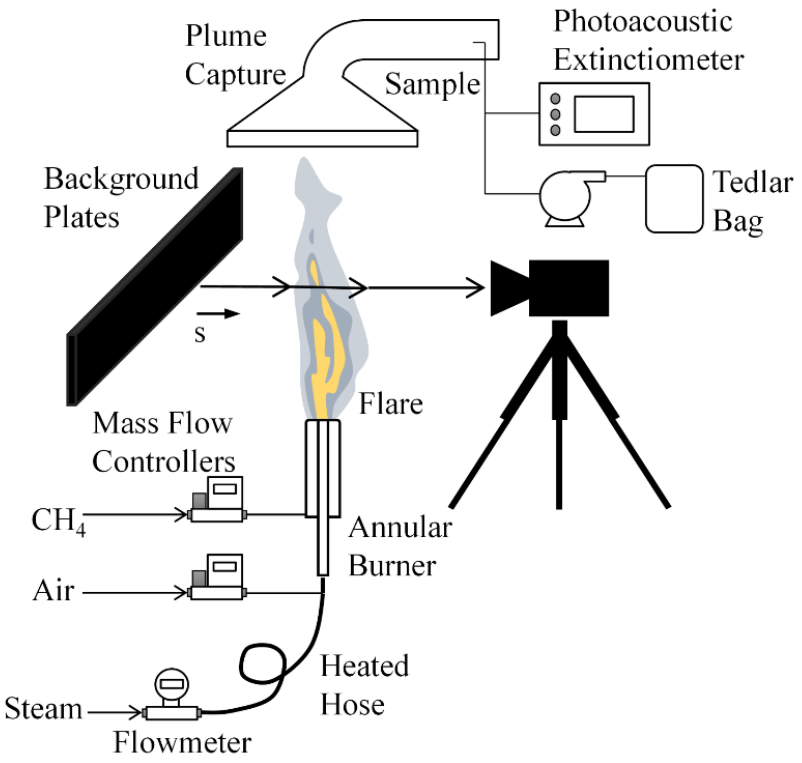

Figure 35 Schematic of the steam- and air-assisted flare experiment. Air- or steam-assisted flare with adjustable assist fluid flowrate release the combustion products between a cold black background and the IFTS.

Methane is supplied to the flare with a flow rate of 5 SLPM. The flare CE is adjusted by varying the assisting fluid flow rate, which is 30, 75, or 120 SLPM of air or 29 g/s of steam. The plume samples are collected into a Tedlar bag and analyzed using a gas chromatograph (GC) (Agilent, 7890B). CH_4, C_2H_6, C_3H_8, CO_2, CO, and H_2 concentrations inferred from this instrument are summarized in Table 5 for the flare operating conditions, which are used to calculate the flare CE. These measurements confirm that the flare CE drops with increasing the air and steam flow rates. The volume fractions are converted into mass flow rates and CE using Eq. (2.10); these values are listed in Table 6.

Table 5 Plume sample species volume fractions, soot concentration and mass flow. Species that were not detected in the sample were excluded from the table (C_2H_6, C_3H_8, CO, and H_2).

Air [SLPM]	Soot [g/m^3] ×10^6	χ_{CH4} [] ×10^3	χ_{CO2} [] ×10^3	$\dot{m}_{Soot}$ [g/s] ×10^6
30	0.034	0.005	0.743	0.012
75	0.046	0.020	0.737	0.015
120	0.234	0.129	0.603	0.085
28.7*	2.030	0.220	0.535	0.751

* Steam [g/s]

Table 6 Results summary of the inferred mass flows using the IFTS versus values obtained by the MFC settings and the GC concentrations.

	GC/MFC			IFTS		
	$\dot{m}_{CH4}$ [g/s]	$\dot{m}_{CO2}$ [g/s]	η_{comb} []	$\dot{m}_{CH4}$ [g/s]	$\dot{m}_{CO2}$ [g/s]	η_{comb} []
HV	0.060	0.162	0.494	0.066	0.189	0.513
Air 120	0.028	0.075	0.50	0.030	0.187	0.70
Air 75	0.004	0.139	0.93	0.015	1.115	0.96
Air 30	0.001	0.146	0.97	2.590	8.130	0.53
Steam	0.049	0.019	0.12	0.062	0.043	0.20

Figure 36 shows spectral intensity maps at 2336 cm^{-1} and 3013 cm^{-1}, aligned with the CO_2 and CH_4 vibro-rotational bands, respectively, for a flare plume with 120 SLPM of air. The control surface is shown in red. The similarity of these results shows that the plume appears to be well-mixed at the measurement height. The relative intensity of the images shows that, as is the case for the heated vent experiments, the CH_4 emission spectrum has a significantly lower SNR compared to the CO_2 emission spectrum.

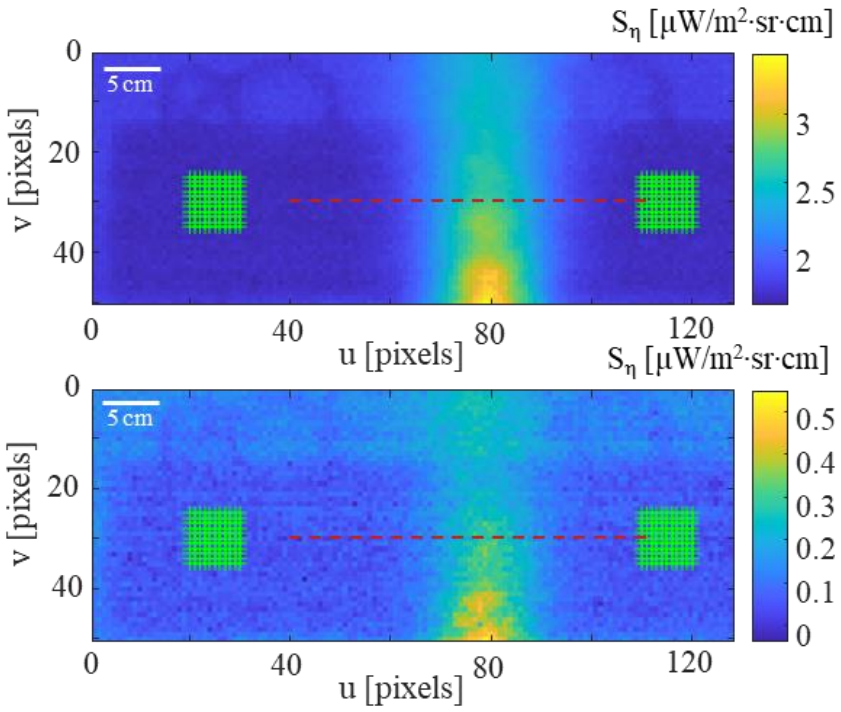

Figure 36 Spectral intensity maps of the flare plume at 2336 cm^{-1} and 3013cm^{-1} (aligned with CO_2 and CH_4 ro-vibrational bands, respectively) for the flare with 120 SLPM of air.

Spectra corresponding to the pixel locations within and outside the plume are plotted in Figure 37. In the air-assisted cases, the visible flame length increases as the airflow rate decreases. The IFTS measurement position is maintained relative to the flare nozzle, so the position of the control surface changes relative to the flame front. Methane spectral lines are apparent for the 120 SLPM air-assisted case, indicating inefficient combustion. The CH_4 emission spectrum is less pronounced at the 75 SLPM air-assisted case, while the CO_2 emission is stronger since the control surface has moved to a hotter region of the flame. In the 30 SLPM air-assisted case, the entire spectrum is uniformly shifted above the background intensity due to broadband emission from soot within the flame that would otherwise be oxidized if the measurement were carried out further downstream. For the steam-assisted case, both

H_2O and CH_4 emission lines are particularly pronounced, suggesting highly inefficient combustion in this scenario. The intensity spectra are qualitatively consistent with the expected trends in CE and GC concentration measurements in Table 6.

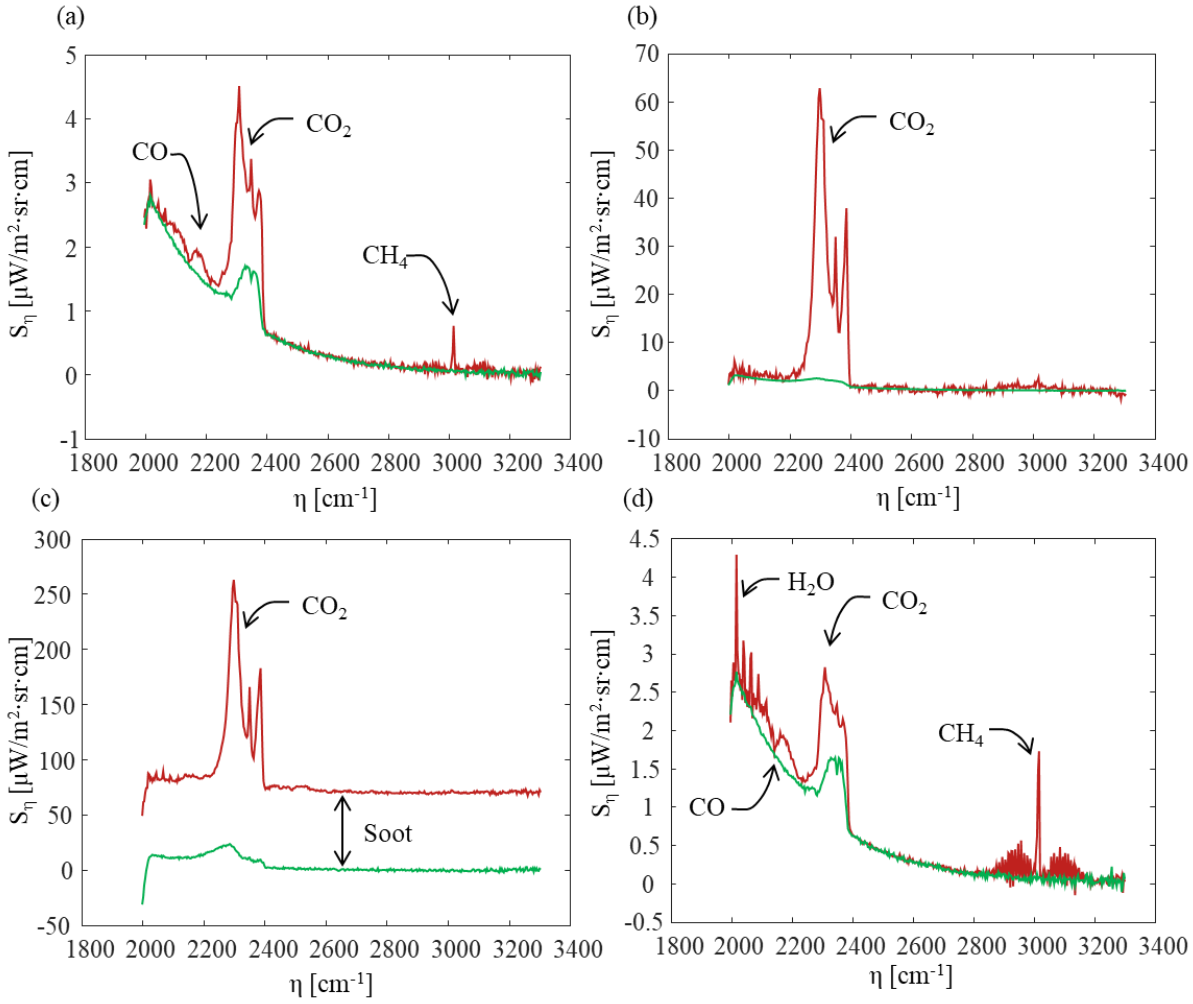

Figure 37 Intensity spectra for assisted flares: (a) 120 SLPM air; (b) 75 SLPM air; (c) 30 SLPM air, and (d) 29 g/s steam. Red and green curves correspond respectively to pixel locations within and outside of the plume, at locations shown in Figure 36.

Next, the IFTS data is analyzed to obtain quantitative mass flow rate estimates and overall flare CE. Background pixels were analyzed to obtain ambient CO_2 concentration and ambient gas and background temperatures, as described in Section 5.2.1, and then incorporated into the RTE model. The peak concentrations for CO_2 and CH_4 for the 120 SLPM air-assisted case are plotted in Figure 38 (a), along with the temperature profile. Each point corresponds to the peak mass fraction inferred from the median of 50 sequential spectra.

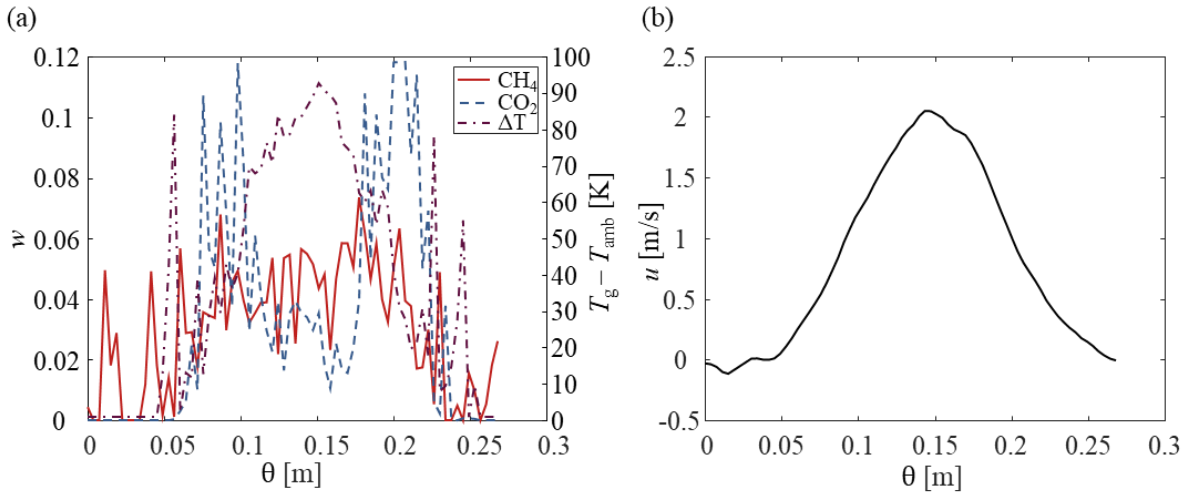

Figure 38 (a) Peak mass fractions and gas temperature, and (b) velocity profile along the control surface shown in Figure 36.

Since the gas temperature of the flare plume is higher than that of the heated vent, one may expect a lower SNR in the data, leading to a more robust estimate of the species column densities. On the contrary, Figure 38 (a) shows that the inferred peak concentrations for CH_4 are more irregular than in the heated vent case. For these measurements, the dynamic range of the camera becomes an issue. Specifically, the integration time of the camera must be decreased to avoid saturating the spectrum corresponding to CO_2 emissions, but this significantly degrades the signal-to-noise ratio over the CH_4

spectral band. In contrast to the heated plume, the CO_2 peak molar fraction does not follow a Gaussian distribution; rather, it appears to be lower in the center of the plume than at the edges. This effect may be due to the fact that air is injected through the centre tube of the burner.

The velocity profile is calculated using the same procedure described in Section 5.2.1 and is plotted in Figure 38 (b). The mass flow of each species is found by combining the column densities and velocity profile, which are shown in Table 6. The inferred CH_4 mass flow is generally close to the ground truth flow, while the CO_2 mass flow is severely over-predicted. Comparing the measured spectrum for the pixel with the highest inferred CO_2 peak concentration and the model spectra for the 120 SLPM air-assisted case provides further insight into the origins of this problem. Figure 39 shows spectral features adjacent to the CO_2 band, but do not correspond to emission spectra of any known combustion species; only the most abundant isotopologues, molecules with the same chemical formula and bonds but composed of atoms having different numbers of neutrons, were investigated. This unknown source also appears in the spectra corresponding to the 75 SLPM air-assisted case.

A possible source of the spectra anomaly can be emission from the second most abundant CO_2 isotopologue. The most abundant isotopologue in the atmosphere is $^{12}C^{16}O_2$ (98.4204%), and the second is $^{13}C^{16}O_2$ (1.1057%) [91]. The different mass of carbon isotopes ^{13}C and ^{12}C affects the rotational and vibrational energy states, changing the absorption lines. The $^{13}C^{16}O_2$ emits in the spectral region that anomalies were observed in Figure 39. Figure 40 shows the absorption coefficient for $^{12}C^{16}O_2$ with the second most abundant $^{13}C^{16}O_2$ with a tenfold ambient concentration to facilitate the observation. However, to justify the spectrum, the ratio between the second and the first CO_2 isotopologues should be higher than the naturally found in the ambient CO_2. This hypothesis could explain the data provided that the ratio $^{13}C/^{12}C$ in the fuel is higher than the ambient CO_2, or incomplete combustion reaction favours ^{13}C carbon isotopes, isotope fractionation. The CO_2 captured by photosynthesis favours the ^{12}C

isotope, so CO_2 arising from the combustion of fossil fuels, mainly formed by the remains of algae and zooplankton, has a $^{13}C/^{12}C$ slightly lower than the ambient CO_2 ratio [92]. At the same time, the fractionation effect on the incomplete combustion process favours ^{12}C isotopes [93]. Therefore, the ratio between the second and the first most abundant CO_2 isotopologue in the combustion products should be lower than the ambient ratio, indicating that $^{13}C^{16}O_2$ is not likely to be the unknown emission source.

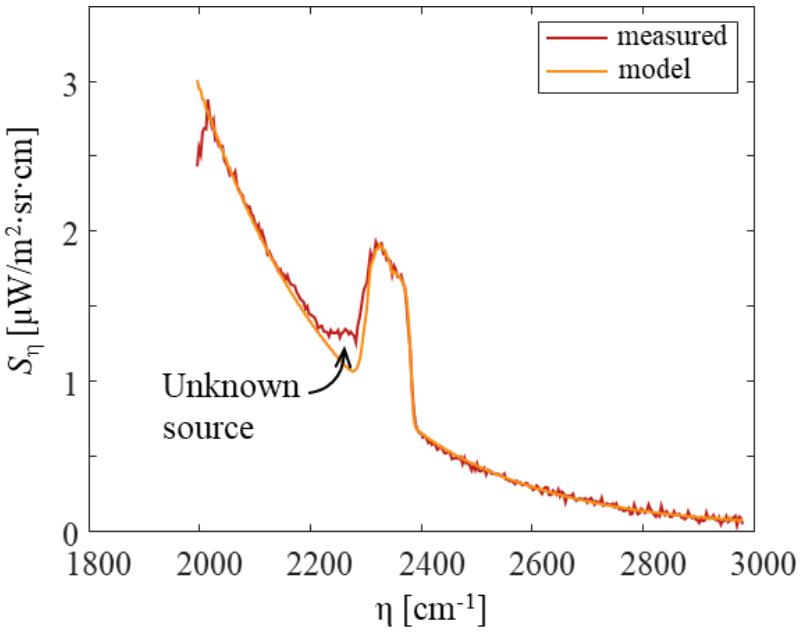

Figure 39 Measured spectral data and fitted data of the point at theta 0.21 m in 120 SLPM air-assisted case.

The situation is compounded when soot contributes to the emission spectrum, as seen in Figure 37 (c) for the 30 SLPM air-assisted case, since soot is not accounted for in the spectroscopic model. This result suggests that the measurement control surface distance from the flare may play a critical role in the feasibility of this approach, and further experimentation is needed to identify strategies that

avoid contamination of the spectrum with measurements errors and soot incandescence. However, this observation may also suggest the possibility that soot emission may also be quantified using the IFTS.

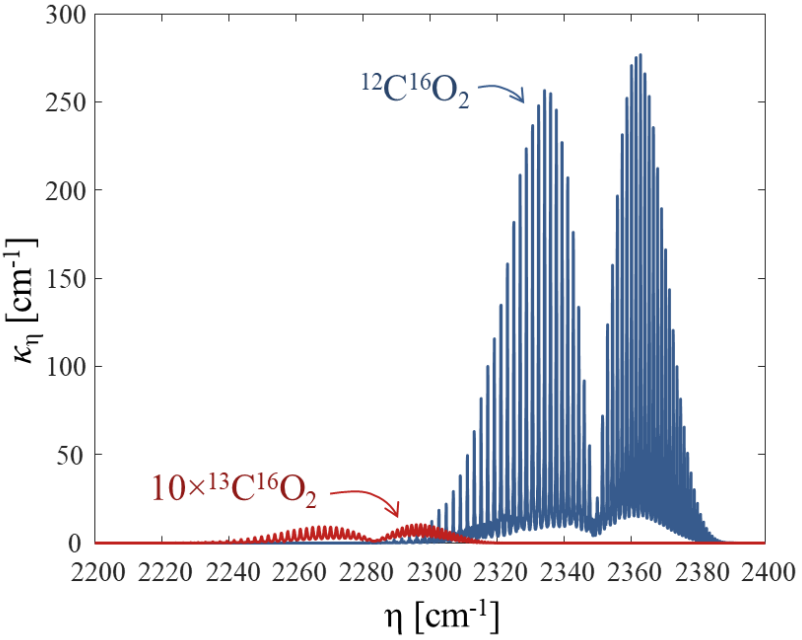

Figure 40 Most abundant CO_2 isotopologue absorption coefficient at 300 K in blue compared to tenfold the ambient ratio of the CO_2 second most abundant isotopologue absorption coefficient.

In a real flare measurement, the influence of soot may be mitigated by choosing the control surface to be farther from the flame. Additionally, the greater contrast between the background and the plume should facilitate the inference. On the other hand, the emission from ambient species between the camera and the flare plume would need to be considered because of the long path length.

5.3 Conclusions

MWIR hyperspectral imaging presents an opportunity to quantify the combustion efficiency of operating flares through remote, stand-off measurements. This chapter summarized a proof-of-concept study for this approach through numerical and experimental analysis. Simulated measurements were carried out on a CFD-LES of a flare in a cross-flow. Intensities generated using the radiative transfer equation were transformed into intensity spectra, which in turn were inverted to recover distributions of temperature, CO_2, and CH_4 volume fractions along various LOS, which are presumed to be Gaussian. These distributions were transformed into column densities and used to define pixel CEs along a control surface. The inferred distributions are, in some cases, significantly different from the CFD simulations, highlighting the ill-posed nature of this inverse problem. However, the recovered CEs are much closer to the ground truth.

The approach was then experimentally assessed using a heated vent of CH_4 and CO_2, and a laboratory-scale air- or steam-assisted flare. In the case of the heated vent experiment, the mass flow rates inferred from the hyperspectral data closely matched known flow rates. In addition, this experiment highlights how hyperspectral data can be used to obtain background intensity and ambient gas concentrations outside of the plume, parameters that feature in the spectroscopic model. In the case of the lab-scale flare, the intensity spectra are qualitatively consistent with the expected trends in CE. The IFTS-inferred CH_4 mass flow rates were close to values inferred from the known flow rates of the reactants and gas chromatography measurements on the combustion products. On the other hand, CO_2 mass flow is significantly over-predicted, likely due to unexplained features in the spectral data.

Overall, the results establish the viability of hyperspectral imaging to quantify flare CE and highlight the challenges of this approach and the need for further experimentation to develop best

practices to avoid adverse measurement conditions. However, the possibility exists to improve the robustness of the CE estimate, by incorporating additional information into the inference procedure. The CFD distribution shapes for temperature and CO_2 in particular, Figure 30, are generally similar as combustion reaction releases CO_2 and locally increases the gas temperature, implying valuable information about CO_2 concentration in the gas temperature.

Chapter 6

Enhancing Optical Quantification of Combustion Products using Thermochemical Manifold Reduction

Optical diagnostics are useful to measure gas emissions since large flow field areas may be imaged instantaneously, and, in some cases, gas concentrations and temperatures may be reconstructed along each LOS. However, in addition to spatial and temporal resolution, some degree of spectral resolution is needed to resolve concentrations of multiple species simultaneously. Obtaining concentration distribution of combustion products from spectroscopic data is often challenging due to the large number of variables involved and the indirect relationship between the measured spectra and the unknown quantities. Combined, these effects often make the inference problem mathematically ill-posed and computationally-demanding to solve. Particularly in the case of emission-based spectroscopy, for a mixture containing n radiatively-participating species, at least n+1 images must be obtained at independent wavenumbers or over distinct spectral bands to estimate species concentrations and temperature, assuming that the plume is well-mixed. Due to the inherent ill-posedness of the problem, and in scenarios involving heterogeneous species concentrations and temperatures, it may be necessary to have an even higher degree of spectral resolution to obtain robust estimates of the quantities-of-interest.

In this regard, hyperspectral imaging using IFTSs is particularly appealing. Each pixel in an image corresponds to a high-resolution spectrum, from which the species column densities and temperature may be inferred simultaneously by regressing a model spectrum derived from the radiative transfer equation to the measurements [43,66,77]. On the other hand, a major drawback of the IFTS is

its poor temporal resolution compared to other types of sensors. Higher spectral resolutions require more images, which increases the acquisition time; typical acquisition times may be on the order of 30 s in order to achieve a spectral resolution of 0.25 cm^{-1}. This long acquisition time is not an issue for stationary targets, but, in the case of turbulent flow fields, changes in the gas state can generate artifacts in the recovered spectra [62]. For this reason, it is desirable to use the lowest resolution necessary to infer the temperature and volume fraction of each species. However, lowering the spectral resolution may increase the ill-posedness of the problem.

Multispectral cameras offer a faster and significantly less costly alternative to IFTSs. However, this temporal resolution is achieved at the expense of a much lower spectral resolution, typically 4-8 near-simultaneous broadband filtered images, versus thousands of images generated by the IFTS. Even when using an optimized set of filters, as discussed in Chapter 4, the limited spectral resolution afforded by broadband multispectral cameras may render this inverse problem too ill-posed to solve.

This chapter examines the possibility of ameliorating this ill-posedness by introducing additional prior information via a thermochemical manifold reduction (TCMR) model. This procedure is implemented on synthetic MS and IFTS measurements on a flare in a crosswind to infer the combustion efficiency. The results and procedure presented in this chapter were disseminated in Ref. [94][10].

6.1 Thermochemical Manifold Reduction

Thermochemical manifold reduction or flamelet generated manifolds are widely used in numerical simulations to reduce the number of transported variables [95]. This approach is transferred to the

[10] This paper is coauthored by Johannes Emmert who helped in the creation of the concept, and methodology; Kyle J. Daun helped in the creation of the concept, supervision, review, project administration, supervision, and funding acquisition.

inversion problem, reducing the number of variables and the ill-posedness of the problem. In many cases, the MS or IFTS measurement focuses not on the reaction zone of the combustion process itself but rather on the downstream combustion products, allowing for a significant simplification of the thermochemical manifold compared to methods used in simulations. For example, when determining flame CE or gas turbine emissions, measurements are carried out downstream of the flame, and intermediate combustion species are not considered.

Gas concentrations and temperatures in the combustion products are strongly correlated via combustion reactions. Unburned fuel and CO_2 concentrations can be expected to be anti-correlated, while the CO_2 is expected to have a higher temperature compared to the unburned fuel due to the enthalpy of combustion. On the other hand, dilution by air entrainment will lower the temperature of the combustion products. Incorporating this information into the inference procedure should improve the accuracy of the recovered gas state and decrease the computational cost. Therefore, the species in the zone of interest are approximated as a mixture of three states: (i) combustion products, (ii) unburned fuel, and (iii) air. Although only these three states are assumed in this application, the procedure can be adapted to more states with targeted species.

The enthalpy values for each of the three states are calculated from standard mixing rules. The enthalpy of the combustion products is augmented by adding the lower heating value (LHV) to the mixture enthalpy, using a factor to account for radiant losses. Therefore, the temperature distribution over the LOS pixel can be approximated using the mixing enthalpy of the three possible states. Consider the simplest case of complete CH_4 combustion, which is important for flaring from upstream oil and gas operations. Equation (2.1) can be written for CH_4/air combustion,

$$CH_4 + 2\left(O_2 + 3.76N_2\right) \rightarrow CO_2 + 2H_2O + 7.52N_2 . \tag{6.1}$$

The complete manifold is defined by the mole fractions of CH_4, CO_2, H_2O, O_2, N_2, and the molar absolute enthalpy of the mixture,

$$\beta_i = [X_{CH4}, X_{CO2}, X_{H2O}, X_{O2}, X_{N2}, h_i]. \tag{6.2}$$

The gas state at any point of the combustion products can be approximated by a linear combination of the three pure state vectors given by

$$[X_{CH4}, X_{CO2}, X_{H2O}, X_{O2}, X_{N2}, h_i] = x_1(\beta_1 - \beta_3) + x_2(\beta_2 - \beta_3) + \beta_3, \tag{6.3}$$

where variables x_1 and x_2 denote combustion products and unburned fuel fractions, respectively, while the residual $(1-x_1-x_2)$ is the dilution with air. States β_1, β_2, and β_3 are the combustion products, unburned fuel, and air, respectively, given by

$$\begin{bmatrix} \beta_1 \\ \beta_2 \\ \beta_3 \end{bmatrix} = \begin{bmatrix} 0 & \frac{1}{10.52} & \frac{2}{10.52} & 0 & \frac{7.52}{10.52} & \frac{1}{10.52}(1 - X_R)h_{LHV} \\ 1 & 0 & 0 & 0 & 0 & h_{2,AMB} \\ X_{CH4,AMB} & X_{CO2,AMB} & X_{H2O,AMB} & X_{O2,AMB} & X_{N2,AMB} & h_{3,AMB} \end{bmatrix} \tag{6.4}$$

where $X_{k,AMB}$ are mole fractions in ambient air, $h_{i,AMB}$ are the enthalpies of the mixtures at ambient temperature, h_{LHV} is the enthalpy of combustion per mole of fuel, and X_R accounts for radiative losses. The small contributions of ambient air, CO_2, and H_2O to the burned state are treated in the code, but neglected in these equations to reduce complexity and more clearly present the concept.

Accordingly, the gas state can be expressed completely via a ternary plot like the one in Figure 41, which shows the adiabatic temperature predicted by the TCMR model. Consequently, the spectral absorption coefficient and the spectral intensity incident on the detector depend only on x_1 and x_2. It is possible to precompute the mixture absorption coefficient for all valid combinations of x_1 and x_2, thereby reducing the computational cost.

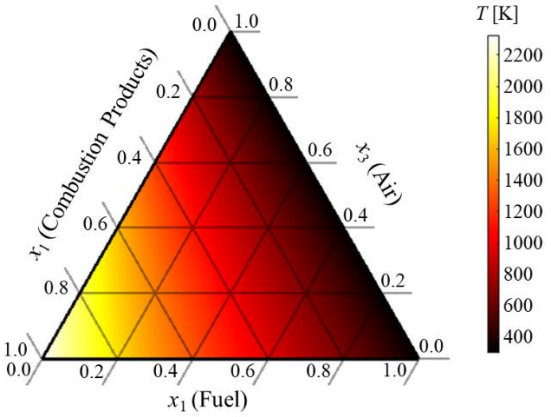

Figure 41 States mixture adiabatic temperature predicted by TCMR.

The distribution of these two gases along the LOS are modelled as Gaussian

$$x_i(s) = x_{i,\max} \exp\left(-\frac{s^2}{2\sigma^2}\right), \tag{6.5}$$

where $x_{i,\max}$ is the variable peak value, and σ is the plume width parameter. The values are inferred from the MLE of Eq. (3.27) with the state vector being $\mathbf{x} = [x_{1,\max}, x_{2,\max}]^T$ for fixed X_R, and $\mathbf{x} = [x_{1,\max}, x_{2,\max}, X_R]^T$ for simultaneously-inferred X_R. The limited model dimensionality also allows pre-computation of the IFTS signals as a function of $x_{1,\max}$ and $x_{2,\max}$.

The information incorporated into the inference process via the TCMR also reduces the ill-posedness of the problem; for example, the implied relationship between H_2O and CO_2 concentrations means that radiative emission from hot H_2O lines can inform the CO_2 volume fraction. Although this work focuses on CH_4 combustion, the benefits presented by the TCMR are higher when considering multicomponent fuels, which would otherwise require a large number of variables to represent combustion emissions.

6.2 Synthetic Data

The feasibility of the TCMR approach is assessed by considering a synthetic experiment of inferring the CE of an upstream oil and gas flare using an IFTS or an MS camera. The procedure to generate the synthetic data is described in Section 4.4.1. These CFD results were used to generate synthetic MWIR images according to the measurement model defined in 3.1. As this study uses a higher IFTS spectral resolution, a lookup table was precomputed for each species with a spectral resolution of 0.025 cm^{-1} using Voigt profile to generate the spectral lines.

The spectral intensity is processed to generate the synthetic data using Eq. (3.17) for the IFTS and Eq. (3.14) for the MS camera. The IFTS parameters correspond to a Telops MWIR Hyper-cam with a spectral range from 2000 to 3333 cm^{-1} (3-5 μm). The IFTS may be adjusted to optimize the trade-off between spectral and temporal resolution; this work considers spectral resolutions of 0.25, 1, 4, 16, and 64 cm^{-1}. The multispectral camera parameters correspond to those of a Telops multispectral MWIR camera. The set of filters used in this case, shown in Table 3, are optimized to measure the CE of flares following the procedure defined in Chapter 4. The filters were modelled as boxcar functions with a transmittance equal to the specified peak transmittance.

6.3 Results

The synthetic data of 24 pixels, shown in Figure 42 with the CO_2 volume fraction contour map, were sampled and contaminated with 10% white noise for a set of 128 measurements each, totalizing 3072 samples for each chosen spectral resolution. The MS camera data was contaminated with white noise using Eq. (3.15) equivalent to a temperature difference (NETD) of 25 mK. The CO_2, CH_4, and H_2O column densities are estimated for each sample in terms of their respective maximum values ($x_{1,max}$, $x_{2,max}$). In the case of the IFTS, column densities are found using three different procedures and five

spectral resolutions. First, the peak volume fraction of each species and peak temperature is inferred simultaneously, assuming that they obey Gaussian distributions having the form of Eq. (3.26); this is henceforth called the full manifold (FM) procedure. Next, the TCMR is used to estimate $x_{1,max}$ and $x_{2,max}$. In order to account for radiation losses in the flame from soot and participating gases, the LHV added to the enthalpy of the combustion products is reduced by the radiant fraction term, X_R, which is treated as an additional parameter to be inferred ($\mathbf{x} = [x_{1,max}, x_{2,max}, X_R]^T$). Finally, the radiant fraction was set fixed to simulate the use of the camera as a radiometer to measure the radiant fraction using the single point source model [96]. In all the above treatments, σ was set equal to 30 cm based on the projection shown in Figure 42 (a).

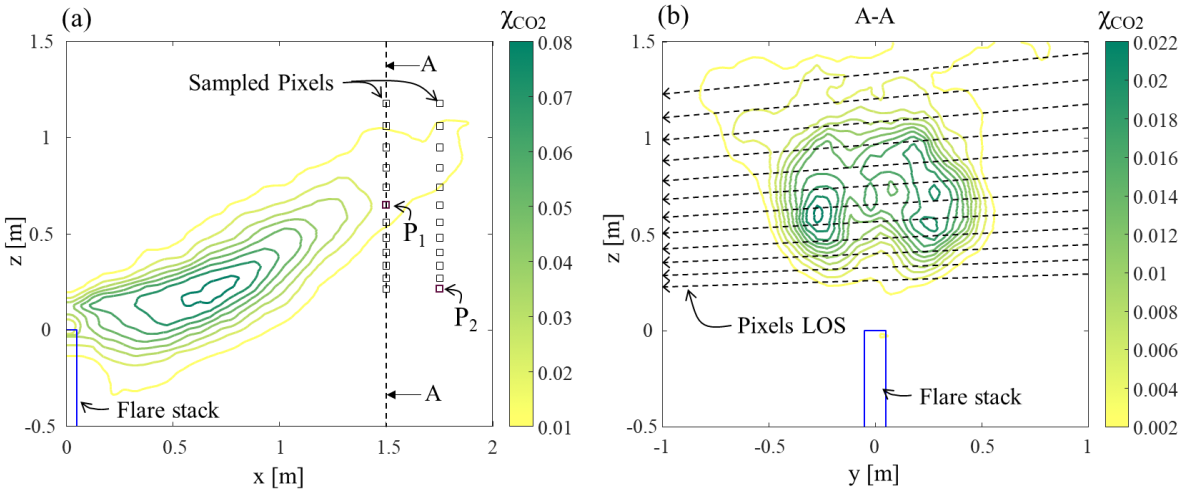

Figure 42 Simulation CO_2 volume fraction contour maps with sampled pixels, (a) center plane (y=0 m) and (b) plane at x=1.5 m, plane A-A.

Figure 43 shows the CO_2 column number densities estimated using the three approaches for the 4 cm^{-1} resolution IFTS. The black line shows the CFD ground truth; in other words, exact estimations of column densities would land on the line. The abscissa and ordinate axes correspond to

the CFD CO_2 column density and the spectrally-inferred CO_2 column density. Purple points show column densities found by fitting the entire spectrum using the incident spectral intensity, $I_{\eta L}$, before accounting for the ILS via Eq. (3.17) and without using the TCMR. Even with this high-resolution data (HRD) and neglecting instrument effects, the Gaussian profile assumption leads to significant errors in the recovered column densities.

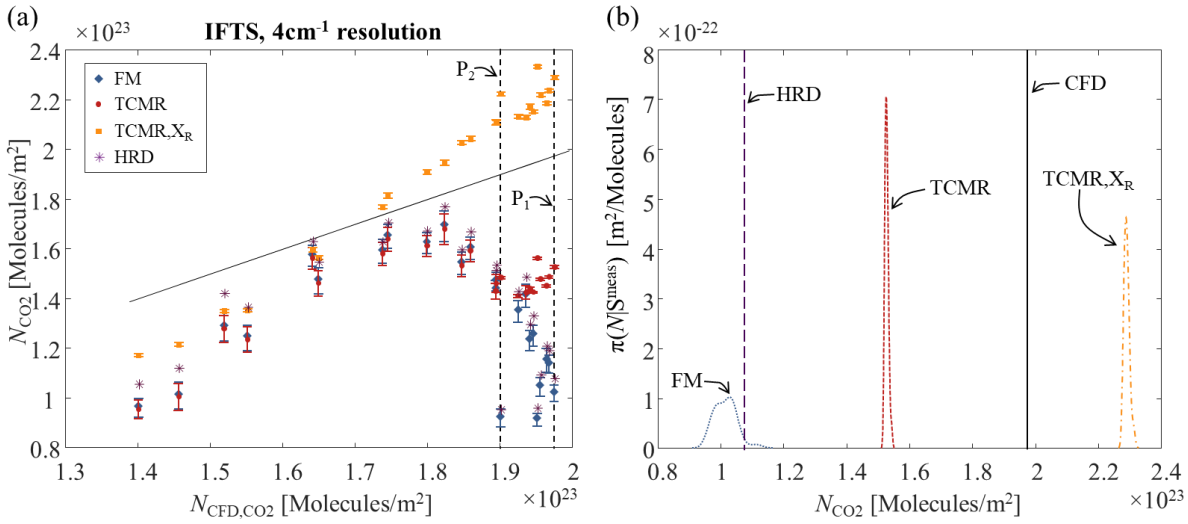

Figure 43 Estimated column number densities using spectral data with 4 cm^{-1} resolution, (a) for the 24 sampled pixels. Data points represent the average of the samples, and error bars one standard deviation between the results for each sampled pixel, and (b) pixel P_1 column number density pdf. Curves denote full manifold fitting (FM), TCMR fitting the radiant fraction (TCMR), TCMR with known radiant fraction (TCMR, X_R), and high-resolution data (HRD).

The column densities recovered using the FM approach and the transformed IFTS data (blue diamonds) are close to the parameters found using $I_{\eta L}$. The similarity between these results shows that changing the resolution, downsampling from the HRD to instrument spectral resolution, and accounting for the instrument effects on the data do not significantly impact the model error. Incorporating the

TCMR approach with an unknown X_R (red dots) improves pixels corresponding to larger column densities. On the other hand, the column number inferences improve significantly when the radiant fraction is estimated radiometrically (orange squares), assumed as 0.32 from a pixel fitted using the second approach.

The results can also be envisioned as probability density functions (pdfs) as shown in Figure 43 (b) for pixel P_1, as indicated in Figure 42, which corresponds to the largest difference between the ground truth and inferred CO_2 column number densities. The FM results are close to the HRD case, indicating that the LOS profile approximation causes the error. However, both approaches using the TCMR are more accurate than the FM results. The TCMR-pdfs results are also narrower than the FM results. With fewer unknown parameters, the TCMR inverse problem is far less ill-posed than the FM approach, and, consequently, the random measurement noise $\boldsymbol{\delta S}^{meas}$ is amplified to a much lesser extent.

The error can be further investigated by comparing the inferred CO_2 volume fraction and gas temperature distributions along the LOS with the CFD ground truth for pixel P_1, Figure 44 (a) and (b), respectively. The ground-truth CFD volume fraction profile does not follow a Gaussian distribution, although the temperature peak found using the FM is close to the ground truth. The spectral intensity is more sensitive to temperature than volume fractions due to the blackbody term in the RTE, Eq. (3.11) . Because the ground truth CFD temperature and volume fraction profiles decay faster away from the plume centerline compared to the Gaussian curves, the reabsorption term in the RTE is less important, and consequently, a profile having a higher temperature and a more gradual drop in temperature and volume fraction will produce very similar spectral intensities in the case of non-optically-thin lines. On the other hand, changing the species volume fraction will impact optically-thin and optically-thick lines differently. The spectral intensities corresponding to optically-thin lines increase with volume fraction due to the enhanced emission term. In contrast, spectral intensities

corresponding to thicker lines decrease by the increase of the reabsorption term. As the spectral intensity is more sensitive to temperature, a small over-prediction on the estimated temperature causes a large under-prediction on the estimated volume fraction.

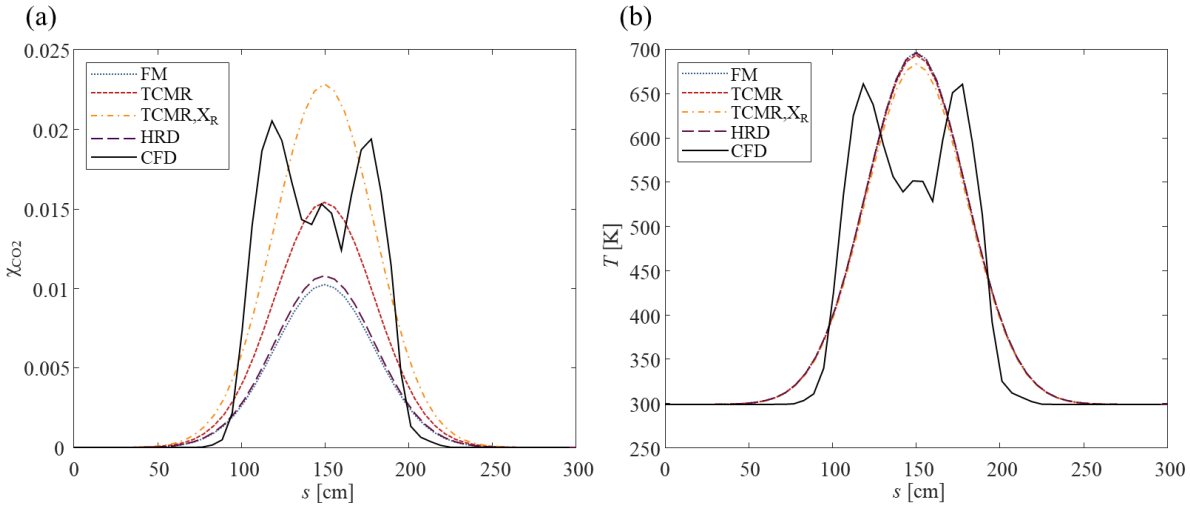

Figure 44 CFD and estimated parameter profile along the LOS: (a) CO_2 volume fraction and (b) gas temperature. Curves denote full manifold (FM); TCMR fitting the radiant fraction (TCMR); TCMR with known radiant fraction (TCMR,X_R); and high-resolution data (HRD).

In the first TCMR approach, in which the radiant fraction is inferred along with x_1 and x_2, the H_2O spectra provide information for inferring the temperature and the CO_2 volume fraction by fixing the ratio between combustion products. Although the inferred temperature is close to the FM results, it is slightly lower than the FM, leading to a more accurate volume fraction. Measuring the radiant fraction radiometrically and treating it as a fixed parameter amounts to fixing the ratio between the temperature, CO_2, and H_2O volume fraction. In this case, in addition to the H_2O spectra, the radiometrically-inferred temperature provides information about the CO_2 column number densities. However, the temperature

is still over-predicted for the same reasons, and the volume fraction is also over-predicted since the TCMR explicitly couples these variables.

Considering the inferred CH_4 column number densities, as shown in Figure 45. While the inferred CH_4 column number densities are reasonably accurate for smaller values, they significantly under-predict the ground truth for larger values. The error is caused by assuming the same Gaussian profile for both the CH_4 volume fraction and temperature; on the contrary, regions with a higher concentration of CH_4 will correspond to lower temperatures, since they indicate that the corresponding gas packets did not completely combust upstream of the measurement. An over-prediction of the temperature leads to an under-prediction of the CH_4 volume fraction. Figure 46 (a) and (b) show the CH_4 volume fraction and temperature distribution along the LOS. Note that, as expected, regions of high CH_4 correspond with lower temperatures. Another observation is that the pixel with the highest amount of CH_4 in the CFD results has a volume fraction peak of only 0.25%, much smaller than the CO_2 concentration. The combination of CH_4 low concentrations, weaker spectral lines, and ro-vibrational band with lower gain caused by the blackbody term on the RTE, makes CH_4 harder to infer compared to CO_2.

The estimated CO_2 column number densities using the MS camera are shown in Figure 47. For one pixel, the inferred CO_2 column density was overestimated by more than 300% using the FM (blue diamonds) and is excluded from the figure. Incorporating the TCMR (red dots) reduced the difference between the ground truth and inferred CO_2 column number densities compared to the FM approach, but the column number densities are biased low. On the other hand, the column densities are over-predicted using the TCMR with known radiant fraction (orange squares).

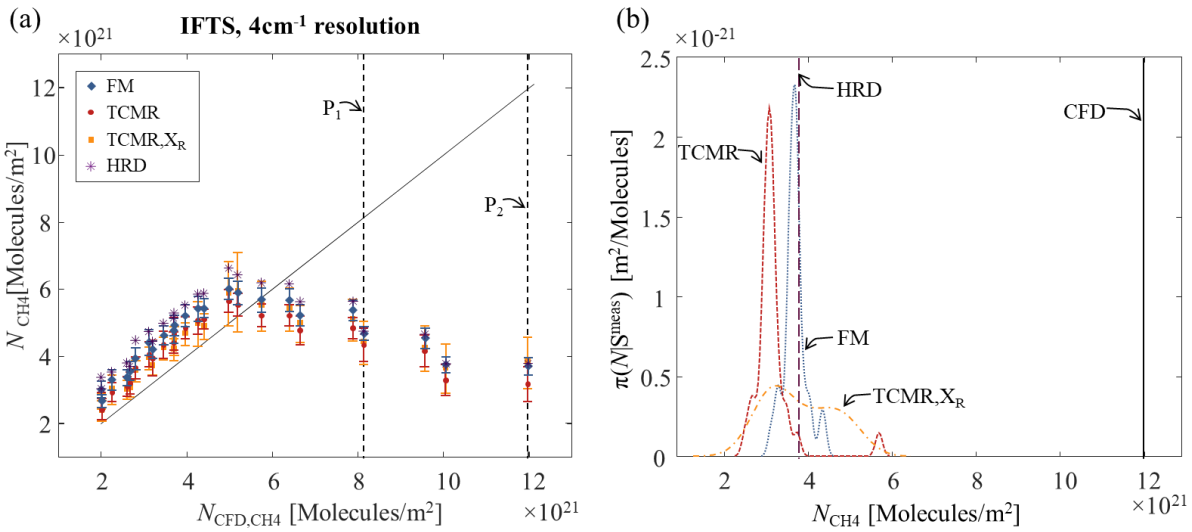

Figure 45 Estimated CH_4 column number estimated for spectral data with 4 cm^{-1} resolution: (a) for the 24 sampled pixels. Data points represent the average of the samples, and error bars one standard deviation between the results for each sampled pixel; (b) pixel P_2 column number pdf. Curves denote full manifold (FM); TCMR fitting the radiant fraction (TCMR); TCMR with known radiant fraction (TCMR, X_R); and high-resolution data (HRD).

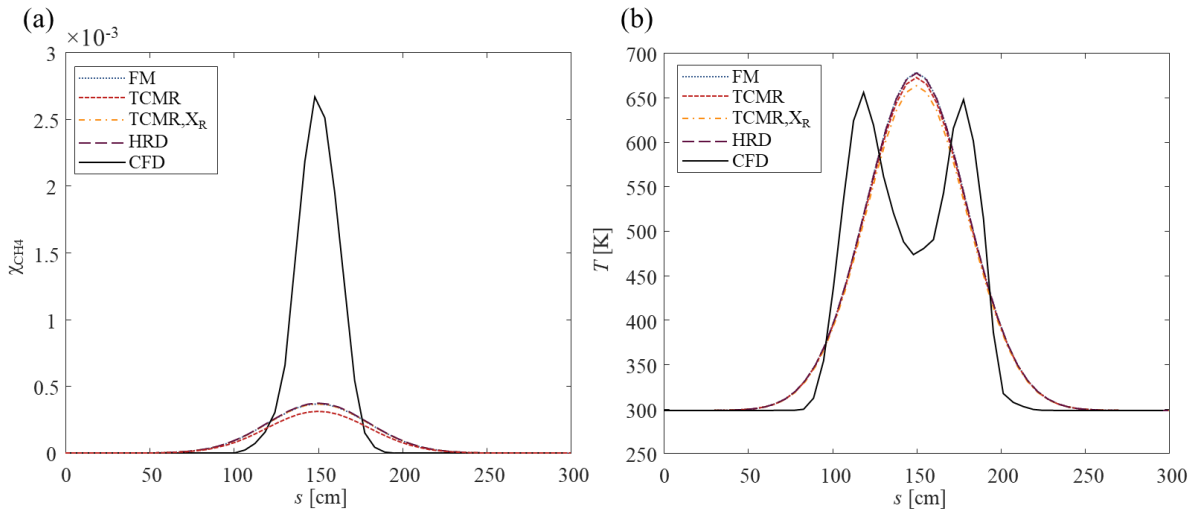

Figure 46 CFD and estimated parameter profile along the LOS: (a) CH_4 volume fraction; and (b) temperature. Curves denote full manifold (FM); TCMR fitting the radiant fraction (TCMR); TCMR with known radiant fraction (TCMR, X_R); and high-resolution data (HRD).

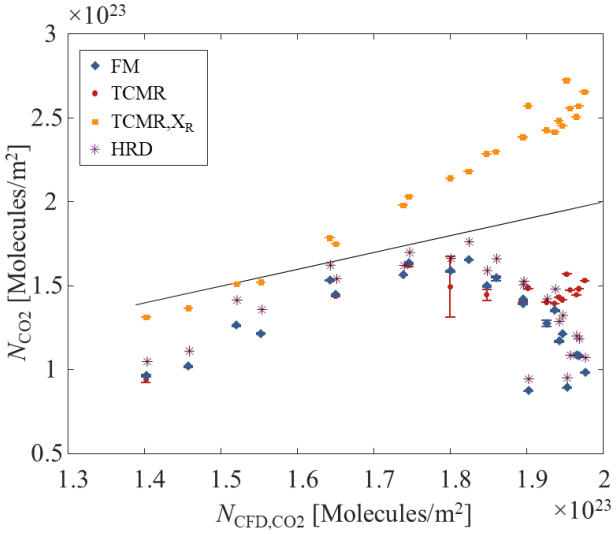

Figure 47 Estimated CO_2 column number densities using the multispectral camera. Data points are the averaged values and error bars one standard deviation to full manifold (FM); TCMR fitting the radiant fraction (TCMR); TCMR with known radiant fraction (TCMR, X_R); and high-resolution data (HRD).

Figure 48 shows the RMS error of the CO_2 column number density estimates for all sampled pixels for the different IFTS spectral resolutions and the MS camera for the three tested methods. The RMS error decreases as information is added via the TCMR and radiant fraction. Unexpectedly, however, increasing the spectral resolution of the IFTS does not improve the results. Because the measurements are more sensitive to temperature, the temperature is "easier" to infer, even using few spectral bins. However, the absorption coefficient is almost linear in relation to volume fraction, so the spectral bins are not independent and adding more spectral bins does not add information to the problem.

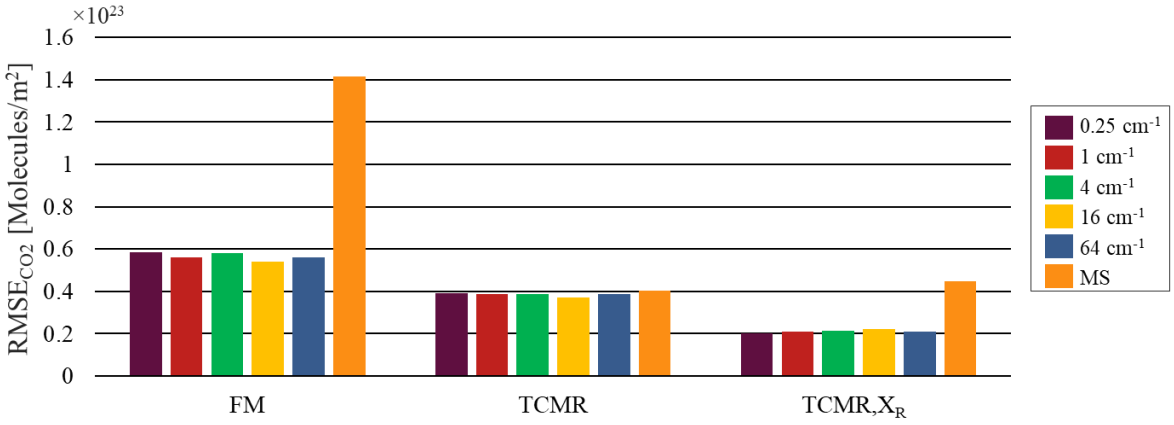

Figure 48 CO_2 column number densities estimate RMS error for different IFTS spectral resolutions and multispectral (MS) camera using the full manifold (FM), TCMR fitting the radiant fraction (TCMR), and TCMR with known radiant fraction (TCMR, X_R).

Figure 49 shows the CH_4 column number density RMS error in logarithmic scale for the same samples. Although the optimal filter set has six of the eight filters in the CH_4 region, the column densities inferred using the MS camera are far less accurate than those obtained using the IFTS. As expected, the TCMR did not improve the CH_4 estimates using the IFTS for any spectral resolution, as it does not add valuable information to the fuel state. On the other hand, the TCMR significantly improves the CH_4 column densities inferred using the MS data. This improvement is mainly due to the fact that the TCMR suppresses outliers. When these outliers are excluded, the errors obtained with and without the TCMR are similar.

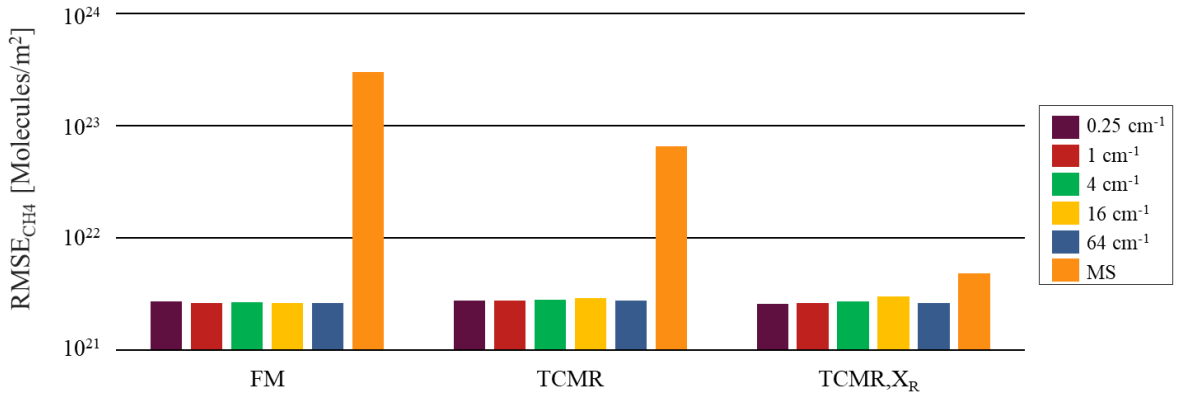

Figure 49 CH_4 column number densities estimate RMS error for different IFTS spectral resolutions and multispectral camera using the full manifold (FM), TCMR fitting the radiant fraction (TCMR), and TCMR with known radiant fraction (TCMR, X_R).

6.4 Conclusions

However, simultaneous inference of species concentrations and temperature from HS and MS images is challenging because the inversion of the measurement equations is often mathematically ill-posed. This chapter describes a novel approach to mitigate this problem by incorporating additional information via a thermochemical reduction mechanism, thereby reducing the number of inferred parameters and the statistical degrees-of-freedom in the inversion problem. The model is tested using a simulated CH_4 flare in a crosswind using three different strategies and five different camera resolutions in the case of the IFTS. The estimated values were converted to the species column number and compared to the CFD data.

Incorporating the TCMR and fitting the radiant fraction improved the CO_2 column number accuracy and precision for all wavenumber resolutions in relation to the standard approach; the improvement was most pronounced for pixels corresponding to large column number densities. An even more significant improvement is obtained by imposing a radiant fraction. The CO_2 column

densities estimated using the IFTS data are more accurate than values found using the multispectral data, even when considering that the signal-to-noise ratio of the multispectral data is higher than that of the IFTS data. However, CO_2 estimates inferred using the multispectral camera are most improved by the TCMR compared to those obtained assuming a full manifold.

On the other hand, the TCMR result does not significantly improve estimates for the unburned fuel state. The combination of weaker spectral lines, lower concentrations, and the fact that the CH_4 spectral band corresponds to lower blackbody intensities make CH_4 concentrations much harder to quantify compared to CO_2 concentrations. The brightness difference between CO_2 and CH_4 emissions is particularly challenging when detecting CO_2 and CH_4 simultaneously, since the camera's integration time must be adjusted to accommodate the CO_2 emission, especially at high gas temperatures. Nevertheless, the biggest cause of inference error is the assumption of Gaussian profile along the LOS. While the information added by the TCMR can somewhat mitigate the effects of the model error, significant improvements in the recovered accuracy of CO_2 and CH_4 column densities will require a more sophisticated measurement model.

Chapter 7

Conclusions and Future Work

Optical gas imaging is a powerful tool for measuring gaseous emissions. This thesis explores how this technology may be used to estimate flare CE. Additionally, the thesis presents techniques that can improve the robustness of QOGI-inferred CE through optimal filter selection, and adding combustion information to the inference process.

7.1 Summary and Key Findings

If flares are assumed to have a combustion efficiency of 98%, they would be responsible for 0.9% of global anthropogenic CO_2 emissions. However, the environmental impact of flares may be much higher due to real-world effects like crosswinds and air and steam assisted flaring. Accordingly, there is an urgent need for optical techniques that can make stand-off measurements of flare combustion efficiency in order to better understand this problem.

Flare combustion efficiency is inferred using MS or HS cameras, by combining column density measurements found from a spectroscopic model, with projected velocities solved using an optical flow algorithm. Both procedures require solving mathematically ill-posed problems. In the case of the column density, the inference procedure is ill-posed due to convolutions in the spectral and spatial dimensions; consequently, several concentration distributions along the LOS can generate the same data with different column densities. Furthermore, different species emitting in the same spectral band can generate the same data with different column densities. As the volume fraction affects the

absorption coefficient linearly, it is impossible to infer volume fraction distribution along the LOS without additional information. Therefore, the profile is parametrized as a Gaussian profile.

In the case of MS cameras, obtaining robust estimates of CO_2 and CH_4 volume fractions relies on using a suitable set of filters. Chapter 4 presents a procedure for optimizing the filter set for CE measurement based on error propagation. The assumptions of unbiased error distribution and linearization allow for an efficient algorithm. The best set of filters found by the optimization were not obvious, but made intuitive sense: most filters were located at one end of the CH_4 spectral band to increase the SNR to infer CH_4 volume fraction and temperature. The best filter sets focus on specific spectral features that are sensitive to changes in each parameter independently, with a higher weight on parameters that most affect the CE.

IFTS cameras have a much high spectral resolution compared to MS cameras. Chapter 5 evaluates using an MWIR IFTS to measure flare CE through numerical and experimental analysis. First, CFD data is used to generate synthetic camera data. This data was used to recover the column densities, allowing the comparison between the recovered parameters distribution along the LOS and column densities against the ground-truth data. The CFD instantaneous species volume fraction and temperature distribution along the LOS do not follow a Gaussian profile like the parametrized one in some cases. However, the estimated local CE was similar to the CFD ground truth.

The IFTS was then used to characterize a heated vent of CH_4 and CO_2 in nitrogen, produced with mass flow controllers and a heated line. The mass flow rates inferred from the IFTS were close to mass flow controller settings. An additional experiment was done using a lab-scale air- and steam-assisted flare. Although the IFTS data is qualitatively consistent with the expected flare emissions, the

CO_2 mass flow is significantly over-predicted. Unexplained features in the measurement spectrum likely cause the errors; thus, more experiments are needed to identify the error sources.

On the other hand, temperature is the easiest parameter to infer due to the blackbody emission term on the RTE, Eq. (3.11). Although temperature results do not influence CE computation significantly, the temperature can be used to obtain information about the combustion process and, consequently, CO_2 concentrations. Chapter 6 presents a novel approach using the TCMR mechanism to incorporate additional information about the combustion process into the inference procedure, thereby reducing the ill-posedness of the problem. The TCMR improved the CO_2 column number inference for all tested resolutions, including MS data, in relation to the traditional approach. Pixels corresponding to large column densities, with more effect on the CE estimates, benefited most from the TCMR. In addition, inferring the radiant fraction a priori, possibly using the camera as a radiometer, improved the accuracy of the results. However, as expected, the TCMR does not improve the unburned fuel state. Additionally, the information added by the TCMR mitigated the error caused by the Gaussian profile approximation along the LOS.

7.2 Ongoing and Future Work

This research has also identified several knowledge gaps, as well as emerging research opportunities for improved flare emission measurements. First, it is necessary to identify and mitigate the sources of spectral anomalies in the IFTS measurements of flare plume, in order to improve the accuracy of the inferred CO_2 column densities. Second, a more comprehensive analysis needs to be done on the velocimetry inference. Finally, the TCMR method can be used to infer the nonuniform state distribution along the LOS.

7.2.1 Spectral Anomalies

Additional experiments can to be done to infer the error sources. A new CFD data with a higher temporal resolution with 120 timesteps totalizing 9.6 s are available for numerical tests. For reference, the hypercubes from the lab-scale flare used in Chapter 5 take between 6 to 9 s to acquire the 4740 frames needed to build the interferogram to generate the data cube. The CFD results can be used to generate synthetic interferograms using Eq. (3.16), and then generate synthetic IFTS by applying the inverse Fourier transform. Extending the timescale of interest will permit study of scene change artifacts, one of the leading factors that impairs the accuracy of IFTS-inferred column densities.

Another source of error that needs to be investigated is the effects of IFTS calibration conditions. The IFTS uses two black bodies at different temperatures to calibrate the data. As the effect of temperature on the IFTS raw signal is nonlinear, the data will be more precise for plume temperatures that are close to the blackbody temperatures. Figure 50 shows the raw blackbody measurements at three different temperatures for two different integration times, 100 and 1200 μs. A line is plotted in each case to simulate the camera calibration using two different temperatures in each case; in both cases, the temperature inferred will be overpredicted. The camera blackbodies have upper and lower temperatures that are physically constrained by the available heater power and water condensation, respectively. In particular, in the cases of hot gas sources, such as combustion products or soot, or cold background as the sky, the calibration temperature can be far from the calibration black bodies, and the calibration errors can be significant.

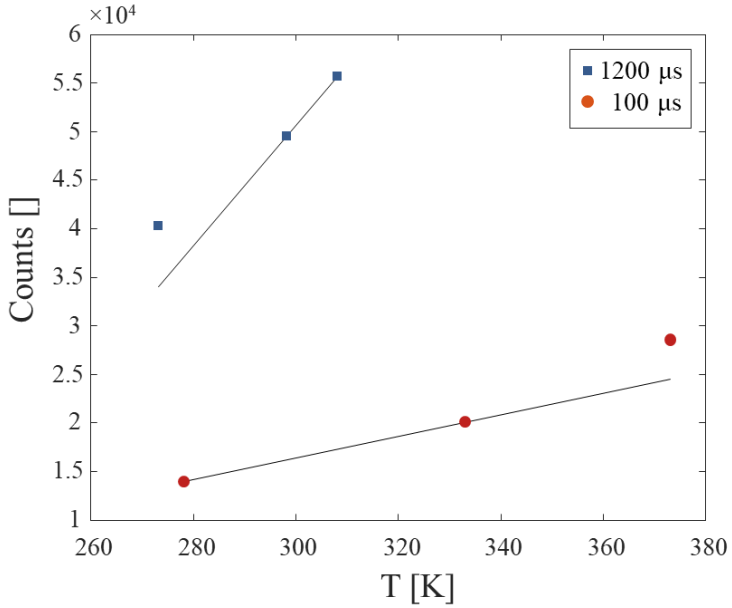

Figure 50 IFTS raw data for two integration time, blue squares 1200 µs, and red circles 100 µs. The data is for three different built-in blackbody temperatures. Straight lines are plotted to simulate the camera calibration model.

Another possible source of error can be emission from the second most abundant isotopologue of CO_2, $^{13}C^{16}O_2$. Only the most abundant isotopologue was included in the spectral model to reduce the computational time needed to generate the absorption coefficient lookup tables. However, the second most abundant CO_2 isotopologue emits in the spectral region that anomalies were observed in Figure 39. Although the difference between the first and second most abundant isotopologue should be higher in the combustion products than in the ambient CO_2, the second isotopologue is red-shifted from the first isotopologue spectral band. Therefore, the effects of the blackbody intensity distribution in high temperatures magnify the impact of the second isotopologue. Figure 51 shows the measured emission of the lab-scale flare of pixel analyzed in Section 5.2.2, same pixels of Figure 39, with the model emission using only the most abundant and the first two most abundant CO_2 isotopologues. Although

the model spectral intensity is lower than the measured intensity, they are similar. However, the spectral band aligned with $^{13}C^{16}O_2$ spectral emission is more sensitive to temperature changes and is probably more susceptible to error caused by temperature changes during the data acquisitions.

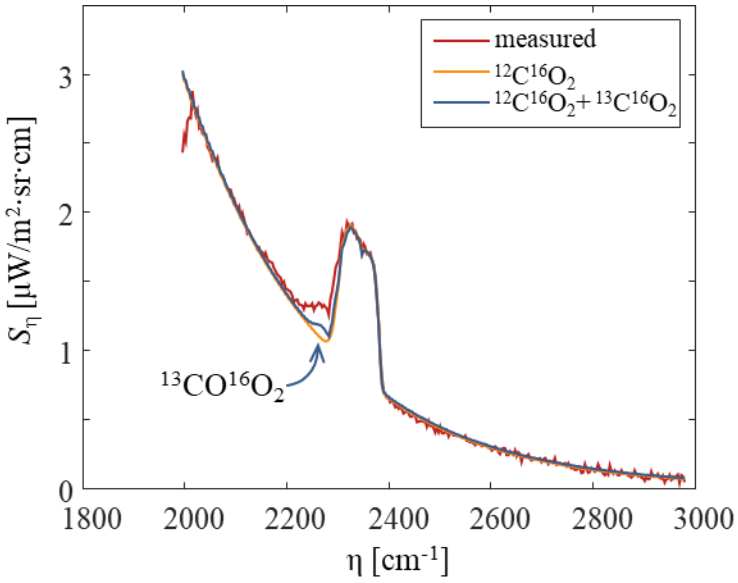

Figure 51 Measured spectral data and fitted data of the point at theta 0.21 m in 120 SLPM air-assisted case using the $^{12}C^{16}O_2$ and $^{12}C^{16}O_2$+$^{13}C^{16}O_2$ absorption coefficient.

7.2.2 Velocimetry Estimation

The work focused mainly on inferring species column densities using the RTE. However, the velocity distribution is an important component of CE estimates. The optical flow generates a two-dimensional projection of the three-dimensional flow velocity weighted by the gas radiative intensity, i.e., hotter or higher concentration gas has a heavier weight on the computed velocity. For instance, in a buoyance-dominated flow, the warmer combustion products will have a higher radiative intensity and higher

velocity; therefore, using the optical flow can overpredict the mass flows. A suggestion for future work is to measure the accuracy of the different algorithms to estimate the flow velocity. Although several studies were done to compare different optical flow algorithm results [97–99], the studies are focused on solid objects moving in the images. Additionally, the optical flow studies focused on fluid flow mainly use light scattered by particles in the flow [100,101]. The most recent survey from Mendes et al. [101] compares optical flow algorithms for measuring fluid velocity using three different algorithms: those of Horn and Schunck [68], Lucas and Kanade [102], and Farnebäck [103]. Although the study focuses on particle-based velocimetry, it observed better results using the Farnebäck algorithm combined with fluid flow information given by the Liu and Shen technique [104]. In addition to the discussed optical flow differential techniques, several novel velocimetry approaches based on convolutional neural networks (CNNs) have advantages in efficiency and accuracy [99]. As the CFD discussed in Section 7.2.1 contains the velocity data, it is possible to compare the k^{th} pixel mass flow derived from Eq. (3.21) given by

$$\dot{m}_{i,k} = \rho_{i,k}\bar{u}_k = \frac{M_i}{A}\bar{u}_k \int_0^L \frac{\chi_{\mathrm{CFD}}(s)\,p}{k_B T_{\mathrm{CFD}}(s)}\,ds\,, \tag{7.1}$$

with the ground truth CFD pixel mass flow given by

$$\dot{m}_{i,k,\mathrm{CFD}} = \frac{M_i}{A}\int_0^L \frac{u_{\mathrm{CFD}}(s)\,\chi_{\mathrm{CFD}}(s)\,p}{k_B T_{\mathrm{CFD}}(s)}ds \tag{7.2}$$

where u_{CFD} is the CFD velocity normal to the control surface. Using the column number from the CFD results, one could isolate how the inferred velocity field impacts the mass flow estimates. The effects of the intensity on the velocity estimated can be further investigated. Additionally, the effects of the intensity changes caused by the interference patterns on the interferogram can be investigated using the CFD data.

7.2.3 Nonuniform LOS Profile

The spatial ill-posedness, and the need to parameterize the species volume fraction and temperature along the LOS, is perhaps the leading factor that impairs the accuracy of inferred column densities. In absorption spectroscopy, the distribution along the LOS can be assumed as a uniform profile without significant model errors. However, the results in Chapter 6 showed that the Gaussian approximation can generate an expressive model error for pixels with large column densities. A few studies have successfully inferred the temperature profile along the LOS by solving the Fredholm integral equation of the first kind, but assuming a uniform concentration [49,105,106]. The absorption coefficient of CO_2 varies in a nearly linear way with the volume fraction change, making it impossible to infer the volume fraction profile without additional information.

However, when using the TCMR to generate a LOS profile and assuming linearity around the chosen gas state, it is possible to obtain the Jacobian matrix, Eq. (4.9), of the spectral intensity in relation to a change in the state of the combustion products. The condition number of the Jacobian matrix (actually Cond($\mathbf{J}^T\mathbf{J}$)) may be used to compare the ill-posedness of recovering the temperature at 21 points along the LOS, the same spatial resolution used in Ref. [49], with recovering the combustion state using TCMR for the same conditions. The condition number of the Jacobian of the spectral intensity in the range of 1950 to 2400 cm^{-1} (CO_2, and H_2O absorption bands) to a change in temperature is ~10^{14}, while the additional information introduced through the TCMR reduces it to ~10^{12}. Certainly, the LOS profile inference needs additional information to be reconstructed, and the referred papers used Tikhonov regularization to carry this out.

7.3 Final Remarks

Overall, optical gas imaging shows significant potential to generate independent flare emission measurements without prior knowledge of the flare parameters. The IFTS demonstrated good accuracy using a CFD-based proof-of-concept, and experimental tests on a heated vent. Additionally, in the tests on the lab-scale flares, the IFTS agreed with the CE trend, excluding the measurement contaminated with soot radiative emissions. As a result, the IFTS CE measurements can help to identify the top flare emitters to maximize the effects of mitigation strategies and resources. Although the numerical experiment using the MWIR MS camera showed inferior results than the IFTS, it has a large potential for CE measurements as it is more economically-viable compared to the IFTS. Nevertheless, as no experimental tests were done with the MS camera with the optimal set of filters, the effects of anomalies in the measurement are not accounted to the MS camera. Moreover, the emission from a warm filter MS camera can decrease the SNR, hampering the accuracy of the calibration. In addition, spectroscopy from gas emission proved to be a complex problem as it is very dependent on the gas state distribution along the LOS. Although the average state distribution is close to a Gaussian profile, the non-linearities between fluctuations of radiation intensity and the gas state fluctuations make the instantaneous gas state distribution along the LOS critical. The observed errors in the experimental tests were concentrated on the CO_2 emissions, and the TCMR method added information mainly to combustion products. TCMR has a high potential to improve the experimental results.

References

[1] M.R. Johnson, L.W. Kostiuk, J.L. Spangelo, A Characterization of Solution Gas Flaring in Alberta, J. Air Waste Manage. Assoc. 51 (2001) 1167–1177. https://doi.org/10.1080/10473289.2001.10464348.

[2] C.D. Elvidge, M. Zhizhin, K. Baugh, F.C. Hsu, T. Ghosh, Methods for global survey of natural gas flaring from visible infrared imaging radiometer suite data, Energies. 9 (2016). https://doi.org/10.3390/en9010014.

[3] G. Myhre, D. Shindell, F.-M. Bréon, W. Collins, J. Fuglestvedt, J. Huang, D. Koch, J.-F. Lamarque, D. Lee, B. Mendoza, T. Nakajima, A. Robock, G. Stephens, T. Takemura, H. Zhang, Anthropogenic and Natural Radiative Forcing, Clim. Chang. 2013 Phys. Sci. Basis. Contrib. Work. Gr. I to Fifth Assess. Rep. Intergov. Panel Clim. Chang. (2013) 659–740. https://doi.org/10.1017/ CBO9781107415324.018.

[4] S.O. Giwa, C.N. Nwaokocha, S.I. Kuye, K.O. Adama, Gas flaring attendant impacts of criteria and particulate pollutants: A case of Niger Delta region of Nigeria, J. King Saud Univ. - Eng. Sci. 31 (2019) 209–217. https://doi.org/10.1016/J.JKSUES.2017.04.003.

[5] C.D. Elvidge, M. Zhizhin, F.-C. Hsu, K.E. Baugh, VIIRS Nightfire: Satellite Pyrometry at Night, Remote Sens. 2013, Vol. 5, Pages 4423-4449. 5 (2013) 4423–4449. https://doi.org/10.3390/RS5094423.

[6] Global Gas Flaring Reduction Partnership, Global Gas Flaring Tracker Report, Glob. Gas Flaring Tracker Rep. (2020).

[7] World Bank, Climate Change | Data, World Dev. Indic. World Bank Gr. (2018).

https://data.worldbank.org/topic/climate-change (accessed October 2, 2021).

[8] M. McDaniel, Flare Efficiency Study EPA, (1983).

[9] A. Gvakharia, E.A. Kort, A. Brandt, J. Peischl, T.B. Ryerson, J.P. Schwarz, M.L. Smith, C. Sweeney, Methane, Black Carbon, and Ethane Emissions from Natural Gas Flares in the Bakken Shale, North Dakota, Environ. Sci. Technol. 51 (2017) 5317–5325. https://doi.org/10.1021/ACS.EST.6B05183.

[10] V.M. Torres, S. Herndon, Z. Kodesh, D.T. Allen, Industrial Flare Performance at Low Flow Conditions. 1. Study Overview, Ind. Eng. Chem. Res. 51 (2012) 12559–12568. https://doi.org/10.1021/ie202674t.

[11] K. MacKay, M. Lavoie, E. Bourlon, E. Atherton, E. O'Connell, J. Baillie, C. Fougère, D. Risk, Methane emissions from upstream oil and gas production in Canada are underestimated, Sci. Rep. 11 (2021) 1–8. https://doi.org/10.1038/s41598-021-87610-3.

[12] A. Jernelöv, The threats from oil spills: Now, then, and in the future, Ambio. 39 (2010) 353–366. https://doi.org/10.1007/s13280-010-0085-5.

[13] ECCC, National Inventory Report 1990 –2019 Greenhouse Gas Sources and Sinks in Canada, (2021) 13. https://publications.gc.ca/collections/collection_2021/eccc/En81-4-1-2019-eng.pdf%0Acanada.ca/ghg-inventory.

[14] E.H.T. Doumbia, C. Liousse, S. Keita, L. Granier, C. Granier, C.D. Elvidge, N. Elguindi, K. Law, Flaring emissions in Africa: Distribution, evolution and comparison with current inventories, Atmos. Environ. 199 (2019) 423–434. https://doi.org/10.1016/J.ATMOSENV.2018.11.006.

[15] J. Durango-Cordero, M. Saqalli, R. Parra, A. Elger, Spatial inventory of selected atmospheric emissions from oil industry in Ecuadorian Amazon: Insights from comparisons among satellite and institutional datasets, Saf. Sci. 120 (2019) 107–116. https://doi.org/10.1016/J.SSCI.2019.05.047.

[16] M. Franklin, K. Chau, L.J. Cushing, J.E. Johnston, Characterizing Flaring from Unconventional Oil and Gas Operations in South Texas Using Satellite Observations, Environ. Sci. Technol. 53 (2019) 2220–2228. https://doi.org/10.1021/ACS.EST.8B05355.

[17] M.R. Johnson, R.W. Devillers, K.A. Thomson, Quantitative Field Measurement of Soot Emission from a Large Gas Flare Using Sky-LOSA, Environ. Sci. Technol. 45 (2010) 345–350. https://doi.org/10.1021/ES102230Y.

[18] C.L. Weyant, P.B. Shepson, R. Subramanian, M.O.L. Cambaliza, A. Heimburger, D. McCabe, E. Baum, B.H. Stirm, T.C. Bond, Black Carbon Emissions from Associated Natural Gas Flaring, Environ. Sci. Technol. 50 (2016) 2075–2081. https://doi.org/10.1021/ACS.EST.5B04712.

[19] B.M. Conrad, M.R. Johnson, Field Measurements of Black Carbon Yields from Gas Flaring, Environ. Sci. Technol. 51 (2017) 1893–1900. https://doi.org/10.1021/ACS.EST.6B03690.

[20] S. Faramawy, T. Zaki, A.A.-E. Sakr, Natural gas origin, composition, and processing: A review, J. Nat. Gas Sci. Eng. 34 (2016) 34–54. https://doi.org/10.1016/J.JNGSE.2016.06.030.

[21] M.R. Johnson, A.R. Coderre, Compositions and greenhouse gas emission factors of flared and vented gas in the Western Canadian Sedimentary Basin, J. Air Waste Manag. Assoc. 62 (2012) 992–1002. https://doi.org/10.1080/10962247.2012.676954.

[22] AER (Alberta Energy Regulator), Upstream Petroleum Industry Flaring, Incinerating, and

Venting, Dir. 060. (2016) 99. https://www.aer.ca/documents/directives/Directive060.pdf.

[23] R.B. Miguel, I.M. Machado, F.M. Pereira, P.R. Pagot, F.H.R. França, Application of inverse analysis to correlate the parameters of the weighted-multi-point-source model to compute radiation from flames, Int. J. Heat Mass Transf. 102 (2016) 816–825. https://doi.org/10.1016/J.IJHEATMASSTRANSFER.2016.06.051.

[24] T.A. Brzustowski, Flaring in the energy industry, Prog. Energy Combust. Sci. 2 (1976) 129–141. https://doi.org/10.1016/0360-1285(76)90009-5.

[25] C.D. Elvidge, M.D. Bazilian, M. Zhizhin, T. Ghosh, K. Baugh, F.-C. Hsu, The potential role of natural gas flaring in meeting greenhouse gas mitigation targets, Energy Strateg. Rev. 20 (2018) 156–162. https://doi.org/10.1016/J.ESR.2017.12.012.

[26] D.J. Corbin, Methodology and Experiments to Determine Soot and NOx Yields from a Vertical Lab-Scale Flare Burning Alkane-Mixtures and Ethylene By, 2014.

[27] P. Poudenx, Plume Sampling of a Flare in Crosswind: Structure and Combustion Efficiency, University of Alberta, 2000. https://doi.org/10.1177/001088048102200214.

[28] J.H. Pohl, J. Lee, R. Payne, B.A. Tichenor, Combustion Efficiency of Flares, Combust. Sci. Technol. 50 (1986) 217–231. https://doi.org/10.1080/00102208608923934.

[29] D.J. Corbin, M.R. Johnson, Detailed expressions and methodologies for measuring flare combustion efficiency, species emission rates, and associated uncertainties, Ind. Eng. Chem. Res. 53 (2014) 19359–19369. https://doi.org/10.1021/ie502914k.

[30] K. Müller-Dethlefs, A.F. Schlader, The effect of steam on flame temperature, burning velocity and carbon formation in hydrocarbon flames, Combust. Flame. 27 (1976) 205–215.

https://doi.org/10.1016/0010-2180(76)90023-7.

[31] M.T. Strosher, Characterization of emissions from diffusion flare systems, J. Air Waste Manag. Assoc. 50 (2000) 1723–1733. https://doi.org/10.1080/10473289.2000.10464218.

[32] J.L. Ellzey, J.G. Berbee, Z.F. Tay, D.E. Foster, Total Soot Yield from a Propane Diffusion Flame in Cross-Flow, Combust. Sci. Technol. 71 (1990) 41–52. https://doi.org/10.1080/00102209008951623.

[33] E. Bourguignon, M.R. Johnson, L.W. Kostiuk, The use of a closed-loop wind tunnel for measuring the combustion efficiency of flames in a cross flow, Combust. Flame. 119 (1999) 319–334. https://doi.org/10.1016/S0010-2180(99)00068-1.

[34] M.R. Johnson, L.W. Kostiuk, Efficiencies of low-momentum jet diffusion flames in crosswinds, Combust. Flame. 123 (2000) 189–200. https://doi.org/10.1016/S0010-2180(00)00151-6.

[35] M.R. Johnson, D.J. Wilson, L.W. Kostiuk, A Fuel Stripping Mechanism for Wake-Stabilized Jet Diffusion Flames in Crossflow, Combust. Sci. Technol. 169 (2001) 155–174. https://doi.org/10.1080/00102200108907844.

[36] M. Zamani, E. Abbasi-Atibeh, S. Mobaseri, H. Ahsan, A. Ahsan, J.S. Olfert, L.W. Kostiuk, An experimental study on the carbon conversion efficiency and emission indices of air and steam co-flow diffusion jet flames, Fuel. 287 (2021) 119534. https://doi.org/10.1016/j.fuel.2020.119534.

[37] B. Duck, Reducing emissions in plant flaring operations, 3rd AIChE Reg. Process Technol. Conf. 2011. (2011) 49–72.

[38] D. Castiñeira, T.F. Edgar, CFD for simulation of steam-assisted and air-assisted flare

combustion systems, Energy and Fuels. 20 (2006) 1044–1056. https://doi.org/10.1021/ef050332v.

[39] A. Ahsan, H. Ahsan, J.S. Olfert, L.W. Kostiuk, Quantifying the carbon conversion efficiency and emission indices of a lab-scale natural gas flare with internal coflows of air or steam, Exp. Therm. Fluid Sci. 103 (2019) 133–142. https://doi.org/10.1016/j.expthermflusci.2019.01.013.

[40] V.M. Torres, S. Herndon, D.T. Allen, Industrial flare performance at low flow conditions. 2. Steam- and air-assisted flares, Ind. Eng. Chem. Res. 51 (2012) 12569–12576. https://doi.org/10.1021/ie202675f.

[41] V.M. Torres, TCEQ 2010 Flare Study Final Report Prepared by, Energy. (2011). https://doi.org/August 1, 2011.

[42] J. Wormhoudt, S.C. Herndon, J. Franklin, E.C. Wood, B. Knighton, S. Evans, C. Laush, M. Sloss, R. Spellicy, Comparison of remote sensing and extractive sampling measurements of flare combustion efficiency, Ind. Eng. Chem. Res. 51 (2012) 12621–12629. https://doi.org/10.1021/ie202783m.

[43] M. Gålfalk, G. Olofsson, D. Bastviken, Approaches for hyperspectral remote flux quantification and visualization of GHGs in the environment, Remote Sens. Environ. 191 (2017) 81–94. https://doi.org/10.1016/j.rse.2017.01.012.

[44] J.R. Howell, M.P. Menguc, R. Siegel, Thermal Radiation Heat Transfer, 6th Edition, Taylor & Francis, 2015. https://books.google.ca/books?id=4qYprgEACAAJ.

[45] M. Gharavi, S.G. Buckley, Single diode laser sensor for wide-range H 2O temperature measurements, Appl. Spectrosc. 58 (2004) 468–473.

https://doi.org/10.1366/000370204773580338.

[46] E.E. Whiting, An empirical approximation to the Voigt profile, J. Quant. Spectrosc. Radiat. Transf. 8 (1968) 1379–1384. https://doi.org/10.1016/0022-4073(68)90081-2.

[47] I.E. Gordon, L.S. Rothman, C. Hill, R.V. Kochanov, Y. Tan, P.F. Bernath, M. Birk, V. Boudon, A. Campargue, K.V. Chance, B.J. Drouin, J.-M. Flaud, R.R. Gamache, J.T. Hodges, D. Jacquemart, V.I. Perevalov, A. Perrin, K.P. Shine, M.-A.H. Smith, J. Tennyson, G.C. Toon, H. Tran, V.G. Tyuterev, A. Barbe, A.G. Császár, V.M. Devi, T. Furtenbacher, J.J. Harrison, J.-M. Hartmann, A. Jolly, T.J. Johnson, T. Karman, I. Kleiner, A.A. Kyuberis, J. Loos, O.M. Lyulin, S.T. Massie, S.N. Mikhailenko, N. Moazzen-Ahmadi, H.S.P. Müller, O.V. Naumenko, A.V. Nikitin, O.L. Polyansky, M. Rey, M. Rotger, S.W. Sharpe, K. Sung, E. Starikova, S.A. Tashkun, J. Vander Auwera, G. Wagner, J. Wilzewski, P. Wcisło, S. Yu, E.J. Zak, The HITRAN2016 molecular spectroscopic database, J. Quant. Spectrosc. Radiat. Transf. 203 (2017) 3–69. https://doi.org/10.1016/J.JQSRT.2017.06.038.

[48] J. Taine, A. Soufiani, Gas IR Radiative Properties : From Spectroscopic Data to Approximate Models, 1999.

[49] T. Ren, M.F. Modest, Temperature Profile Inversion from Carbon-Dioxide Spectral Intensities Through Tikhonov Regularization, J. Thermophys. Heat Transf. 30 (2016) 211–218. https://doi.org/10.2514/1.T4561.

[50] I.E. Gordon, L.S. Rothman, R.J. Hargreaves, R. Hashemi, E. V. Karlovets, F.M. Skinner, E.K. Conway, C. Hill, R. V. Kochanov, Y. Tan, P. Wcisło, A.A. Finenko, K. Nelson, P.F. Bernath, M. Birk, V. Boudon, A. Campargue, K. V. Chance, A. Coustenis, B.J. Drouin, J.M. Flaud, R.R. Gamache, J.T. Hodges, D. Jacquemart, E.J. Mlawer, A. V. Nikitin, V.I. Perevalov, M. Rotger,

J. Tennyson, G.C. Toon, H. Tran, V.G. Tyuterev, E.M. Adkins, A. Baker, A. Barbe, E. Canè, A.G. Császár, A. Dudaryonok, O. Egorov, A.J. Fleisher, H. Fleurbaey, A. Foltynowicz, T. Furtenbacher, J.J. Harrison, J.M. Hartmann, V.M. Horneman, X. Huang, T. Karman, J. Karns, S. Kassi, I. Kleiner, V. Kofman, F. Kwabia-Tchana, N.N. Lavrentieva, T.J. Lee, D.A. Long, A.A. Lukashevskaya, O.M. Lyulin, V.Y. Makhnev, W. Matt, S.T. Massie, M. Melosso, S.N. Mikhailenko, D. Mondelain, H.S.P. Müller, O. V. Naumenko, A. Perrin, O.L. Polyansky, E. Raddaoui, P.L. Raston, Z.D. Reed, M. Rey, C. Richard, R. Tóbiás, I. Sadiek, D.W. Schwenke, E. Starikova, K. Sung, F. Tamassia, S.A. Tashkun, J. Vander Auwera, I.A. Vasilenko, A.A. Vigasin, G.L. Villanueva, B. Vispoel, G. Wagner, A. Yachmenev, S.N. Yurchenko, The HITRAN2020 molecular spectroscopic database, J. Quant. Spectrosc. Radiat. Transf. 277 (2022) 107949. https://doi.org/10.1016/j.jqsrt.2021.107949.

[51] N. Kasai, C. Tsuchiya, T. Fukuda, K. Sekine, T. Sano, T. Takehana, Propane gas leak detection by infrared absorption using carbon infrared emitter and infrared camera, NDT E Int. 44 (2011) 57–60. https://doi.org/10.1016/J.NDTEINT.2010.09.006.

[52] R. Nelson, Optical gas imaging: From qualitative to quantitative, CONCAWE Rev. 25 (2016) 18–19.

[53] H. Abdel-Moati, J. Morris, Y. Zeng, P. Kangas, D. McGregor, New Optical Gas Imaging Technology for Quantifying Fugitive Emission Rates, in: Int. Pet. Technol. Conf., Qatar, 2015.

[54] G. Druart, P.-Y. Foucher, S. Doz, X. Watremez, S. Jourdan, E. Vanneau, H. Pinot, Test of SIMAGAZ: a LWIR cryogenic multispectral infrared camera for methane gas leak detection and quantification, (2021) 9. https://doi.org/10.1117/12.2586933.

[55] R. Milner, FLIR, personal communication, (2017).

[56] M.-A.A. Gagnon, K.-A.A. Jahjah, F. Marcotte, P. Tremblay, V. Farley, M. Chamberland, É. Guyot, M. Chamberland, Time-resolved thermal infrared multispectral imaging of gases and minerals, Electro-Optical Infrared Syst. Technol. Appl. XI. 9249 (2014) 92490U. https://doi.org/10.1117/12.2064611.

[57] M. Vollmer, K.-P. Möllmann, Infrared Thermal Imaging, Wiley-VCH Verlag GmbH & Co. KGaA, Weinheim, Germany, 2010. https://doi.org/10.1002/9783527630868.

[58] E.A. Moore, K.C. Gross, S.J. Bowen, G.P. Perram, M. Chamberland, V. Farley, J.-P. Gagnon, P. Lagueux, A. Villemaire, Characterizing and overcoming spectral artifacts in imaging Fourier-transform spectroscopy of turbulent exhaust plumes, in: A.W. Fountain III, P.J. Gardner (Eds.), International Society for Optics and Photonics, 2009: p. 730416. https://doi.org/10.1117/12.818710.

[59] K.C. Gross, P. Tremblay, K.C. Bradley, M. Chamberland, V. Farley, G.P. Perram, Instrument calibration and lineshape modeling for ultraspectral imagery measurements of industrial smokestack emissions, in: S.S. Shen, P.E. Lewis (Eds.), Proc. SPIE, International Society for Optics and Photonics, 2010: p. 769516. https://doi.org/10.1117/12.850142.

[60] J.L. Massman, K.C. Gross, Understanding the influence of turbulence in imaging Fourier transform spectroscopy of smokestack plumes, Algorithms Technol. Multispectral, Hyperspectral, Ultraspectral Imag. XVII. 8048 (2011) 80480A. https://doi.org/10.1117/12.883197.

[61] A.M. Young, Scene Change Artifacts in Fourier Transform Spectroscopy of Temporally Changing Sources, (2010).

[62] P. Tremblay, K.C. Gross, V. Farley, M. Chamberland, A. Villemaire, G.P. Perram,

Understanding and overcoming scene-change artifacts in imaging Fourier-transform spectroscopy of turbulent jet engine exhaust, Imaging Spectrom. XIV. 7457 (2009) 74570F. https://doi.org/10.1117/12.828001.

[63] M.A. Rodríguez-Conejo, J. Meléndez, Hyperspectral quantitative imaging of gas sources in the mid-infrared, Appl. Opt. 54 (2015) 141. https://doi.org/10.1364/AO.54.000141.

[64] K.C. Gross, K.C. Bradley, G.P. Perram, Remote identification and quantification of industrial smokestack effluents via imaging fourier-transform spectroscopy, Environ. Sci. Technol. 44 (2010) 9390–9397. https://doi.org/10.1021/es101823z.

[65] A. Soufiani, J.P. Martin, J.C. Rolon, L. Brenez, Sensitivity of temperature and concentration measurements in hot gases from FTIR emission spectroscopy, J. Quant. Spectrosc. Radiat. Transf. 73 (2002) 317–327. https://doi.org/10.1016/S0022-4073(01)00209-6.

[66] S.J. Grauer, B.M. Conrad, R.B. Miguel, K.J. Daun, Gaussian model for emission rate measurement of heated plumes using hyperspectral data, J. Quant. Spectrosc. Radiat. Transf. 206 (2018) 125–134. https://doi.org/10.1016/j.jqsrt.2017.11.005.

[67] M.R. Johnson, R.W. Devillers, K.A. Thomson, A Generalized Sky-LOSA Method to Quantify Soot/Black Carbon Emission Rates in Atmospheric Plumes of Gas Flares, Aerosol Sci. Technol. 47 (2013) 1017–1029. https://doi.org/10.1080/02786826.2013.809401.

[68] B.K.P. Horn, B.G. Schunck, Determining optical flow., Comput. Vis. 17 (1981) 185–203. https://doi.org/10.7551/mitpress/1413.003.0014.

[69] Y. Zeng, J. Morris, M. Dombrowski, Validation of a new method for measuring and continuously monitoring the efficiency of industrial flares, J. Air Waste Manag. Assoc. 66

(2016) 76–86. https://doi.org/10.1080/10962247.2015.1114045.

[70] Y. Zeng, J. Morris, M. Dombrowski, Multi-Spectral Infrared Imaging System for Flare Combustion Efficiency Monitoring, 2016. https://patents.google.com/patent/US9258495B2/en (accessed June 25, 2018).

[71] J. Sandsten, P. Weibring, H. Edner, S. Svanberg, Real-time gas-correlation imaging employing thermal background radiation, Opt. Express. 6 (2000) 92–103. https://doi.org/10.1364/OE.6.000092.

[72] J. Sandsten, H. Edner, S. Svanberg, Gas visualization of industrial hydrocarbon emissions., Opt. Express. 12 (2004) 1443–1451. https://doi.org/10.1364/OPEX.12.001443.

[73] J. Sandsten, M. Andersson, Volume flow calculations on gas leaks imaged with infrared gas-correlation, Opt. Express. 20 (2012) 20318–20329. https://doi.org/10.1364/OE.20.020318.

[74] J.P. Dakin, H.O. Edwards, Progress in fiber-remoted gas correlation spectrometry, Opt. Eng. 31 (1992) 1616. https://doi.org/10.1117/12.58704.

[75] P. Chambers, E.A.D. Austin, J.P. Dakin, Theoretical analysis of a methane gas detection system, using the complementary source modulation method of correlation spectroscopy, Meas. Sci. Technol. 15 (2004) 1629–1636. https://doi.org/10.1088/0957-0233/15/8/034.

[76] A. Cheung, W. Johnstone, D. Moodie, Gas detection based on optical correlation spectroscopy using a single light source, Meas. Sci. Technol. 17 (2006) 1107–1112. https://doi.org/10.1088/0957-0233/17/5/S28.

[77] J.L. Harley, K.C. Gross, Remote quantification of smokestack effluent mass flow rates using imaging Fourier transform spectrometry, Chem. Biol. Radiol. Nucl. Explos. Sens. XII. 8018

(2011) 801813. https://doi.org/10.1117/12.883193.

[78] J.L. Harley, B.A. Rankin, D.L. Blunck, J.P. Gore, K.C. Gross, Imaging Fourier-transform spectrometer measurements of a turbulent nonpremixed jet flame, Opt Lett. 39 (2014) 2350–2353. https://doi.org/10.1364/OL.39.002350.

[79] X. Watremez, N. Labat, G. Audouin, B. Lejay, X. Marcarian, D. Dubucq, A. Marblé, P.-Y. Foucher, L. Poutier, R. Danno, D. Elie, M. Chamberland, Remote Detection and Flow rates Quantification of Methane Releases Using Infrared Camera Technology and 3D Reconstruction Algorithm, SPE Annu. Tech. Conf. Exhib. (2016) 1–17. https://doi.org/10.2118/181501-MS.

[80] R.B. Miguel, J. Emmert, S.J. Grauer, J.N. Thornock, K.J. Daun, Optimal filter selection for quantitative gas mixture imaging, J. Quant. Spectrosc. Radiat. Transf. 254 (2020) 107208. https://doi.org/10.1016/j.jqsrt.2020.107208.

[81] S. (Department of E.E.U. Boyd, L. (Electrical E.D. of C. Vandenberghe, Convex Optimization, Cambridger University Press, 2004. https://doi.org/10.1002/9781119295952.app1.

[82] M.A. Delichatsios, Transition from momentum to buoyancy-controlled turbulent jet diffusion flames and flame height relationships, Combust. Flame. 92 (1993) 349–364. https://doi.org/10.1016/0010-2180(93)90148-V.

[83] S.G. Parker, A component-based architecture for parallel multi-physics PDE simulation, Futur. Gener. Comput. Syst. 22 (2006) 204–216. https://doi.org/10.1016/j.future.2005.04.001.

[84] S.G. Parker, J. Guilkey, T. Harman, A component-based parallel infrastructure for the simulation of fluid–structure interaction, Eng. with Comput. 2006 223. 22 (2006) 277–292. https://doi.org/10.1007/S00366-006-0047-5.

[85] J. Davison De, J. McCorquodale, S.G. Parker, C.R. Johnson, Uintah: A massively parallel problem solving environment, Proc. IEEE Int. Symp. High Perform. Distrib. Comput. 2000-Janua (2000) 33–41. https://doi.org/10.1109/HPDC.2000.868632.

[86] A.F. Sarofim, H.C. Hottel, Radiative Transfer in Combustion Chambers: Influence of Alternative Fuels, Heat Transf. 6 (1978) 199–217.

[87] C.K. Westbrook, F.L. DRYER, C.K. Westbrook, Simplified Reaction Mechanisms for the Oxidation of Hydrocarbon Fuels in Flames, Combust. Sci. Technol. 27 (1981) 31–43. https://doi.org/10.1080/00102208108946970.

[88] B.M. Conrad, J.N. Thornock, M.R. Johnson, Beam steering effects on remote optical measurements of pollutant emissions in heated plumes and flares, J. Quant. Spectrosc. Radiat. Transf. 254 (2020) 107191. https://doi.org/10.1016/j.jqsrt.2020.107191.

[89] Spectrogon US Inc., Spectrogon Optical Interference Filters Catalog, (n.d.). https://www.spectrogon.com/product-services/optical-filters/spectrogon-us/ (accessed October 25, 2019).

[90] R.B. Miguel, S. Talebi-Moghaddam, M. Zamani, C. Turcotte, K.J. Daun, Assessing Flare Combustion Efficiency using Imaging Fourier Transform Spectroscopy, J. Quant. Spectrosc. Radiat. Transf. 273 (2021) 107835. https://doi.org/10.1016/j.jqsrt.2021.107835.

[91] P. Biévre, M. Gallet, N.E. Holden, I.L. Barnes, Isotopic Abundances and Atomic Weights of the Elements, J. Phys. Chem. Ref. Data. 13 (1984) 809–891. https://doi.org/10.1063/1.555720.

[92] C.M. Stevens, A. Engelkemeir, Stable carbon isotopic composition of methane from some natural and anthropogenic sources, J. Geophys. Res. 93 (1988) 725.

https://doi.org/10.1029/jd093id01p00725.

[93] D. Widory, Combustibles, fuels and their combustion products: A view through carbon isotopes, Combust. Theory Model. 10 (2006) 831–841. https://doi.org/10.1080/13647830600720264.

[94] R.B. Miguel, J. Emmert, K.J. Daun, Enhancing optical quantification of combustion products using thermochemical manifold reduction, J. Quant. Spectrosc. Radiat. Transf. 289 (2022) 108293. https://doi.org/10.1016/j.jqsrt.2022.108293.

[95] G. Sorrentino, G. Ceriello, A. Cavaliere, M. de Joannon, R. Ragucci, Thermo-chemical manifold reduction for tabulated chemistry modeling. Temperature and dilution constraints for smooth combustion reactors, Proc. Combust. Inst. 38 (2021) 5393–5402. https://doi.org/10.1016/J.PROCI.2020.06.144.

[96] G. Hankinson, B.J. Lowesmith, A consideration of methods of determining the radiative characteristics of jet fires, Combust. Flame. 159 (2012) 1165–1177. https://doi.org/10.1016/J.COMBUSTFLAME.2011.09.004.

[97] J.L. Barron, D.J. Fleet, S.S. Beauchemin, Performance of optical flow techniques, Int. J. Comput. Vis. 12 (1994) 43–77. https://doi.org/10.1007/BF01420984.

[98] S. Baker, D. Scharstein, J.P. Lewis, S. Roth, M.J. Black, R. Szeliski, A database and evaluation methodology for optical flow, Int. J. Comput. Vis. 92 (2011) 1–31. https://doi.org/10.1007/s11263-010-0390-2.

[99] Z. Tu, W. Xie, D. Zhang, R. Poppe, R.C. Veltkamp, B. Li, J. Yuan, A survey of variational and CNN-based optical flow techniques, Signal Process. Image Commun. 72 (2019) 9–24. https://doi.org/10.1016/j.image.2018.12.002.

[100] T. Corpetti, D. Heitz, G. Arroyo, E. Mémin, A. Santa-Cruz, Fluid experimental flow estimation based on an optical-flow scheme, Exp. Fluids. 40 (2006) 80–97. https://doi.org/10.1007/s00348-005-0048-y.

[101] L.P.N. Mendes, A.M.C. Ricardo, A.J.M. Bernardino, R.M.L. Ferreira, A comparative study of optical flow methods for fluid mechanics, Exp. Fluids. 63 (2022) 1–26. https://doi.org/10.1007/s00348-021-03357-7.

[102] B.D. Lucas, T. Kanade, An iterative image registration technique with an application to stereo vision, (1981) 674–679.

[103] G. Farnebäck, Two-Frame Motion Estimation Based on Polynomial Expansion, in: J. Bigun, T. Gustavsson (Eds.), Image Anal., Springer Berlin Heidelberg, Berlin, Heidelberg, 2003: pp. 363–370.

[104] T. Liu, L. Shen, Fluid flow and optical flow, J. Fluid Mech. 614 (2008) 253–291. https://doi.org/10.1017/S0022112008003273.

[105] N.A. Malarich, G.B. Rieker, Resolving nonuniform temperature distributions with single-beam absorption spectroscopy. Part I: Theoretical capabilities and limitations, J. Quant. Spectrosc. Radiat. Transf. 260 (2021) 107455. https://doi.org/10.1016/j.jqsrt.2020.107455.

[106] N.A. Malarich, G.B. Rieker, Resolving nonuniform temperature distributions with single-beam absorption spectroscopy. Part II: Implementation from broadband spectra, n.d.

Appendix

Analysis of the Commercially-Available Equipment for Flare Combustion Efficiency Quantification

To the best of the author's knowledge, the only commercially-available technique for measuring flare CE using optical devices is the multi-spectral infrared imaging system for flare CE monitoring from Providence Photonics, which is described in Refs. [69,70]. According to the patent [70], the equipment uses broadband signals to estimate the flame product concentrations. As described in Section 3.1.3, broadband imagers are faster and less expensive than IFTSs. The Patent describes the method using four broadband channels to estimate the concentration of different combustion products, as shown in Figure 52. The first channel, from 2940 to 3030 cm^{-1} (3.3-3.4 μm,) is used to estimate the concentration of unburned fuel. The second and third channels, 2325 to 2380 cm^{-1} (4.2-4.3 μm) and 2080 to 2130 cm^{-1} (4.7-4.8 μm), infer the concentration of CO_2 and CO respectively. The fourth channel corresponds to the reference, 2780 to 2860 cm^{-1} (3.5-3.6 μm), over which the species-of-interest are transparent, but emissions from soot present in the flame are approximately the same as other bands.

However, to infer combustion product concentrations and the temperature, at least one broadband signal is needed for each species, with an additional channel to infer temperature. Assuming the possibility that in some pixels will contain only one species-of-interest at a time, the concentration and temperature will need to be inferred simultaneously for each species-of-interest. Therefore, at least two independent broadband signals are needed for each species of interest when expected one species at a time, i.e. measurement of unburned fuel without CO_2 and combustion products in other pixels without unburned fuel.

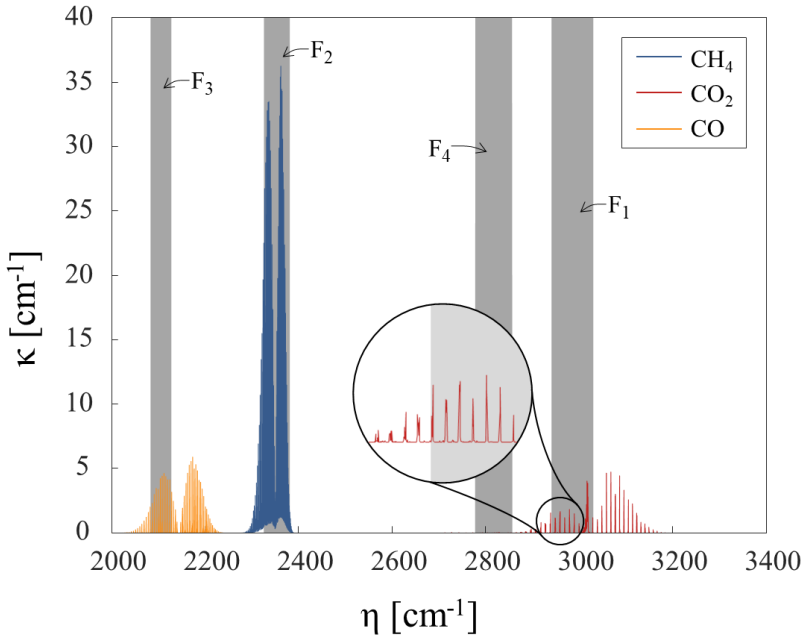

Figure 52 Spectral bands selected to represent each species adapted from [70].

In the method described in [ref], the radiative emission from the flame combustion products is approximated by

$$I_{L\eta} = \kappa_\eta I_{b\eta}(T_g)L = \alpha_{\eta,i}\chi_i I_{b\eta}(T_g)L, \tag{A.1}$$

the effect of collision broadening is considered constant in the function of gas concentrations, and concentration is detached from the absorption coefficient $\alpha_{\eta,i}$. Concentration and temperature are modelled as uniform along the LOS. For the broadband channels, the absorption coefficient is considered spectrally uniform ("grey") over the whole band, and the observed emission from the jth channel is considered as

$$S_j = \overline{\alpha_{\eta,i}}\chi_i L\overline{I_{b\eta,j}}, \tag{A.2}$$

where $\overline{I_{b\eta,j}}$ is the spectrally averaged blackbody radiation for this band. The concentration of species *i* can then be obtained by reorganizing Eq. (A.2) in the form

$$\chi_i = \frac{S_j}{\overline{\overline{\alpha_{\eta,i}} L \overline{I_{b\eta,j}}}}. \tag{A.3}$$

The local CE of the flare is found by substituting the concentration of Eq. (A.3) into Eq. (2.9), and, as the LOS length is the same for all bands,

$$\eta_{\text{comb}} = \frac{\dfrac{S_2}{B_2(T_g)\overline{\alpha}_{\eta,CO2}}}{\dfrac{S_1}{B_1(T_g)\overline{\alpha}_{\eta,HC}} + \dfrac{S_2}{B_2(T_g)\overline{\alpha}_{\eta,CO2}} + \dfrac{S_3}{B_3(T_g)\overline{\alpha}_{\eta,CO}}}. \tag{A.4}$$

From this point, the authors propose three approximations to simplify Eq. (A.4). In the first approach, the variation of blackbody emission with respect to wavelength over the entire measurement spectrum is neglected. With this consideration, Eq. (A.4) can be rewritten as

$$\eta_{\text{comb,M1}} = \frac{\dfrac{S_2}{\overline{\alpha}_{\eta,CO2}}}{\dfrac{S_1}{\overline{\alpha}_{\eta,HC}} + \dfrac{S_2}{\overline{\alpha}_{\eta,CO2}} + \dfrac{S_3}{\overline{\alpha}_{\eta,CO}}}. \tag{A.5}$$

In the second method, the fourth band is used to find the gas temperature through Planck's law and then use the gas temperature to calculate the blackbody emission in each band of Eq. (A.4). As the fourth band is transparent to combustion gases, the authors are planning to use calibration or additional bands to infer the gas temperature. The third method proposed is to pre-compute the ratio between blackbody contribution of each band to the fourth band for temperatures between 700 K and 920 K. In this method, instead of considering all blackbody contributions as equal, the values of Eq. (A.4) are weighted by the ratios of the band blackbody emission to the reference band blackbody emission.

The simplifications involved in deriving Eq. (A.4) or (A.5) introduce model errors in the inferred combustion efficiency. The concentration distribution along each LOS is considered uniform and can generate significant errors in emission spectroscopy. The authors also neglect the reabsorption of the radiation emitted by the plume along each LOS, i.e. the optically-thin approximation; this effect may be significant considering that the signal captured by the camera is from the gas radiative emission, not background radiation absorption by the gas. Another possible source of error comes from estimating the overall CE as the average of the local CE over the visible flame envelope as in ref [70]. The average approximation does not account for the species' mass flows. Consequently, unburned products with the same concentration but with a lower velocity and therefore a lower mass flow will have the same influence as a gas stream with a higher velocity, thereby underpredicting the CE. Additionally, the method does not account for the unburned fuel that leaves the flame by the stripping mechanism, over predicting the overall CE.

The methods proposed in reference [70] were used to obtain the combustion efficiency from the flare LES simulation as described in Section 4.4.1. The pixels' location was the same tested in Section 5.1 and is shown in Figure 28. The signal corresponding to each sampled pixel was synthetically generated using the temperature and gas concentrations from the flare LES using the non-optically thin RTE, Eq (3.11), and the broadband signal for each band by Eq (3.14) considering ideal cold filters. The CE of each pixel was then approximated using methods 1 (M1) and 2 and 3 (M2) using the temperature from the LES. Although it is impossible to obtain the gas temperature using the proposed method, it gives some advantage to M1, and method 2 and 3 becomes equivalent. The results are shown in Figure 53.

The graphics showed that M1 overpredicts the CE while M2 underpredicts the pixels' CE. As proposed in the document, the global CE should be calculated by the average of the pixels CE on the

flame envelope (not considering the mass flow of each gas). The procedure was repeated to the pixels on the flame envelope, generating the same results.

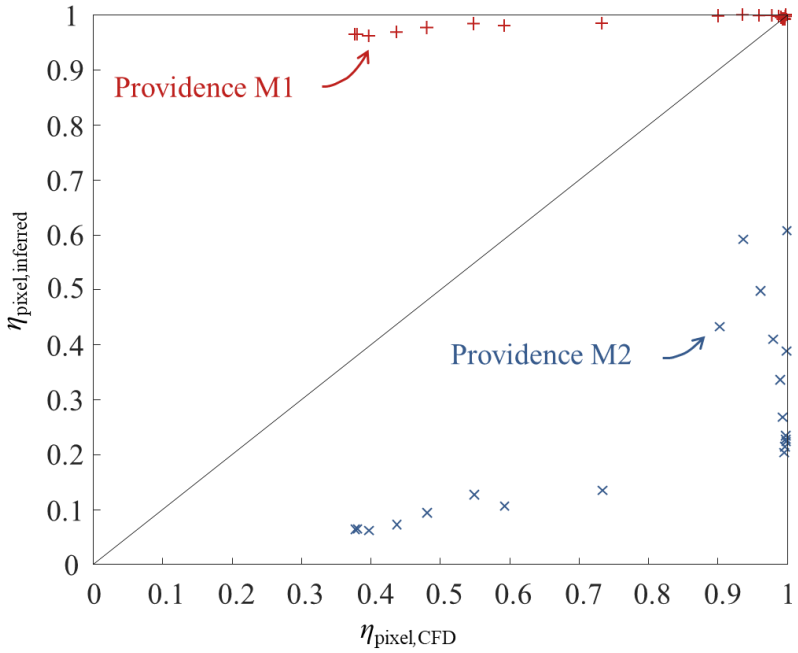

Figure 53 Comparison between pixels' CE obtained using the described methods and the CFD pixels' CE.

On the other hand, the authors specified an IFTS as the used apparatus in the peer-reviewed publication [69]. The equipment uses a SOC750 MWIR hyperspectral imager from Surface Optics Corporation with a spatial resolution of 256×240 pixels and a spectral discretization of 42 bands. According to the authors, the spectral data is downsampled to four (undefined) broadband channels selected to estimate the concentration of each product of combustion containing carbon. The spectral resolution from an IFTS should facilitate the simultaneous inference of gas concentration and temperature of each species of interest. However, the paper reference the patent as the method utilized

and does not describe the method using the IFTS. In addition, the data collected by the IFTS is not published, and it is not possible to replicate the results.

All flares with low CE tested in the paper are from steam-assisted flares. As water has spectral lines in the same band as described in the method to measure unburned fuel. In the case of model fitting using the collected data, it can correlate steam radiative emission with CE. The water absorption coefficient is weaker than the fuel absorption coefficient in this spectral region. However, water can be found in higher concentrations and temperatures.

The method to measure CE using broadband bands described in the patent has several flaws. First, the method uses the optically-thin model that potentially over-predicts each species' amount on each pixel. This error is a function of the gas temperature and concentration distribution along the LOS. As the combustion products and unburned fuel – the leading cause of inefficiencies in flares – have different temperatures, this error can cause errors in the CE estimation. Second, the gas concentration and temperature are considered uniform along the LOS. The Gaussian distribution along the LOS generates more precise species flow quantification in emission spectroscopy. Third, the method does not infer the gas temperature or assumes that the unburned fuel has the same temperature as the combustion products. As the problem is ill-posed when broadband signals are used, a low concentration gas with high temperature can generate the same broadband signal as a high concentration gas with low temperature; to infer temperature and concentration simultaneously is needed at least two broadband signals per species of interest. Last, the method computes the global CE as the average of all pixels in the flame envelope. This procedure does compute the mass flow of each species, i.e. pixels with the same concentrations with different gas velocities will have the same weights at the global CE calculation, despite the species mass flow difference.

The peer-reviewed paper shows promising results but does not describe the scientific method utilized, and it is not possible to be replicated considering the presented data. The low CE studied flares are all from steam-assisted flares; if a model fitting is used, the results obtained can be generated by steam radiative emission instead of unburned fuel. It is needed tests with a broader range of CE using other methods of flare assistance to isolate water radiative emission effects from the results. Furthermore, the water concentration and temperature can be estimated using other spectral bands, and the radiative effect can be accounted for in the model.